Theoretical Study on Vortex States in Unconventional Superconductors

Yuki TAKAHASHI

February 2014

Theoretical Study on Vortex States in Unconventional Superconductors

Yuki TAKAHASHI
Doctoral Program in Materials Science and Engineering

Submitted to the Graduate School of
Pure and Applied Sciences
in Partial Fulfillment of the Requirements
for the Degree of Doctor of Philosophy in
Engineering

at the
University of Tsukuba

Abstract

The *vortex*, a quantized magnetic flux surrounded by local supercurrents, plays an important role in the magnetic properties of type-II superconductors. While vortices are understood to behave as line-like objects within a mean-field theory, this simple notion may not be appropriate in unconventional superconductors like copper-oxide (cuprate) or iron-based superconductors because of the nature of their intrinsic superconducting mechanism or their crystalline structures. Motivated by such critical characteristics for vortex states, namely "multibandness" and "dimensionality", I explore in numerical simulations theoretic aspects of novel vortex states in unconventional superconductors.

In Chapter 1, I shall first review the fundamental magnetic properties in conventional superconductors within the framework of the Ginzburg-Landau (GL) theory, and thereby introduce the vortex as the principal player in type-II superconductors. The microscopic theory known as the Bardeen-Cooper-Schrieffer (BCS) theory is also reviewed to connect with phenomenological parameters that appear in the GL theory. I then provide an overview of the latest timeline of discoveries in the field of superconductivity, and illuminate two characteristics, multibandness and dimensionality, which have an inevitable impact on vortex states. For multibandness, I review the latest theoretical studies that simply extending conventional multiband theory ($N = 2$: N for the number of superconductivity condensation) in a straightforward manner is not sufficient for more general cases ($N \geq 3$), and that essentially novel superconductivity appears spontaneously, i.e. time-reversal symmetry breaking (TRSB). A multicomponent GL theory is introduced that extends the conventional GL theory to describe multiband superconductivity and used to discuss the stability condition of the TRSB state.

In Chapter 2, I focus attention on the temperature dependence of the stability condition for the TRSB state based on the BCS theory. Additionally, for the following discussion of vortex states in multicomponent TRSB superconductors, I explain the principal parameterization used in numerical calculation based on the time-dependent Ginzburg-Landau (TDGL) method.

In Chapter 3, I begin discussing vortex structures in multicomponent TRSB superconductors simulated using a TDGL method near the critical temperature $T_{\rm c}$ where the GL theory is valid. Single-vortex solutions reveal qualitatively anomalous vortex structures associated with multiple divergent coherence lengths.

In Chapter 4, I employ the TDGL method to investigate interactions between vortices in the multicomponent TRSB superconductor. A novel intermediate state is found that is characterized by vortex clustering when the material parameters satisfy a certain condition wherein the nucleation field is slightly larger than the thermodynamic field ($H_{\rm n} \gtrsim H_{\rm tc}$). A calculation of the interface energy reveals that the vortex cluster is associated with positive interface energy. I thereby compose novel H-T phase diagrams where the multicomponent TRSB superconductor cannot be classified as simply type-I or type-II as in conventional single-component superconductors.

In Chapter 5, I investigate further details of the H-T phase diagrams, focusing in particular on the lower critical field ($H_{\rm c1}$) accompanying with the novel vortex state. Using the TDGL method, I demonstrate typical magnetization curves (M-H) and highlight vortex penetration at $H_{\rm c1}$. Remarkable dynamics are found to occur during vortex penetration that suggest an experimental method to probe the TRSB state in multicomponent superconductivity.

In Chapter 6, I turn to the study of vortex states affected by the dimensionality. A typical system of interest is the cuprate superconductors which have been well established as having two-dimensional superconductivity originating within CuO_2 layers. As characterized by the anisotropy parameter $\gamma \equiv \xi_{ab}/\xi_c$ with ξ_c (ξ_{ab}) denoting the coherence lengths perpendicular (parallel) to the CuO_2 layers, the vortex states in layered superconductors with large γ vary considerably depending on the direction of the applied magnetic fields. Although the vortex states in perpendicular fields ($H \perp ab$) are nowadays well elucidated, those in parallel fields ($H \parallel ab$) where vortices are confined between the CuO_2 layers, namely *Josephson vortex* (JV) states, have not been equally investigated. Because of the commensurability condition between the JV lattice constant determined by the external magnetic fields and periodicity of the layered structure, interlayer JVs can take various configurations.

Using the Langevin simulation for the in-plane JV flow dynamics subject to point-like pinning centers, I analyze the experimental results on the resistivity using a single crystal of underdoped $YBa_2Cu_3O_y$ with anisotropy parameter $\gamma \sim 50$. I thereby identify a unique JV lattice state not seen previously.

Chapter 7 provides a summary of general conclusions and an outlook for the new developments described above.

Acknowledgements

I have completed my PhD work supported by uncountable support, excellent tuition, and encouragement. I would like to impress my acknowledgement on this occasion.

First and foremost, I would like to express my gratitude to my supervisor Professor Xiao Hu, who enrolled me in the PhD program at University of Tsukuba, for his always constructive discussions and supervising general attitudes toward scientific works. His noble character can be seen not only in research scenes but also in daily lab-life, that he takes warm care of working motivation of all group members with casual activities outside of the lab. I therefore could have spent fruitful three years.

I am fortunate having been surrounded by competent group members. For Professor Meng-Bo Luo, who supported me with his excellent Langevin-dynamics simulation studying the Josephson vortex states discussed in this thesis, I owe him a debt of gratitude to successive collaboration with my experimental result. For Dr. Shi-Zeng Lin, I acknowledge his support with TDGL coding used in my work, as well as his progressive and inspiring works about multiband superconductivity. For Dr. Zhao Huang, I specially thank him for vital contribution to our scientific papers and for a lot of discussions. I would like to thank all the members, Dr. Masanori Kohno, Prof. Zhi Wang, Prof. Qi-Feng Liang, Dr. Sasmita Mohakud, Dr. Munehisa Matsumoto, Dr. Madhav Prasad Ghimire, Dr. Bin Xi, Dr. Xue-Yuan Hu, Dr. Takuto Kawakami, Dr. Rui Yu, Dr. Feng Liu, and Dr. Long-Hua Wu, for their insightful comments on my work.

I am distinctively grateful to my supervisors for my MSc work, Prof. Norio Kobayashi and Prof. Terukazu Nishizaki, for their warm understandings to resume my academic career, and for the first invitation to research on the vortex matter in superconductivity. The experimental results analyzed in this thesis are extracted from my MSc thesis, and the measurements were performed at the Institute for Materials Research, Tohoku University (Sendai, Japan).

Lastly, I sincerely thank to my family, mom Misuzu, Yuiko, and Koh for their heartfelt support in accomplishing the PhD work. I dedicate this thesis to my father in memory, Tetsuro Takahashi, who gently encouraged me always from far.

Definitions

Definitions of acronyms

AFM	Antiferromagnetic
BCS	Bardeen Cooper Schrieffer
FM	Ferromagnetic
GL	Ginzburg-Landau
HTSC	High-temperature superconductor
JV	Josephson vortex
MCGL	Multi-Component Ginzburg-Landau
SC	Superconductor
SDW	Spin density wave
TDGL	Time-dependent Ginzburg-Landau
TRSB	Time-reversal symmetry breaking
TRSR	Time-reversal symmetry reserved

Definitions of notation

$\mathbf{A}$	Vector potential
$\mathbf{B}$	Magnetic flux density
Δ	Superconductivity gap
e	Charge on an electron, $e = 1.602 \times 10^{-19}$C
F	Helmholtz free energy
G	Gibbs free energy
h	Planck constant, $h = 6.626 \times 10^{-34}$Js
$\hbar$	Reduced Planck constant, $\hbar = h/(2\pi) = 1.055 \times 10^{-34}$Js
H	Applied magnetic field
H_{c1}	Lower critical field
H_{c2}	Upper critical field
H_{n}	Nucleation field
H_{tc}	Thermodynamic field
J_{s}	Superconductivity current (Supercurrent)
$\mathbf{k}$	Wave number
k_{B}	Boltzmann constant, $k_{\mathrm{B}} = 1.381 \times 10^{-23}\mathrm{JK}^{-1}$
κ	GL parameter $\kappa \equiv \lambda/\xi$
λ	Magnetic-field penetration depth
m	Electron mass, $m = 9.109 \times 10^{31}$kg
m^*	Effective mass of a Cooper pair, $m^* \approx 2m$
M	Magnetization
μ_0	Vacuum permeability
ω_{D}	Debye frequency
Φ_0	Magnetic flux quantum, $\Phi_0 = hc/2e = 2.068 \times 10^{-15}$Wb
ψ	Order parameter
T	Temperature
T_{c}	Critical temperature
ξ	Superconductivity coherence length
x, y, z	Coordinates of real space

Contents

Chapter 1

Introduction

Superconductivity, which was discovered in 1911 by H. Kamerlingh Onnes [1] in his intensive development of the experimental environment at low-temperature, represents one of the vast historical stages in modern physics. The characteristics of *zero resistivity* is interesting in view of not only fundamental physics but also applications. As Onnes proposed in his speech for the Nobel prize win, superconductivity was readily expected to yield successes in applications such as high-field magnets by taking advantage of its dissipationless conductivity. Another hallmark, *perfect diamagnetism*, was discovered in 1933 by W. Meissner and R. Ochsenfeld [2]. They found that magnetic fields are excluded from the interior of superconductors, a phenomenon that cannot be explained by perfect conductivity. However, it was soon realized that the critical field at which the superconductivity is broken by magnetic fields are typically low, at most 1 kOe in the known materials at that time.

Therefore, the discovery of *type-II superconductors*, which were firstly proposed by A. A. Abrikosov (1957) [3], was an important breakthrough in superconductivity applications. In type-II superconductors, magnetic flux lines can *elegantly* penetrate the interior of superconductors as units of magnetic flux quanta (*vortex*), which typically resulted in high critical fields. Historically, widespread interest was sparked by Kunzler's discovery of Nb_3Sn with its extremely high upper critical field H_{c2} [4]. Currently, continuing developments have carried on in areas such as power transmission and storage, magnetic resonance imaging (MRI), superconducting quantum interference devices (SQUIDs), and magnetic levitation (*Maglev*) for mass transportation. All these applications are concurrently the focus of further research into new material synthesis, process engineering, and novel properties of superconductors, to bring forth new functionality in superconductivity.

In the same year as Abrikosov's work on type-II superconductivity, Bardeen, Cooper and Schrieffer published a theory of superconductivity that helped to understand the underlying microscopic mechanism. Their proposal was that electrons form 'Cooper pairs' through interactions between electrons mediated by phonons [5]. The Cooper pair is two coupled electrons with spins anti-aligned that can establish an energy gap between the ground state and the lowest quasiparticle excitation state. This fundamental mechanism of the BCS theory succeeded in explaining various phenomena of superconductivity.

In this Chapter, we first review the various fundamental theoretical models of superconductivity. We start with the Ginzburg-Landau (GL) theory which is powerful in discussing magnetic properties and vortex solutions. Next, the BCS theory is presented to provide microscopic interpretations to phenomenological parameters that appear in the GL theory. Keeping the unique magnetic properties of superconductivity in our mind, we overview the recently discovered superconductors. As we shall see, these superconductors, termed unconventional superconductors in this thesis, cannot be treated by conventional theories.

1.1 Ginzburg-Landau (GL) Theory

The Ginzburg-Landau (GL) theory is powerful in discussing phase transitions, symmetry breaking and the magnetic response of superconductors. The vortex state, which in this thesis is the main player we are interested in when discussing the intermediate state in superconductivity, is derived from the GL theory as first proposed by Abrikosov [3]. The GL theory introduces a pseudo-wavefunction $\psi(\mathbf{r})$ as a complex order parameter, with $|\psi(\mathbf{r})|^2$ representing the local density of superconducting electrons, $n_s(\mathbf{r})$. This theory commences with an expansion of the free-energy density in powers of $|\psi|^2$ and $|\nabla\psi|^2$. The well-known GL coupled differential equations for $\psi(\mathbf{r})$ and the vector potential $\mathbf{A}(\mathbf{r})$ are derived by applying a variational method on the free-energy density functional. Although the GL theory succeeded in explaining intermediate-state phenomena, where spatially inhomogeneous superconductivity must be analyzed, only limited attention was paid to the theory until Gor'kov revealed that the GL theory is derivable in a rigorous limit from the microscopic BCS theory for Green functions which enable spatial inhomogeneity to be treated [6]. The GL theory was proved to be in principle valid near T_c if the spatial variation of ψ and $\mathbf{A}$ are not too rapid.

In this section, we introduce following Ref. [6] the fundamental framework of the GL theory, and review how the vortex solution is derived analytically.

1.1.1 GL free-energy functional

The free-energy density f is expanded in a series of the form introducing a wavefunction-like order parameter $\psi = |\psi|e^{i\phi}$,

$$f = f_s - f_{n0} = \alpha|\psi|^2 + \frac{\beta}{2}|\psi|^4 + \frac{1}{2m^*}\left|\left(\frac{\hbar}{i}\nabla - \frac{2e}{c}\mathbf{A}\right)\psi\right|^2 + \frac{(\nabla\times\mathbf{A})^2}{8\pi}, \tag{1.1}$$

where α and β represent two phenomenological coefficients and m^* is the effective mass which depends on the material. When $\psi = 0$, this properly yields the free energy of the normal state $f_s = f_{n0} + B^2/8\pi^2$.

In the absence of magnetic fields and gradients, we have

$$f_s - f_n = \alpha|\psi|^2 + \frac{\beta}{2}|\psi|^4. \tag{1.2}$$

Evidently, the coefficient α should change sign at T_c. Making a Taylor series expansion of $\alpha(T)$ about T_c, we have

$$\alpha(T) = \alpha(0)\left(\frac{T}{T_c} - 1\right), \tag{1.3}$$

with $\alpha(0) > 0$. Figure 1.1 shows the typical behaviors of the GL free energy f at the different temperature regimes, $T > T_c$, $T = T_c$, and $T < T_c$. When $\alpha > 0$, the minimum of the free energy is fixed at $|\psi|^2 = 0$ corresponding to the normal state; otherwise, for $\alpha < 0$, the minimum occurs when

$$|\psi|^2 = |\psi_\infty|^2 = -\frac{\alpha}{\beta}, \tag{1.4}$$

where $|\psi_\infty|$ represents the absolute value of order parameter for the equilibrium state. Substituting this value back into Eq. (1.1), one finds

$$f_s - f_n = \frac{-H_{tc}^2}{8\pi} = \frac{-\alpha^2}{2\beta}, \tag{1.5}$$

where H_{tc} denotes the thermodynamic critical field.

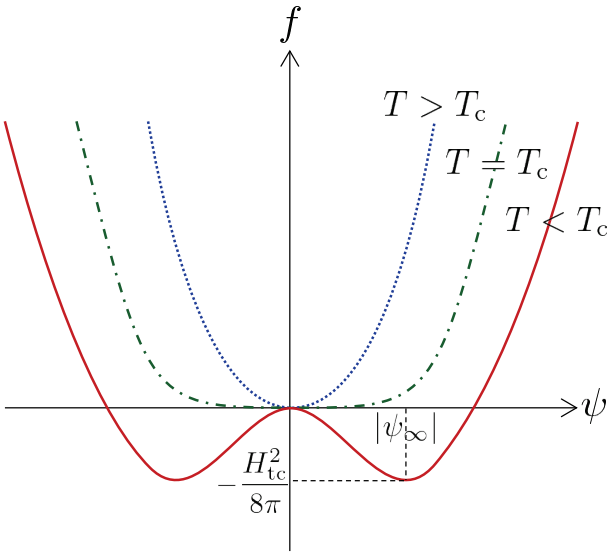

Figure 1.1: Schematics of GL free energy f at typical temperature regimes.

We next consider the remaining terms in Eq. (1.1) which deal with the gradients of ψ and vector potential $\mathbf{A}$. By the definition of the order parameter, $\psi = |\psi|e^{i\phi}$, the term is rewritten,

$$\frac{1}{2m^*}\left[\hbar^2(\nabla|\psi|)^2 + \left(\hbar\nabla\phi - \frac{2e\mathbf{A}}{c}\right)^2|\psi|^2\right]. \tag{1.6}$$

The first term gives the extra energy associated with gradients of the order parameter. The second term gives the kinetic energy associated with supercurrents in a gauge-invariant form. Becuase ϕ is constant in the London gauge,[1] it can be simply written as $(2e)^2A^2|\psi|^2/m^*c^2$. Equating this to the kinetic-energy density for a London superconductor $A^2/8\pi\lambda_{\rm eff}^2$, we find

$$\lambda_{\rm eff}^2 = \frac{m^*c^2}{4\pi|\psi|^2(2e)^2}. \tag{1.7}$$

When we identify $n_s^* = |\psi|^2$ with the total density of conduction electrons n_s^*, the expression agrees with the London penetration depth λ_L, except for the presence of the starred quantities related to effective number, mass, and charge.[2]

GL differential equations

The GL differential equations for the order parameter ψ and vector potential $\mathbf{A}$ are derived by a variational method,

$$\alpha\psi + \beta|\psi|^2\psi + \frac{1}{2m^*}\left(\frac{\hbar}{i}\nabla - \frac{2e}{c}\mathbf{A}\right)^2\psi = 0, \tag{1.8}$$

and

$$\mathbf{J} = \frac{c}{4\pi}\mathrm{rot}\mathbf{B} = \frac{2e\hbar}{2m^*i}(\psi^*\nabla\psi - \psi\nabla\psi^*) - \frac{(2e)^2}{m^*c}\psi\psi^*\mathbf{A}, \tag{1.9}$$

or equivalently,

$$\mathbf{J} = \frac{2e}{m^*}|\psi|^2\left(\hbar\nabla\phi - \frac{2e}{c}\mathbf{A}\right) - 2e|\psi|^2\mathbf{v}_{\rm s}. \tag{1.10}$$

[1] The London gauge requires setting $\nabla\cdot\mathbf{A} = 0$.

[2] According to the London equations, developed by brothers Fritz and Heinz London, the penetration depth is derived as $\lambda_L(0) = (mc^2/4\pi n_s e^2)^{1/2}$ with the temperature dependent quantity n_s decreasing continuously to zero as $T \to T_{\rm c}$.

The coherence length ξ is derived from Eq. (1.8) by treating the problem for zero-magnetic field $\mathbf{A} = 0$, and hence we can take ψ to be real valued. We here consider the distortion of the order parameter δ from the bulk value $\psi = (1+\delta)\psi_\infty$, where $\psi_\infty^2 = -\alpha/\beta$. The GL equation Eq. (1.8) is then reduced to,

$$(\alpha + 3\beta\psi_\infty^2)\delta = \frac{\hbar^2}{2m^*}\frac{d^2\delta}{dx^2}. \tag{1.11}$$

Introducing the wavefunction $\delta = A\exp(-\sqrt{2}x/\xi)$, the equation for the coherence length ξ is found to be

$$\xi^2 = \frac{\hbar^2}{2m^*|\alpha|}. \tag{1.12}$$

The London penetration depth λ also is obtained from the GL equation for supercurrents in Eq. (1.10) multiplying ∇,

$$\nabla \times \nabla \times \mathbf{B} = -\frac{4\pi|\psi|^2(2e)^2}{m^*c^2}\mathbf{B}, \tag{1.13}$$

with $\nabla \times \mathbf{A} = \mathbf{B}$ and $\nabla\phi = 0$. This can be transformed by a vector identity to the London's equation coupled with the Maxwell equation, namely $\nabla^2\mathbf{B} = \mathbf{B}/\lambda$. One then finds,

$$\lambda^{-2} = \frac{4\pi|\psi|^2(2e)^2}{m^*c^2}. \tag{1.14}$$

Let us next discuss the nucleation field of a superconductor in a bulk sample in the presence of fields $\mathbf{H}$ along the z axis. We here consider the linearized GL equation in which the term $\beta|\psi|^2\psi$ is neglected,

$$\left(\frac{\nabla}{i} - \frac{2\pi}{\Phi_0}\mathbf{A}\right)^2 \psi = -\frac{2m^*\alpha}{\hbar^2}\psi \equiv \frac{\psi}{\xi^2}. \tag{1.15}$$

This is appropriate only when the order parameter ψ becomes much smaller than the bulk value ψ_∞ in magnetic fields. Introducing a convenient gauge choice $A_y = Hx$ and $A_x = A_z = 0$, the linearized GL equation can be modified and it is reasonable to look for a solution of the form,

$$\psi = e^{ik_y y}e^{ik_z z}f(x). \tag{1.16}$$

Substituting this into Eq. (1.15), we find

$$-f''(x) + \left(\frac{2\pi H}{\Phi_0}\right)^2 (x - x_0)^2 f = \left(\frac{1}{\xi^2} - k_z^2\right) f, \tag{1.17}$$

where

$$x_0 = \frac{k_y\Phi_0}{2\pi H}. \tag{1.18}$$

Multiplying by $\hbar^2/2m^*$, we immediately notice that the form is the same as the Schrödinger equation for a particle of mass m^* bounded in a harmonic oscillator potential with constant force $(2\pi\hbar H/\Phi_0)^2/m^*$. This is formally solved in analogy with the quantized states of a charged particle in a magnetic field and yields the Landau level solution. The resulting eigenvalues are

$$\epsilon_n = \left(n + \frac{1}{2}\right)\hbar\omega_c = \left(n + \frac{1}{2}\right)\hbar\left(\frac{2eH}{m^*c}\right), \tag{1.19}$$

and the eigenfunction yields

$$H = \frac{\Phi_0}{2\pi(2n+1)}\left(\frac{1}{\xi^2} - k_z^2\right). \tag{1.20}$$

The highest value occurs when $k_z = 0$ and $n = 0$, which correspond to the nucleation field H_n, or in other words, the upper critical field $H_{\mathrm{c}2}$,

$$H_\mathrm{n} = \frac{\Phi_0}{2\pi\xi^2}. \tag{1.21}$$

Relating the nucleation field $H_{\rm n}$ in Eq. (1.21) and the thermodynamic $H_{\rm tc}$ in Eq. (1.5), we arrive at the simple expression,

$$H_{\rm n} = \sqrt{2}\kappa H_{\rm tc}, \tag{1.22}$$

where $\kappa \equiv \lambda/\xi$ is the well-known *GL parameter* which depends only on material properties. The threshold value $\kappa = 1/\sqrt{2}$ indeed classifies superconductors as either type-I ($H_{\rm n} < H_{\rm tc}$) or type-II ($H_{\rm n} > H_{\rm tc}$). For type-II superconductors, one meets to $H_{\rm n}$ in decreasing magnetic fields, and $|\psi|^2$ starts to grow continuously from zero in a second-order transition. On the other hand, type-I superconductors in decreasing field would be *supercooled* from $H_{\rm tc}$ until ideally $H_{\rm n}$, and exhibit discontinuous and irreversible jump of $|\psi|^2$ to ψ_∞^2 in a first-order transition.

1.1.2 Classification of superconductivity

As proposed in A. A. Abrikosov's pioneering work [3], the classification of superconductors was originally discussed based on the GL theory investigating the interface energy between the superconducting and normal domains. We seek solutions of the differential equations Eq. (1.8) and (1.9) subject to the following boundary conditions:

$$\begin{array}{ll} \psi = \psi_\infty \text{ and } B = 0 & \text{for } x \to +\infty \\ \psi = 0 \text{ and } B = H_{\rm tc} & \text{for } x \to -\infty \end{array}$$

We here consider a one-dimensional problem, and take ψ as real. The calculation of the interface energy corresponds to evaluating the excess Gibbs free energy at $H_{\rm tc}$,

$$\begin{aligned} \Gamma &= \int_{-\infty}^{+\infty} (g_{sH} - g_{s0}) dx = \int_{-\infty}^{+\infty} \left(f_{sH} - \frac{BH_{\rm tc}}{4\pi} - f_{s0} \right) dx \\ &= \int_{-\infty}^{+\infty} \left[\alpha|\psi|^2 + \frac{\beta}{2}|\psi|^4 + \frac{1}{2m^*} \left| \left(\frac{\hbar}{i}\nabla - \frac{2e}{c}\mathbf{A} \right) \psi \right|^2 + \frac{(B - H_{\rm tc})^2}{8\pi} \right] dx, \end{aligned} \tag{1.23}$$

where $f_{n0} - f_{s0} = H_{\rm tc}^2/8\pi$ is used. This can be further simplified using the relation obtained from the integrated GL equation in Eq. (1.8)

$$0 = \int_{-\infty}^{+\infty} \left[\alpha|\psi|^2 + \beta|\psi|^4 + \frac{1}{2m^*} \left| \left(\frac{\hbar}{i}\nabla - \frac{2e}{c}\mathbf{A} \right) \psi \right|^2 \right] dx. \tag{1.24}$$

Subtracting this from Eq. (1.23), the interface energy is obtained with equating to $(H_{\rm tc}^2/8\pi)\delta$ as,

$$\delta = \int_{-\infty}^{+\infty} \left[\left(1 - \frac{B}{H_{\rm tc}} \right)^2 - \left(\frac{\psi}{\psi_\infty} \right)^2 \right]. \tag{1.25}$$

Therefore, there is a crossover from positive to negative interface energy which was first illuminated by Abrikosov in superconductors that he termed type-II. Although analytic calculations of the interface energy for all parameter regime is difficult, the crossover is numerically proved to occur at $\kappa = 1/\sqrt{2}$. Moreover, an important consequence is that the crossover of sign in the interface energy at $\kappa = 1/\sqrt{2}$ coincides to the relation $H_{\rm tc} = H_{\rm n}$. In a type-II superconductor, magnetic fields penetrate into a superconductor in units of quantized flux $\Phi_0 = hc/2e = 2.07 \times 10^{-15}$Wb to utilize the negative interface energy. Giving the name *vortex*, they result typically in high upper-critical-field ($H_{\rm c2}$) enabling industrial applications.

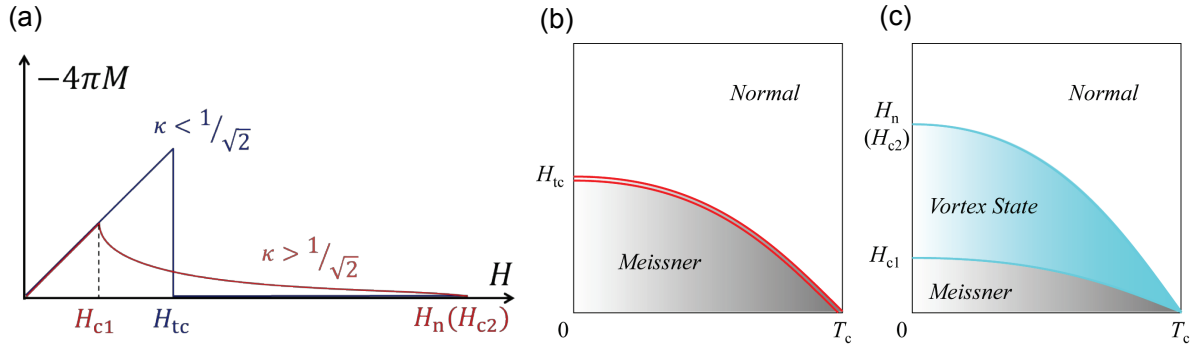

Figure 1.2: (a) Typical M-H curves for type-I and type-II superconductors. Schematics of H-T phase diagrams for (b) type-I superconductors and (c) type-II superconductors. The double and single lines represent first- and second-order transition, respectively.

1.1.3 Magnetic properties of type-II superconductors

A typical magnetic feature of superconductors subject to small applied magnetic fields is the well-known Meissner effect, in which the applied is excluded from the superconductor, producing perfect diamagnetism. Nevertheless, as discussed in the previous section, superconductors are classified as either type-I or -II depending on whether $H_n < H_{tc}$ ($\kappa < 1/\sqrt{2}$) or $H_n > H_{tc}$ ($\kappa > 1/\sqrt{2}$), respectively; Fig. 1.2 shows schematics of typical H-T phase diagrams and magnetization curves (M-H curves for short). We here discuss an analytical derivation of the vortex states that contributes the building block of the vortex structure.

Structure of single vortex

When magnetic fluxes penetrate a type-II superconductor, the vortices are distributed sparsely forming an array throughout the material. As long as the separation is larger than λ, the interaction between vortices is negligible, and one can treat them as being isolated.

Given the axial symmetry of the situation, the problem is reduced to finding a self-consistent solution of the GL equations for $\psi(r)$ and $B(r)$. Hence one can calculate the extra free energy ϵ_1 per unit length of the line given a definition of the lower critical field H_{c1}, where the Gibbs free energy must have the same value whether the first vortex is inside or outside the sample,

$$G_s|_{\text{no flux}} = G_s|_{\text{first vortex}}. \tag{1.26}$$

Because $G = F - (H/4\pi)\int B d\mathbf{r}$ and $G_s = F_s$ in the absence of a flux, the condition becomes

$$\begin{aligned} F_s &= F_s + \epsilon_1 L - \frac{H_{c1}\int B d\mathbf{r}}{4\pi} \\ &= F_s + \epsilon_1 L - \frac{H_{c1}\Phi_0 L}{4\pi}, \end{aligned} \tag{1.27}$$

where L is the length of the vortex line in the sample. Therefore, one has

$$H_{c1} = \frac{4\pi\epsilon_1}{\Phi_0}. \tag{1.28}$$

The calculation of ψ, B and ϵ_1 for arbitrary κ unfortunately requires a numerical solution of the GL equation. Therefore, considerable attention has been given to the extreme type-II limit, in which $\kappa = \lambda/\xi \gg 1$, where useful analytical results can be obtained.

We here try to approach the full solution of the nonlinear GL equations. It is convenient to introduce a vortex wavefunction of the form

$$\psi = \psi_\infty f(r) e^{i\theta}, \tag{1.29}$$

which complies with the axial symmetry and the fact that the phase of ψ varies by 2π. This actually corresponds to the existence of a single flux quantum associated with vortex currents. This phase choice for ψ fixes the gauge choice for $\mathbf{A}$ so that

$$\mathbf{A} = A(r)\hat{\theta}, \tag{1.30}$$

with

$$A(r) = \left(\frac{1}{r}\right)\int_0^r r'B(r')dr'. \tag{1.31}$$

Near the center of the vortex, this becomes

$$A_{r\to 0} = \frac{B(0)r}{2}, \tag{1.32}$$

whereas far from the center of an isolated vortex, it becomes

$$A_{r\to\infty} = \frac{\Phi_0}{2\pi r}, \tag{1.33}$$

as the total flux contained is $\oint \mathbf{A}\cdot d\mathbf{s} = 2\pi r A_\infty = \Phi_0$.

When Eq. (1.29) is substituted into the GL equation, we find after simplifying that f satisfies

$$f - f^3 - \xi^2\left[\left(\frac{1}{r} - \frac{2\pi A}{\Phi_0}\right)^2 f - \frac{1}{r}\frac{d}{dr}\left(r\frac{df}{dr}\right)\right] = 0. \tag{1.34}$$

The current has only one component, that associated with θ, and from the GL equation it is

$$J = -\frac{c}{4\pi}\frac{dB(r)}{dr} = -\frac{c}{4\pi}\frac{d}{dr}\left[\frac{1}{r}\frac{d}{dr}(rA)\right] = \frac{e^*\hbar}{m^*}\psi_\infty^2 f^2\left(\frac{1}{r} - \frac{2\pi A}{\Phi_0}\right). \tag{1.35}$$

The problem is now to find simultaneous solutions of these two nonlinear differential equations for $f(r)$ and $A(r)$. Because this requires numerical methods in general, we examine certain limit cases which enable analytical treatments.

First, let us look at the center of the vortex, as $r \to 0$. Using Eq. (1.32), Eq. (1.34) becomes

$$f - f^3 - \xi^2\left[\left(\frac{1}{r} - \frac{\pi B(0)r}{\Phi_0}\right)^2 f - \frac{1}{r}\frac{d}{dr}\left(r\frac{df}{dr}\right)\right] = 0. \tag{1.36}$$

Let us assume that the solution starts as $f = cr^n$ with $n \geq 0$, then Eq. (1.36) becomes

$$cr^n - c^3 r^{3n} - \xi^2\left[\left(\frac{1}{r} - \frac{\pi B(0)r}{\Phi_0}\right)^2 cr^n - n^2 cr^{n-2}\right] = 0. \tag{1.37}$$

As $r \to 0$, the leading term is proportional to $r^{n-2}(1-n^2)$. For this to vanish, $n = 1$ and f must start out proportional to r at the core. Seeing the structure in Eq. (1.36), only odd powers of r now enter the expansion of f. Working out the coefficient of the next term, we find

$$f(r) \approx cr\left\{1 - \frac{r^2}{8\xi^2}\left[1 + \frac{B(0)}{H_{c2}}\right]\right\}, \tag{1.38}$$

which shows that the rise of $f(r)$ starts to saturate at $r \approx 2\xi$. To get the normalization constant c, we must go further to bring the f^3 term into play. However, it is clear that c must be $\sim 1/2\xi$ for isolated vortices, so that the series in Eq. (1.38) matches the long-distance behavior, where $f \to 1$. A reasonable approximation to f over the entire range is

$$f \approx \tanh\frac{\nu r}{\xi}, \tag{1.39}$$

where ν is a constant ~ 1.

High-κ approximation

Because the order parameter recovers almost to unity in a distance $\sim \xi$, we can make a convenient approximation when $\lambda \gg \xi$, or equivalently $\kappa \gg 1$. we treat f as a constant $\simeq 1$ where the London equations govern the field and currents outside the core except for a core region with radius $\sim \xi$, namely,

$$\frac{4\pi\lambda^2}{c}\text{rot}\mathbf{J}_s + \mathbf{B} = 0. \tag{1.40}$$

This relation should be modified by inserting a term that considers the presence of the core,

$$\frac{4\pi\lambda^2}{c}\text{rot}\mathbf{J}_s + \mathbf{B} = \hat{\mathbf{z}}\Phi_0\delta_2(\mathbf{r}), \tag{1.41}$$

where $\hat{\mathbf{z}}$ is a unit vector along the vortex and $\delta_2(\mathbf{r})$ is a two-dimensional δ function as the location of the core. Combining Eq. (1.41) with the Maxwell equation $\text{rot}\mathbf{B} = (4\pi/c)\mathbf{J}$, we obtain

$$\lambda^2\text{rot rot}\mathbf{B} + \mathbf{B} = \hat{\mathbf{z}}\Phi_0\delta_2(\mathbf{r}). \tag{1.42}$$

As $\text{div}\mathbf{B} = 0$, this can be written

$$\nabla^2\mathbf{B} - \frac{\mathbf{B}}{\lambda^2} = -\frac{\Phi_0}{\lambda^2}\hat{\mathbf{z}}\delta_2(\mathbf{r}). \tag{1.43}$$

This equation has an exact solution

$$B(r) = \frac{\Phi_0}{2\pi\lambda^2}K_0\left(\frac{r}{\lambda}\right), \tag{1.44}$$

where K_0 is a zeroth-order Bessel function. At large distances, $K_0(r/\lambda)$ behaves approximately as $e^{-r/\lambda}$ but diverges logarithmically as $\ln(\lambda/r)$ when $r \to 0$. Noted that the divergence of Eq. (1.44) is cut off at $r \sim \xi$ where $|\psi|^2$ starts dropping to zero, and thus $B(r)$ is actually regular at the center of the vortex.

For our reference, the typical structure of a single vortex is shown in Fig. 1.3(a), where the order parameter is suppressed within a scale of coherence length ξ and supercurrents localize within a range of penetration depth λ. Figure 1.3(b) shows the structure of the order parameter associated with phase ϕ in the x-y coordinate. Based on the penetration of magnetic fluxes, type-II superconductors exhibit an intermediate state that is associated with a triangular lattice structure within a sample.

Vortex line energy

We next consider the vortex-line tension, namely the free energy per unit length ϵ_1. Neglecting the core, we have only the contributions from the field energy and the kinetic energy of the currents,

$$\epsilon_1 = \frac{1}{8\pi}\int (B^2 + \lambda^2|\text{rot}\mathbf{B}|^2)dS. \tag{1.45}$$

This can be transformed by a vector identity to

$$\begin{aligned}\epsilon_1 &= \frac{1}{8\pi}\int (\mathbf{B} + \lambda^2\text{rot rot}\mathbf{B})\cdot\mathbf{B}dS + \frac{\lambda^2}{8\pi}\oint(\mathbf{B}\times\text{rot}\mathbf{B})\cdot\mathbf{B}d\mathbf{s} \\ &= \frac{1}{8\pi}\int |\mathbf{B}|\Phi_0\delta_2(\mathbf{r})dS + \frac{\lambda^2}{8\pi}\oint(\mathbf{B}\times\text{rot}\mathbf{B})\cdot d\mathbf{s},\end{aligned} \tag{1.46}$$

where the line integrals around the inner and outer perimeter of the integration exclude the core. The first term contributes nothing, whereas the second term goes to zero at infinity but gives a finite contribution in encircling the core, specifically,

$$\epsilon_1 = \frac{\lambda^2}{8\pi}\left[B\frac{dB}{dr}2\pi r\right]_\xi. \tag{1.47}$$

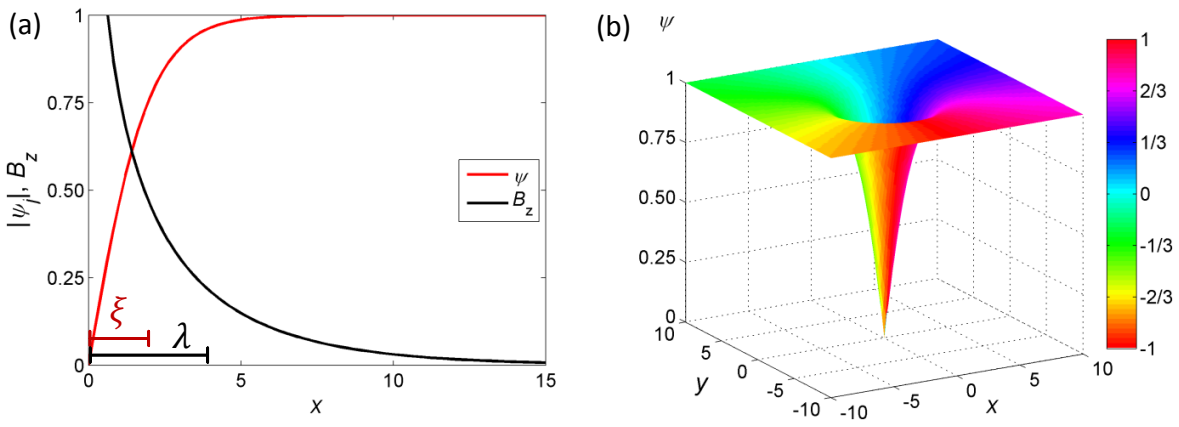

Figure 1.3: Analytic results of a vortex structure for $\kappa = 2$. (a) Radial dependence of order parameter $\psi(r)$ and $B_z(r)$ from the center ($r = 0$) of a single vortex. Amplitude of order parameter and B_z are normalized by bulk value ψ_∞ and the thermodynamic field $H_{\rm tc}$, respectively. (b) Spatial distribution of the order parameter colored in terms of phase ϕ.

Using $dB/dr = \Phi_0/2\pi\lambda^2 r$, this reduces to

$$\epsilon_1 = \frac{\Phi_0}{8\pi} B(\xi) \approx \frac{\Phi_0}{8\pi} B(0), \tag{1.48}$$

where $B(\xi) \approx B(0)$ because $f \to 0$, and hence $J_s \to 0$ in the core. Imposing a cut-off approximation at ξ, we have

$$\epsilon_1 \approx \left(\frac{\Phi_0}{4\pi\lambda}\right)^2 \ln\kappa, \tag{1.49}$$

which depends logarithmically on core size. This is straightforwardly reformulated into more physical terms using the relation $\Phi_0 = 2\sqrt{2}\pi\lambda\xi H_c$,

$$\epsilon_1 = \frac{H_c^2}{8\pi} 4\pi\xi^2 \ln\kappa, \tag{1.50}$$

which shows that the line energy is of the same order as the condensation energy lost in the core, but larger by a factor of order $4\ln\kappa$.[3]

Interaction between vortices

Based on the approximation $\kappa \gg 1$, it is easy to treat the interaction energy between two vortices. The magnetic field in the presence of two vortices is given by the field superposition

$$\begin{aligned} \mathbf{B}(\mathbf{r}) &= \mathbf{B}_1(\mathbf{r}) + \mathbf{B}_2(\mathbf{r}) \\ &= [B(|\mathbf{r} - \mathbf{r}_1|) + B(|\mathbf{r} - \mathbf{r}_2|)]\hat{\mathbf{z}}, \end{aligned} \tag{1.51}$$

where $\mathbf{r}_1$ and $\mathbf{r}_2$ specify the core positions of the two vortex lines and $B(r)$ is given by Eq. (1.44). The energy is calculated by substituting this into Eq. (1.50) and using vector transformations, resulting in a total increase in free energy per unit length,

$$\begin{aligned} \Delta F &= \frac{\Phi_0}{8\pi}[B_1(\mathbf{r}_1) + B_1(\mathbf{r}_2) + B_2(\mathbf{r}_1) + B_2(\mathbf{r}_2)] \\ &= 2\left[\frac{\Phi_0}{8\pi} B_1(\mathbf{r}_1)\right] + \frac{\Phi_0}{4\pi} B_1(\mathbf{r}_2). \end{aligned} \tag{1.52}$$

[3] Therefore, errors in handling the core should be unimportant for $\kappa \gg 1$.

The first term represents simply the sum of the two individual line energies. The second term is the sought-after interaction energy

$$F_{12} = \frac{\Phi_0 B_1(\mathbf{r}_2)}{4\pi} = \frac{\Phi_0^2}{8\pi^2\lambda^2} K_0\left(\frac{r_{12}}{\lambda}\right). \tag{1.53}$$

This energy falls off as $r_{12}^{-1/2} e^{-r_{12}/\lambda}$ at large distances and varies logarithmically at small distances. The interaction is repulsive for the usual case in which the fluxes have the same rotational sense within the two vortices.

We calculate the force arising from the interaction by taking the derivative of F_{12} in Eq. (1.53). For example, the force on line 2 in the x direction is

$$f_{2x} = -\frac{\partial F_{12}}{\partial x_2} = -\frac{\Phi_0}{4\pi}\frac{\partial B_1(\mathbf{r}_2)}{\partial x_2} = \frac{\Phi_0}{c} J_{1y}(\mathbf{r}_2), \tag{1.54}$$

using the Maxwell equation $\mathrm{rot}\mathbf{B} = 4\pi\mathbf{J}/c$. Putting this back into a vector form, the force per unit length on vortex 2 is

$$\mathbf{f}_2 = \mathbf{J}_1(\mathbf{r}_2) \times \frac{\mathbf{\Phi}_0}{c}, \tag{1.55}$$

where the direction of $\mathbf{\Phi}_0$ is parallel to the flux density. Generalizing to an arbitrary array, we obtain

$$\mathbf{f} = \mathbf{J}_\mathrm{s} \times \frac{\mathbf{\Phi}_0}{c}, \tag{1.56}$$

where $\mathbf{J}_\mathrm{s}$ represents the total supercurrent density caused by all other vortices and also includes any net transport currents at the location of the vortex core.

This result indicates that an array of vortices feels finite transverse forces from any transport current; hence vortices will move unless they are pinned by inhomogeneities such as dislocations, defects or impurities. Such flux motion causes finite energy dissipation and induces a longitudinal resistive voltage, which is crucial for any applications of type-II superconductors used for strong currents or fields.

1.2 Bardeen-Cooper-Schrieffer (BCS) Theory

As we have seen in the GL free-energy functional in Eq. (1.1), the coefficients α and β are phenomenological parameters, and their microscopic definitions are unclear. As demonstrated by L. P. Gor'kov [7], the GL theory can be connected with the celebrated microscopic theory, namely the Bardeen-Cooper-Schrieffer (BCS) theory. Although the original work by Gor'kov based on the Green functions enables us to fully access microscopical definitions in the GL theory,[4] We here discuss simply the derivation of GL formalism by analyzing a BCS gap function obtained by the mean-field approximation to provide a basic understanding to show consistency between the BCS and GL theories.

1.2.1 Mean-field approximation

We start from the well-established *reduced BCS Hamiltonian* where necessary interactions between electrons $(\mathbf{k}, \uparrow)$ and $(-\mathbf{k}, \downarrow)$ to form the Cooper pairs are neglected,

$$\mathcal{H} = \sum_{\mathbf{k},\sigma} \xi_\mathbf{k} n_{\mathbf{k}\sigma} + \sum_{\mathbf{k},\mathbf{k}'} V_{\mathbf{k},\mathbf{k}'} c^\dagger_{\mathbf{k}\uparrow} c^\dagger_{-\mathbf{k}\downarrow} c_{-\mathbf{k}'\downarrow} c_{\mathbf{k}'\uparrow}, \tag{1.57}$$

[4] As we shall soon see, the inhomogeneity term which corresponds to the kinetic term in GL functionals cannot be discussed.

where $n_{\mathbf{k}\sigma} = c^\dagger_{\mathbf{k}\sigma} c_{-\mathbf{k}\sigma}$ is the particle number operator and

$$\xi_{\mathbf{k}} = \epsilon_{\mathbf{k}} - \mu = \frac{\hbar^2 \mathbf{k}^2}{2m} - \mu \tag{1.58}$$

is the kinetic energy of a free electron measured from the chemical potential μ.

We are going to calculate various physical properties of superconductors at finite temperature. However, it is inconvenient to treat the interaction term in Eq. (1.57). We here consider a mean-field approximation based on the *pair operators*

$$\begin{aligned} b^\dagger_{\mathbf{k}} &= c^\dagger_{\mathbf{k}\uparrow} c^\dagger_{-\mathbf{k}\downarrow}, \\ b_{\mathbf{k}} = (b^\dagger_{\mathbf{k}})^\dagger &= (c^\dagger_{\mathbf{k}\uparrow} c^\dagger_{-\mathbf{k}\downarrow})^\dagger = c_{-\mathbf{k}\downarrow} c_{\mathbf{k}\uparrow}, \end{aligned} \tag{1.59}$$

which yield averages in terms of the BCS state,

$$\begin{aligned} \bar{b}^*_{\mathbf{k}} &= \langle \Psi_{\rm BCS} | b^\dagger_{\mathbf{k}} | \Psi_{\rm BCS} \rangle = u_{\mathbf{k}} v^*_{\mathbf{k}}, \\ \bar{b}_{\mathbf{k}} &= \langle \Psi_{\rm BCS} | b_{\mathbf{k}} | \Psi_{\rm BCS} \rangle = u^*_{\mathbf{k}} v_{\mathbf{k}}, \end{aligned} \tag{1.60}$$

and take deviations from the average $\delta b^\dagger_{\mathbf{k}}$, $\delta b_{\mathbf{k}}$, one finds,

$$\begin{aligned} b^\dagger_{\mathbf{k}} &= \bar{b}^*_{\mathbf{k}} + \delta b^\dagger_{\mathbf{k}}, \\ b_{\mathbf{k}} &= \bar{b}_{\mathbf{k}} + \delta b_{\mathbf{k}}. \end{aligned} \tag{1.61}$$

Neglecting quadratic terms in $\delta b^\dagger_{\mathbf{k}}$ and $\delta b_{\mathbf{k}}$, the interaction term in the reduced Hamiltonian of Eq. (1.57) can be thenreby rewritten as,

$$\begin{aligned} \sum_{\mathbf{k},\mathbf{k}'} V_{\mathbf{k},\mathbf{k}'} c^\dagger_{\mathbf{k}\uparrow} c^\dagger_{-\mathbf{k}\downarrow} c_{-\mathbf{k}'\downarrow} c_{\mathbf{k}'\uparrow} &= \sum_{\mathbf{k},\mathbf{k}'} V_{\mathbf{k},\mathbf{k}'} b^\dagger_{\mathbf{k}} b_{\mathbf{k}'} \\ &\approx \sum_{\mathbf{k},\mathbf{k}'} V_{\mathbf{k},\mathbf{k}'} \left(\bar{b}^*_{\mathbf{k}} b_{\mathbf{k}'} + \bar{b}_{\mathbf{k}'} b^\dagger_{\mathbf{k}} \right) - \sum_{\mathbf{k},\mathbf{k}'} V_{\mathbf{k},\mathbf{k}'} \bar{b}^*_{\mathbf{k}} \bar{b}_{\mathbf{k}'} \\ &= -\sum_{\mathbf{k}} \left(\Delta^*_{\mathbf{k}} b_{\mathbf{k}} + \Delta_{\mathbf{k}} b^\dagger_{\mathbf{k}} \right) + \frac{1}{2} \sum_{\mathbf{k}} \left(\Delta^*_{\mathbf{k}} \bar{b}_{\mathbf{k}} + \Delta_{\mathbf{k}} \bar{b}^*_{\mathbf{k}} \right), \end{aligned} \tag{1.62}$$

where we define

$$\begin{aligned} \Delta^*_{\mathbf{k}} &\equiv -\sum_{\mathbf{k}'} V_{\mathbf{k},\mathbf{k}'} \bar{b}^*_{\mathbf{k}'}, \\ \Delta_{\mathbf{k}} &\equiv -\sum_{\mathbf{k}'} V_{\mathbf{k},\mathbf{k}'} \bar{b}_{\mathbf{k}'}. \end{aligned} \tag{1.63}$$

The reduced BCS Hamiltonian thereby takes the form

$$\begin{aligned} \mathcal{H}_{\rm MF} = &\sum_{\mathbf{k}} \xi_{\mathbf{k}} \left(c^\dagger_{\mathbf{k}\uparrow} c_{\mathbf{k}\uparrow} + c^\dagger_{-\mathbf{k}\downarrow} c_{-\mathbf{k}\downarrow} \right) \\ &- \sum_{\mathbf{k}} \left(\Delta^*_{\mathbf{k}} c_{-\mathbf{k}\downarrow} c_{\mathbf{k}\uparrow} + \Delta_{\mathbf{k}} c^\dagger_{\mathbf{k}\uparrow} c^\dagger_{-\mathbf{k}\downarrow} \right) + \frac{1}{2} \sum_{\mathbf{k}} \left(\Delta^*_{\mathbf{k}} \bar{b}_{\mathbf{k}} + \Delta_{\mathbf{k}} \bar{b}^*_{\mathbf{k}} \right). \end{aligned} \tag{1.64}$$

This Hamiltonian can be diagonalized by a suitable linear transformation, namely the Bogoliubov-Balatin transformation, to define new Fermi operators $\gamma_{\mathbf{k}}$

$$\begin{aligned} c_{\mathbf{k}\uparrow} &= u^*_{\mathbf{k}} \gamma_{\mathbf{k}\uparrow} + v_{\mathbf{k}} \gamma^\dagger_{-\mathbf{k}\downarrow}, \\ c^\dagger_{-\mathbf{k}\downarrow} &= -v^*_{\mathbf{k}} \gamma_{\mathbf{k}\uparrow} + u_{\mathbf{k}} \gamma^\dagger_{-\mathbf{k}\downarrow}, \end{aligned} \tag{1.65}$$

where the numerical coefficients $u_{\mathbf{k}}$ and $v_{\mathbf{k}}$ satisfy the condition $|u_{\mathbf{k}}|^2 + |v_{\mathbf{k}}|^2 = 1$. The full form of the mean-field Hamiltonian is

$$\begin{aligned}\mathcal{H}_{\mathrm{MF}} = &\sum_{\mathbf{k}} \left[2\xi_{\mathbf{k}} |v_{\mathbf{k}}|^2 - \left(\Delta_{\mathbf{k}}^* u_{\mathbf{k}}^* v_{\mathbf{k}} + \Delta_{\mathbf{k}} u_{\mathbf{k}} v_{\mathbf{k}}^* \right) + \frac{1}{2} \left(\Delta_{\mathbf{k}}^* \bar{b}_{\mathbf{k}} + \Delta_{\mathbf{k}} \bar{b}_{\mathbf{k}}^* \right) \right] \\ &+ \sum_{\mathbf{k}} \left[\xi_{\mathbf{k}} \left(|u_{\mathbf{k}}|^2 - |v_{\mathbf{k}}|^2 \right) + \Delta_{\mathbf{k}}^* u_{\mathbf{k}}^* v_{\mathbf{k}} + \Delta_{\mathbf{k}} u_{\mathbf{k}} v_{\mathbf{k}}^* \right] \left(\gamma_{\mathbf{k}\uparrow}^\dagger \gamma_{\mathbf{k}\uparrow} + \gamma_{-\mathbf{k}\downarrow}^\dagger \gamma_{-\mathbf{k}\downarrow} \right) \\ &+ \sum_{\mathbf{k}} \left(2\xi_{\mathbf{k}} u_{\mathbf{k}} v_{\mathbf{k}} - \Delta_{\mathbf{k}} u_{\mathbf{k}}^2 + \Delta_{\mathbf{k}}^* v_{\mathbf{k}}^2 \right) \gamma_{\mathbf{k}\uparrow}^\dagger \gamma_{-\mathbf{k}\downarrow}^\dagger + \sum_{\mathbf{k}} \left(2\xi_{\mathbf{k}} u_{\mathbf{k}}^* v_{\mathbf{k}}^* - \Delta_{\mathbf{k}}^* u_{\mathbf{k}}^{*2} + \Delta_{\mathbf{k}}^* v_{\mathbf{k}}^{*2} \right) \gamma_{-\mathbf{k}\downarrow} \gamma_{\mathbf{k}\uparrow} \end{aligned} \tag{1.66}$$

This can be diagonalized when $u_{\mathbf{k}}$ and $v_{\mathbf{k}}$ are chosen so that the coefficients of $\gamma_{\mathbf{k}\uparrow}\gamma_{-\mathbf{k}\downarrow}$ and $\gamma_{\mathbf{k}\uparrow}^\dagger \gamma_{-\mathbf{k}\downarrow}^\dagger$ vanish which are physically unimportant, specifically,

$$2\xi_{\mathbf{k}} u_{\mathbf{k}} v_{\mathbf{k}} + \Delta_{\mathbf{k}}^* v_{\mathbf{k}}^2 - \Delta_{\mathbf{k}} u_{\mathbf{k}}^2 = 0. \tag{1.67}$$

Multiplying through by $\Delta_{\mathbf{k}}^*/u_{\mathbf{k}}^2$ and solving using the quadratic formula, the above diagonalization condition yields

$$\frac{\Delta_{\mathbf{k}}^* v_{\mathbf{k}}}{u_{\mathbf{k}}} = \left(\xi_{\mathbf{k}}^2 + |\Delta_{\mathbf{k}}|^2 \right)^{1/2} - \xi_{\mathbf{k}} = E_{\mathbf{k}} - \xi_{\mathbf{k}}, \tag{1.68}$$

where $E_{\mathbf{k}} = \sqrt{\xi_{\mathbf{k}}^2 + |\Delta_{\mathbf{k}}|^2}$. Imposing the normalization condition $|u_{\mathbf{k}}|^2 + |v_{\mathbf{k}}|^2 = 1$ and using the relation $|v_{\mathbf{k}}/u_{\mathbf{k}}| = (E_{\mathbf{k}} - \xi_{\mathbf{k}})/|\Delta_{\mathbf{k}}|$, we can solve for the coefficients obtaining

$$|v_{\mathbf{k}}|^2 = 1 - |u_{\mathbf{k}}|^2 = \frac{1}{2} \left(1 - \frac{\xi_{\mathbf{k}}}{E_{\mathbf{k}}} \right). \tag{1.69}$$

The diagonalized Hamiltonian is finally reduced using the above relations,

$$\mathcal{H}'_{\mathrm{MF}} = \sum_{\mathbf{k}} \left(\xi_{\mathbf{k}} - E_{\mathbf{k}} + \Delta_{\mathbf{k}} b_{\mathbf{k}} \right) + \sum_{\mathbf{k}} E_{\mathbf{k}} \left(\gamma_{\mathbf{k}\uparrow}^\dagger \gamma_{\mathbf{k}\uparrow} + \gamma_{-\mathbf{k}\downarrow}^\dagger \gamma_{-\mathbf{k}\downarrow} \right). \tag{1.70}$$

The second term can be interpreted as the particle number operators for quasi-particles of up-spin and down-spin, that is $\gamma_{\mathbf{k}\uparrow}^\dagger \gamma_{\mathbf{k}\uparrow} = n_{\mathbf{k}\uparrow}$ and $\gamma_{-\mathbf{k}\downarrow}^\dagger \gamma_{-\mathbf{k}\downarrow} = n_{-\mathbf{k}\downarrow}$. The Hamiltonian obtained here is therefore equivalent to that of a free-electron system except for the first term which correspond to the BCS ground state. The quasi-particles excited from the BCS ground state are considered as Fermi particles with excitation energy $E_{\mathbf{k}}$ within the mean-field approximation.

1.2.2 Gap function for finite temperatures

Having identified $E_{\mathbf{k}}$ as the excitation energy of a Fermion quasi-particle, it must be a positive quantity as $E_{\mathbf{k}} \geq \Delta_{\mathbf{k}}$. The probability for a quasiparticle to be excited at thermal equilibrium is given by the Fermi-Dirac distribution function,

$$\langle \gamma_{\mathbf{k}\uparrow}^\dagger \gamma_{\mathbf{k}\uparrow} \rangle (= \langle \gamma_{-\mathbf{k}\downarrow}^\dagger \gamma_{-\mathbf{k}\downarrow} \rangle) = f(E_{\mathbf{k}}) = (e^{\beta E_{\mathbf{k}}} + 1)^{-1}, \tag{1.71}$$

where $\beta = 1/k_B T$. The quantity we are going to calculate is the probability $\langle b_{\mathbf{k}} \rangle$, in which the off-diagonal terms $\langle \gamma_{-\mathbf{k}\downarrow} \gamma_{\mathbf{k}\uparrow} \rangle$ and $\langle \gamma_{\mathbf{k}\uparrow}^\dagger \gamma_{-\mathbf{k}\downarrow}^\dagger \rangle$ are neglected because they do not contribute to the average,

$$\begin{aligned} \langle b_{\mathbf{k}} \rangle = \langle c_{-\mathbf{k}\downarrow} c_{\mathbf{k}\uparrow} \rangle &= u_{\mathbf{k}}^* v_{\mathbf{k}} \left(1 - \langle \gamma_{\mathbf{k}\uparrow}^\dagger \gamma_{\mathbf{k}\uparrow} \rangle - \langle \gamma_{-\mathbf{k}\downarrow}^\dagger \gamma_{-\mathbf{k}\downarrow} \rangle \right) \\ &= u_{\mathbf{k}}^* v_{\mathbf{k}} \left(1 - 2f(E_{\mathbf{k}}) \right). \end{aligned} \tag{1.72}$$

We then obtain a gap function $\Delta_{\mathbf{k}}(T)$ at finite temperature T by substituting $\langle b_{\mathbf{k}} \rangle$ for $b_{\mathbf{k}}$ in the self-consistent condition in Eq. (1.63),

$$\begin{aligned}\Delta_{\mathbf{k}} &= -\sum_{\mathbf{k}'} V_{\mathbf{k}\mathbf{k}'} u_{\mathbf{k}}^* v_{\mathbf{k}} \left[1 - 2f(E_{\mathbf{k}})\right] \\ &= -\sum_{\mathbf{k}'} V_{\mathbf{k}\mathbf{k}'} \frac{\Delta_{\mathbf{k}'}}{2E_{\mathbf{k}'}} \tanh\left(\frac{\beta E_{\mathbf{k}'}}{2}\right). \end{aligned} \tag{1.73}$$

Using the well-established BCS approximation where $V_{\mathbf{k}\mathbf{k}'} = -V$ with cut-off energy $\hbar\omega_D$ and $\Delta_{\mathbf{k}} = \Delta_{\mathbf{k}'} = \Delta$, the self-consistency condition becomes

$$\frac{1}{V} = \frac{1}{2} \sum_{\mathbf{k}} \frac{\tanh(\beta E_{\mathbf{k}}/2)}{E_{\mathbf{k}}}, \tag{1.74}$$

where $E_{\mathbf{k}} = (\xi_{\mathbf{k}}^2 + \Delta_{\mathbf{k}}^2)^{1/2}$. Equation (1.74) determines the temperature dependence of the energy gap $\Delta(T)$.

The critical temperature T_c is obtained as $\Delta(T) \to 0$, and correspondingly $E_{\mathbf{k}} \to |\xi_{\mathbf{k}}|$. Changing the summation for $\mathbf{k}$ to an integral for $\xi_{\mathbf{k}}$ using the density of states for a normal state at the Fermi surface $N(0)$, Eq. (1.74) becomes

$$\frac{1}{N(0)V} = \int_0^{\hbar\omega_D} \frac{1}{\xi_{\mathbf{k}}} \tanh\left(\frac{\xi_{\mathbf{k}}}{2k_B T_c}\right), \tag{1.75}$$

where the interval of integration is changed using the symmetry of odd functions. This integration can be solved by defining variable $x = \xi/2k_BT_c$ and integrating by parts,

$$\begin{aligned}\frac{1}{N(0)V} &= \int_0^{\hbar\omega_D/2k_BT_c} \frac{\tanh(x)}{x} dx \\ &= \Big[\ln(x)\tanh(x)\Big]_0^{\hbar\omega_D/2k_BT_c} - \int_0^{\hbar\omega_D/2k_BT_c} \frac{\ln(x)}{\cosh^2(x)} dx. \end{aligned} \tag{1.76}$$

As $k_BT_c \ll \hbar\omega_D$ for normal metals, $\tanh(x) \approx \tanh(\infty) = 1$ and $\int_0^\infty \ln(x)/\cosh^2(x)dx = \ln(\pi/4e^\gamma)$ with Euler's constant $\gamma = 0.577215\cdots$. We then finally obtain the relation for the critical temperature T_c as

$$\frac{1}{N(0)V} = \ln\left(\frac{2e^\gamma \hbar\omega_D}{\pi k_B T_c}\right). \tag{1.77}$$

1.2.3 Derivation of the GL equation

As revealed by Gor'kov [7], the GL theory is appropriate near the critical temperature T_c where the gap $|\Delta_{\mathbf{k}}|$ is sufficiently small. We here analyze the behavior of the gap equation Eq. (1.74) close to T_c, and try to obtain the GL equation for the order parameter ψ.

First, we consider the Taylor expansion for the gap function assuming sufficiently small $\Delta_{\mathbf{k}}$ as $T \to T_c$,

$$\begin{aligned}\Delta &= N(0)V\Delta \int_0^{\hbar\omega_D} f(E_{\mathbf{k}}) d\xi_{\mathbf{k}} \\ &\approx N(0)V\Delta \int_0^{\hbar\omega_D} d\xi_{\mathbf{k}} \left[f(\xi_{\mathbf{k}}) + (E_{\mathbf{k}} - \xi_{\mathbf{k}}) \frac{df(\xi_{\mathbf{k}})}{dE_{\mathbf{k}}}\Big|_{E_{\mathbf{k}}=\xi_{\mathbf{k}}} + \cdots\right] \\ &\approx N(0)V\Delta \int_0^{\hbar\omega_D} f(\xi_{\mathbf{k}}) d\xi_{\mathbf{k}} + N(0)V\Delta|\Delta|^2 \int_0^{\hbar\omega_D} \frac{d\xi_{\mathbf{k}}}{2\xi_{\mathbf{k}}} \frac{df(\xi_{\mathbf{k}})}{d\xi_{\mathbf{k}}}, \end{aligned} \tag{1.78}$$

where $f(\xi_{\mathbf{k}}) = \tanh(\beta\xi_{\mathbf{k}}/2)/E_{\mathbf{k}}$ and $E_{\mathbf{k}} - \xi_{\mathbf{k}} = \sqrt{\xi_{\mathbf{k}}^2 + |\Delta|^2} - \xi_{\mathbf{k}} \approx |\Delta|^2/2\xi_{\mathbf{k}}$. Taking the following integration formulas [8],

$$\int_0^\infty \frac{\tanh x}{x} dx \to \ln \frac{1.14\hbar\omega_D}{k_B T_c},$$
$$\int_0^\infty \frac{dx}{x}\frac{d}{dx}\left(\frac{\tanh x}{x}\right) \to -\frac{1}{\pi^2}\frac{7\zeta(3)}{8}, \tag{1.79}$$

where $\zeta(3)$ is the Riemann zeta-function we obtain the relation

$$\left(N(0)V \ln \frac{1.14\hbar\omega_D}{k_B T} - 1\right)\Delta - \frac{N(0)V}{2(\pi k_B T_c)^2}\frac{7\zeta(3)}{8}|\Delta|^2\Delta = 0, \tag{1.80}$$

which is equivalent to the GL equation in Eq. (1.8) except for the kinetic term.

Comparing Eqs. (1.8) and (1.80), we are able to estimate by setting $\psi = |\Delta|$, the coefficients in the GL free-energy functional in terms of the microscopic quantities:

$$\alpha(T) = \left(N(0)V \ln \frac{1.14\hbar\omega_D}{k_B T} - 1\right),$$
$$\beta = \frac{N(0)V}{2(\pi k_B T_c)^2}\frac{7\zeta(3)}{8}. \tag{1.81}$$

As mentioned earlier, $\alpha(T)$ is temperature dependent and β is always a positive value.

1.3 Unconventional Superconductors : Overview

Unconventional superconductors, generally identifying the category of superconducting materials for which the BCS theory is not applicable, have always been the source of intense debate in superconductivity research. To the best of my knowledge, the term unconventional superconductor was first applied to $CeCu_2Si_2$ discovered in 1979 with $T_c = 0.5$K [9]. Although it is believed that the superconductivity even for unconventional cases still originates with the formation of Cooper pairs, the conventional mechanism of phonon-mediated interaction as described in BCS theory appears not to be strong enough [10]. All other unconventional superconductors, for example UBe_{13}, UPt_3— known as a heavy Fermion system, Sr_2RuO_4— a spin-triplet superconductor, or the BEDT-TTF system—an organic superconductor, are systems providing exciting area of research that challenge and expand our understanding of superconductivity.

However, we will concentrate our interest on materials that have recorded high superconductivity critical temperatures. A major breakthrough was achieved with the discovery of the copper-oxide (cuprate) compounds, the first $La_{2-x}Ba_xCu_4O_y$ of which was found in 1986 by J. G. Bednorz and K. A. Müller [11]. For application purposes, the cuprate superconductors are still important materials because of their typically higher T_c than the boiling temperature of liquid nitrogen. In contrast, the highest critical temperature in metallic compounds was attained in magnesium diboride (MgB_2 at $T_c = 39$K) by Akimitsu's group [12]. Furthermore, the discoveries of iron-based superconductors by Horono's group in 2007 [13] were recent sensational news in the superconductivity research. Remarkably, the critical temperatures of the latter superconductors actually exceed theoretical predictions of $T_c \sim 30 - 40$K based on the BCS theory. We shall highlight these high-T_c superconductors in the following sections.[5]

[5]Timelines of superconductivity critical temperatures T_c's can be found in several websites, for example http://sakaki.issp.u-tokyo.ac.jp/user/kittaka/contents/others/tc-history.html.

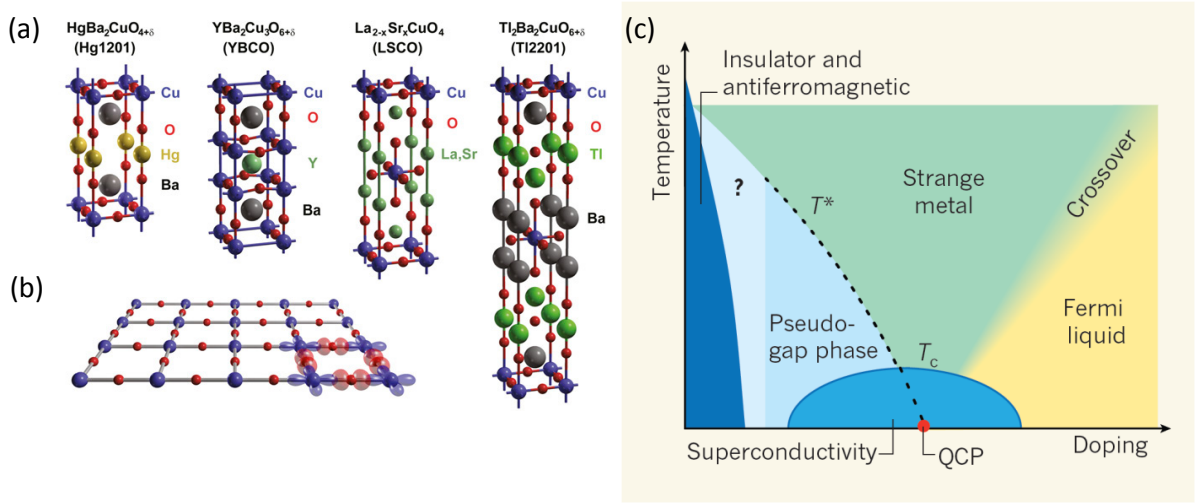

Figure 1.4: (a) Crystalline structures of cuprate superconductors. (b) CuO_2 layer illustrating electronic orbitals Cu $d_{x^2-y^2}$ and O p_σ. Reproduced with permission from Ref. [18]. (c) Typical phase diagram of a cuprate superconductor in terms of temperature and hole doping. Reprinted by permission from Macmillan Publishers Ltd: *Nature* [19], copyright 2010.

1.3.1 Copper-oxide superconductors

The first copper-oxide (cuprate) superconductor $La_{2-x}Ba_xCu_4O_y$ was actually a material unexpected as a superconductor with the remarkably high critical temperature of $T_c \sim 30$K [11]. Surprisingly, higher T_cs were soon to appear from substitution synthesis in $YBa_2Cu_3O_y$ with $T_c = 93$K, the first time the boiling point of liquid nitrogen 77K [14] was exceeded, and $Bi_2Sr_2Ca_2Cu_3O_y$ with $T_c = 107$K [15]. The highest recorded critical temperature among the cuprates (and for all superconductors) to date is achieved in $HgBaCa_2Cu_3O_y$ with $T_c = 135$K [16].

The crystalline structures of the cuprate superconductors (see Fig. 1.4(a)) are typically composed of two-dimensional superconducting planes of copper oxide CuO_2 (Fig. 1.4(b)), interposed by insulating blocking layers with other elements. A typical electrical phase diagram of a cuprate superconductor is shown in Fig. 1.4(c). In general, the undoped parent compounds are classified as Mott insulators, in which strong local Coulomb interactions cause the materials to become insulators instead of metals. Within this Mott-insulator state, antiferromagnetic (AFM) ordering of the copper ions is found within the CuO_2 planes. The AFM ordering appears only in a narrow region of the phase diagram and is quickly suppressed by hole doping; superconductivity emerges after the static AFM order has been suppressed [17].

That being the case, cuprate superconductors provide diverse playgrounds for magnetic characteristics, in other words, vortex states of our interest. Although magnetic properties in cuprate superconductors were readily studied after their discoveries, it was soon recognized that the conventional mean-field theory was no longer applicable and hence the H-T phase diagram becomes more complicated, because of the strong two-dimensionality and thermal fluctuations due to the high critical temperatures. The strength of two-dimensionality is often expressed by the anisotropy parameter $\gamma \equiv \xi_{ab}/\xi_c$ with ξ_{ab} and ξ_c for the superconductivity coherence lengths in ab-plane (CuO_2 planes) and c-axis (perpendicular to CuO_2 planes), respectively. Large anisotropy in cuprate superconductors is obviously originated from the layered crystalline structure of CuO_2. We postpone giving a detailed discussion here of vortex states and H-T diagrams in cuprate superconductors, leaving the topic for separate development in a later for chapter 6.

1.3.2 Magnesium diboride (MgB_2)

Superconductivity in MgB_2 confers the highest transition temperature $T_c = 39$K among metallic superconductors to date. The crystalline structure of MgB_2, as shown in Fig. 1.5(a), is an alternating structure of honeycombed boron layers and magnesium layers. From much intensive work performed immediately after discovery, MgB_2 has a simple superconductivity mechanism based on the electronphonon coupling. The most direct evidence for the phonon-mediated mechanism comes from the isotope effect [20], in which the T_c increased by about 1 K when ^{10}B was used instead of ^{11}B[6]. Other experiments such as photoemission spectroscopy, scanning tunneling microscopy, and neutron scattering measurements, also support the BCS mechanism [21, 22]. In terms of the origin of superconductivity, MgB_2 might be categorized to conventional superconductivity.

However, the remarkable property of MgB_2 is that there are two superconductivity gaps with $\Delta_\pi(0) = 2$meV and $\Delta_\sigma(0) = 7$meV, denoting σ and π bands of the boron electrons, as well established nowadays [21, 22]. Figure 1.5(b) shows the Fermi surface obtained by band structure calculations [23]. Green and blue cylinders (hole-like) come from the bonding $p_{x,y}$ bands, the blue tubular network (hole-like) from the bonding p_z bands, and the red (electron-like) tubular network from the antibonding p_z band. In Fig. 1.5(c), the values of the two gaps extracted from scanning tunneling spectroscopy are plotted as a function of temperature [24]. Both gaps follow typical temperature dependence predicted by the BCS theory as indicated by the lines, and disappear at the same T_c. According to the BCS theory, the material independent relation $2\Delta(0) = 3.54kT_c$ tells that the two energy gaps should then correspond to $T_{c,\pi} = 15$K and $T_{c,\sigma} = 45$K. However, the finite interband coupling results in a single $T_c = 40$K, which is unexpectedly lower than the $T_{c,\sigma}$. This consequence was pointed out by Mazin *et al* that the interband scattering between the σ and π bands is exceptionally small owing to the different symmetries in their charge-density distributions [25].

As we shall discuss in the next section, two-band superconductivity has been theoretically considered since from the 1950s in view of superconductivity in transition metals[26]. Although several candidate material had been suspected earlier as having multiband superconductivity, MgB_2 is the first to be undoubtedly identified as having two-band superconductivity. Also, it is noted that MgB_2 is a simple s-wave superconductor in which the gaps do not have nodes [27, 28], while other unconventional superconductors are known as d-wave for cuprate superconductors [29], or p-wave for Sr_2RuO_4 [30], for example. Furthermore, the multibandness in MgB_2 arise essentially new physical phenomena such as Leggett's collective mode [31].

1.3.3 Iron-based superconductors

In recent research on superconductors as well as on condensed matter physics, the discovery of iron-based (Fe-based) superconductors has been sensational, not only in yielding various high T_c compounds, but also in enriching theory with a new mechanism of superconductivity rich in multiband properties. After the first Fe-based superconductor discovered in 2006, LaFePO with $T_c = 4$K [32],[7] exploration for other Fe-based superconductors was sparked by the subsequent discovery in 2008 of $LaFeAs(O_{1-x}F_x)$ exhibiting a higher T_c of 26K [13]. Very soon after this, substitution of the lanthanoid element (Ln) was subsequently attempted and achieved a higher T_c, namely $NdFeAs(O_{1-x}F_x)$ with $T_c = 51$K [33] and $SmFeAs(O_{1-x}F_x)$ with $T_c = 55$K [34]. These materials are nowadays termed "1111"-type labeled for their atomic ratios. The crystalline structure of these 1111-type consists of an alternate stacking of FePn (Pn: pnictogen) and LnO layers. Each FePn layer is composed of a network of FePn_4 tetrahedra and each Fe layer forms a two-dimensional square sublattice.

Also readily discovered were other kinds of Fe-based superconductors, consisting of an alternate stacking of the same FePn and alkaline-earth layers but different structures, namely the "122"-type

[6] On the other hand, the isotope effect for Mg is much smaller, signaling that the boron atom vibrations are more important for superconductivity in MgB_2.

[7] The material, discovered during a systematic research on transparent semiconductors, is isostructural with p-type oxychalcogenide semiconductors LaCuSO.

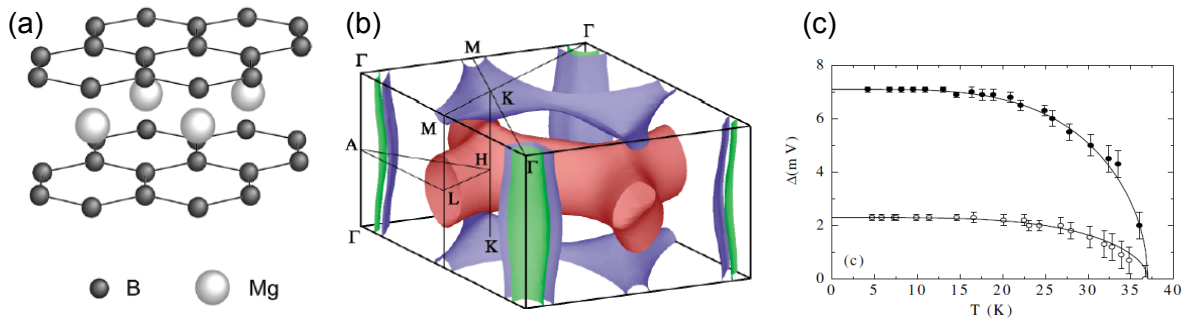

Figure 1.5: Characteristics of MgB_2: (a) Crystalline structure. Reprinted with permission from [22]. © IOP Publishing. Reproduced with permission of IOP Publishing. All rights reserved. (b) Fermi surface. Reprinted with permission from [23]. Copyright 2001 by the American Physical Society. (c) Temperature dependence of the gap values extracted from scanning tunneling spectroscopy (plots), and fitted by the BCS gap function $\Delta(T)$ (lines). Reprinted with permission from [24]. Copyright 2002 by the American Physical Society.

such as hole-doped $(Ae, \mathrm{K})\mathrm{Fe_2As_2}$ with the highest $T_c = 38$K [35, 36] or electron-doped $Ae(\mathrm{Fe,Co})_2\mathrm{As_2}$ (Ae: alkaline-earth elements) with the highest T_c of 23K. Among the all Fe-based superconductors, the 122-type should have been well-studied experimentally because single crystals were successfully synthesized earlier than other materials. Therefore, the Fermi surface of this material has been quickly established and understood.

AFeAs (A: alkaline elements), as "111"-type, was discovered with $T_c = 18$K, where each Ae element in the 122-type is substituted by two A elements [37]. $\beta - \mathrm{FeSe}$, as 11-type, consists of the simplest $\alpha - \mathrm{PbO}$ structure and a stacking of tetrahedron layers of $\mathrm{Fe}Ch_4$ (Ch: chalcogen) [38]. This material exhibits a lower critical temperature of $T_c \sim 8$K *as grown* than its highest one because of suppression of superconductivity owing to an excess of Fe [39]. Under high pressure or by certain annealing operations, FeSe exhibits a higher critical temperature of 37 K [40]. Other compounds consisting of perovskite-like blocking layers have also been synthesized [41, 42], such as $\mathrm{Sr_2VFeAsO_3}$ (21113-type) and $\mathrm{Sr_3Sc_2Fe_2As_2O_5}$ (32225-type). They also exhibit comparably high T_c of 37K and 45K, respectively. The crystalline structures of the Fe-based superconductors are summarized in Fig. 1.6. It is noted that quasi two-dimensional superconducting layers are also found in these materials, which resemble cuprate superconductors although anisotropy parameter γ in Fe-based superconductors is contrastively smaller.

The series of Fe-based superconductors were immediately recognized as a new class of unconventional superconductor because they produced a maximum T_c of 56 K which cannot be explained by a phonon-mediated electron-pairing interaction [46]. The parent phases of Fe-based superconductors are revealed as anti-ferromagnetic (AFM) order in a spin density wave (SDW) states [47]. Figure 1.7(a) shows a typical electronic phase diagram of Fe-based superconductors for both electron and hole doping cases [44]. These materials have presented a novel playground to investigate the magnetic interactions that lead to pairing in superconductivity and pairing symmetries. In Fig. 1.7(b), possible gap symmetries in Fe-based superconductors are illustrated, namely s_{++}-wave, $s_{\pm}$-wave, nodal $s_{\pm}$-wave, and $d_{x^2y^2}$-wave. Note that the s_{++} and $s_{\pm}$ states all have the same symmetry that either do not change sign under rotating the crystal axes by 90°, whereas the d-wave state changes sign under 90° rotation. Although the gap symmetries in Fe-based superconductors are not conclusive at this moment, it is emphasized that they depend sensitively on the doping ratio and the presence of both repulsive and attractive interband couplings. Of all the above-mentioned fundamental properties of Fe-based superconductors, the most relevance for this thesis is the presence of multiple gaps and interband couplings. From the Fermi surface of, for example, $\mathrm{Ba_{0.6}K_{0.4}Fe_2As_2}$ single crystals shown in Fig. 1.7(c), more than three bands contribute to its superconductivity [45]. Nearly isotropic

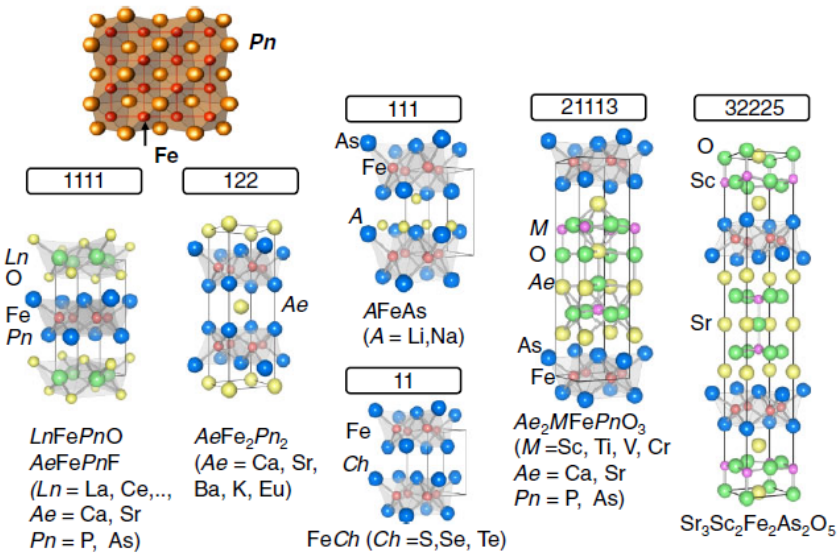

Figure 1.6: Crystalline structures of iron-based superconductors: "1111"-, "122"-, "111"-, "11"-, "21113"-, and "32225"-type compounds. The top-left schematic represents the top view of the common layer in iron-based superconductors, i.e., that of either FePn or FeCh (Pn: pnictogen, Ch: chalcogen). Reproduced with permission from Ref. [43]. Copyright 2012 The Japan Society of Applied Physics.

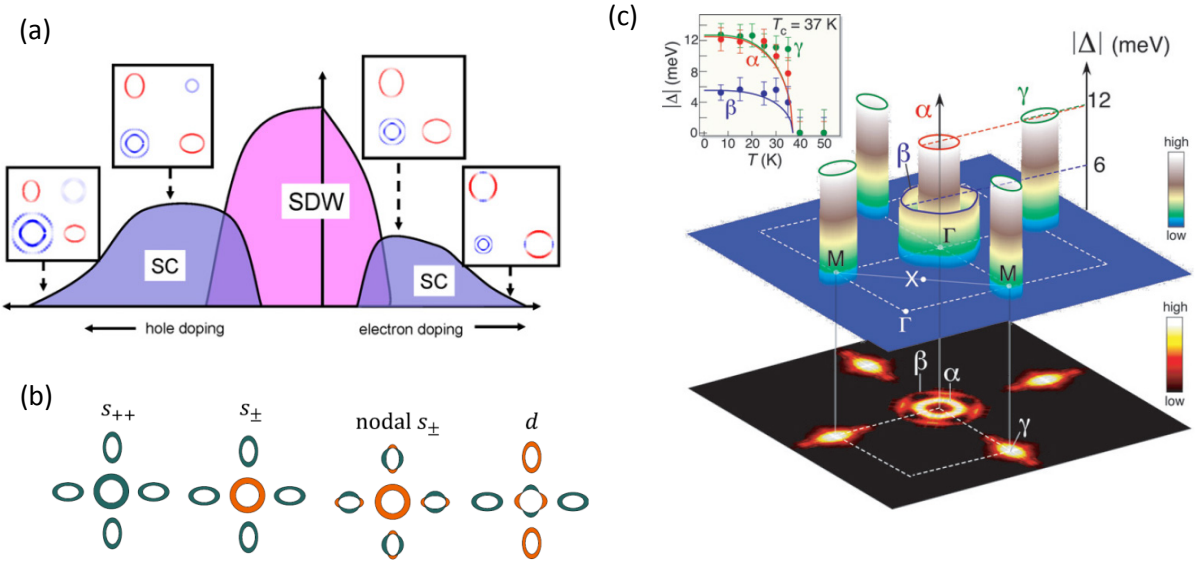

Figure 1.7: Characteristics of Fe-122 type superconductors: (a) Typical electronic phase diagram [44]. (b) Gap symmetries [44]. (c) Three-dimensional plot of the superconductivity gap size ($|\Delta|$) and Fermi surface in $Ba_{0.6}K_{0.4}Fe_2As_2$ [45].

superconductivity gaps open simultaneously at the bulk T_c on each Fermi surface sheet with electron and hole characteristics. Although the most natural interpretation for the pairing order parameter is an s-wave symmetry, we cannot rule out the possibility of nontrivial relative phases between the order parameters on the different Fermi surface sheets, which may bring totally different properties of superconductivity as an intrinsic consequence of multibandness to be discussed later.

1.4 Theories of Multiband Superconductivity

As we have previously stated, multiband superconductors have been widely recognized recently since the discovery of high-T_c superconductors such as MgB_2 and the Fe-based superconductors. However, it is worth remarking that the theoretical framework for multiband superconductivity was actually established soon after the publication of the BCS theory, and essentially different properties to single-band superconductors were uncovered that derive from the interaction between the different superconducting condensates. In this section, I first introduce these early theories for two-band superconductivity, and then review recent ones for multi-band superconductors highlighting their essential properties.[8]

1.4.1 Early theories of two-band superconductivity

The extension of the BCS theory to two-band superconductivity was undertaken first by H. Suhl *et al* [26] to describe superconductivity in transition elements. At that time, the work was apparently motivated by experimental facts resulting from the small isotope effect, which indicated that the conventional electron-phonon interaction mechanism was insufficient.

We first introduce the reduced BCS Hamiltonian for two-band superconductivity by analogy with the single-band BCS theory [26],

$$\begin{aligned}\mathcal{H} = &\sum_{\mathbf{k_1}\sigma} \xi_{\mathbf{k_1}} c^\dagger_{\mathbf{k_1}\sigma} c_{\mathbf{k_1}\sigma} + \sum_{\mathbf{k_2}\sigma} \xi_{\mathbf{k_2}} c^\dagger_{\mathbf{k_2}\sigma} c_{\mathbf{k_2}\sigma} \\ &- \sum_{\mathbf{k_1},\mathbf{k_1}'} V_{11}(\mathbf{k_1},\mathbf{k_1}') c^\dagger_{\mathbf{k_1}\uparrow} c^\dagger_{-\mathbf{k_1}\downarrow} c_{-\mathbf{k_1}'\downarrow} c_{\mathbf{k_1}'\uparrow} - \sum_{\mathbf{k_2},\mathbf{k_2}'} V_{22}(\mathbf{k_2},\mathbf{k_2}') c^\dagger_{\mathbf{k_2}\uparrow} c^\dagger_{-\mathbf{k_2}\downarrow} c_{-\mathbf{k_2}'\downarrow} c_{\mathbf{k_2}'\uparrow} \\ &- \sum_{\mathbf{k_1},\mathbf{k_1}'} V_{12}(\mathbf{k_1},\mathbf{k_2}') c^\dagger_{\mathbf{k_1}\uparrow} c^\dagger_{-\mathbf{k_1}\downarrow} c_{-\mathbf{k_2}'\downarrow} c_{\mathbf{k_2}'\uparrow} - \sum_{\mathbf{k_1},\mathbf{k_1}'} V_{12}(\mathbf{k_2},\mathbf{k_1}') c^\dagger_{\mathbf{k_2}\uparrow} c^\dagger_{-\mathbf{k_2}\downarrow} c_{-\mathbf{k_1}'\downarrow} c_{\mathbf{k_1}'\uparrow},\end{aligned} \tag{1.82}$$

where $\xi_{\mathbf{k_1}}$ and $\xi_{\mathbf{k_2}}$ are the kinetic energies in the first and second band, V_{11} and V_{22} are the electron-electron potentials for intra-band interactions, and V_{12} for inter-band interactions. As in the single-band BCS theory, we assume that the summations extend only over $\mathbf{k_1}$ and $\mathbf{k_2}$ values corresponding to energies within a distance $\pm\hbar\omega_D$ of the Fermi surface.

Following Bogoliubov's method for a single-band, we introduce operators γ by linear transformations indexed by j,

$$\begin{aligned} c_{\mathbf{k}_j\uparrow} &= u^*_{\mathbf{k}_j} \gamma_{\mathbf{k}_j\uparrow} + v_{\mathbf{k}_j} \gamma^\dagger_{-\mathbf{k}_j\downarrow}, \\ c^\dagger_{-\mathbf{k}_j\downarrow} &= -v^*_{\mathbf{k}_j} \gamma_{\mathbf{k}_j\uparrow} + u_{\mathbf{k}_j} \gamma^\dagger_{-\mathbf{k}_j\downarrow}. \end{aligned} \tag{1.83}$$

The gap equations for a finite temperature are obtained in a general form directly,

$$\Delta_{\mathbf{k}_j} = -\sum_{\mathbf{k}'_j} V_{jj}(\mathbf{k}_j,\mathbf{k}'_j) \frac{1-f_{\mathbf{k}_j}}{2\epsilon_{\mathbf{k}'_j}} \Delta_{\mathbf{k}'_j} - \sum_{\mathbf{k}'_l} V_{jl}(\mathbf{k}_j,\mathbf{k}'_l) \frac{1-f_{\mathbf{k}_l}}{2\epsilon_{\mathbf{k}'_l}} \Delta_{\mathbf{k}'_l}. \tag{1.84}$$

[8] In the following discussion, we use the term *multiband superconductor* when the number of bands N contributing to superconductivity is three or more ($N \geq 3$). For simplicity, we shall consider without loss of generality just three bands ($N = 3$).

We here assume that the intraband and interband pairing potentials are approximated in the conventional way,

$$\begin{aligned} V_{11}(\mathbf{k}_1, \mathbf{k}_1') &= -V_{11}, \\ V_{22}(\mathbf{k}_2, \mathbf{k}_2') &= -V_{22}, \\ V_{12}(\mathbf{k}_{1(2)}, \mathbf{k}_{2(1)}') &= -V_{12}. \end{aligned} \tag{1.85}$$

For simplicity, we assume an identical cut-off energy of $\hbar\omega_{\mathrm{D}}$ for both bands. Thus, Eq. (1.84) becomes

$$\Delta_j = N_j(0)V_{jj}\Delta_j \int_{-\hbar\omega_D}^{\hbar\omega_D} \frac{\tanh(\beta E_j/2)}{2E_j} d\xi_j + N_l(0)V_{jl}\Delta_l \int_{-\hbar\omega_D}^{\hbar\omega_D} \frac{\tanh(\beta E_l/2)}{2E_l} d\xi_l, \tag{1.86}$$

noting that the Δ_j are independent of $\mathbf{k}_j$ and depend only on the band index j.

As for a single band, the transition temperature is obtained in the limit $\Delta_j \to 0$. The condition for a nontrivial solution in Eq. (1.86) is that the determinant of the matrix of coefficients multiplying the vector Δ_j vanishes. That is,

$$\begin{vmatrix} N_1V_{11}x - 1 & N_2V_{12}x \\ N_2V_{12}x & N_2V_{22}x - 1 \end{vmatrix} = 0, \tag{1.87}$$

with definition $x = \ln(1.14\hbar\omega_D/k_BT_{\mathrm{c}})$. The relation for T_{c} is obtained by a quadratic equation in x,

$$\ln\left(\frac{1.14\hbar\omega_D}{k_BT_{\mathrm{c}}}\right) = \frac{N_1V_{11} + N_2V_{22} \pm [(N_1V_{11} + N_2V_{22})^2 + 4N_1N_2V_{12}^2]^{1/2}}{2N_1N_2(V_{11}V_{22} - V_{12}^2)}. \tag{1.88}$$

Enhancement of T_{c}

An insightful remark on the critical temperature was given by J. Kondo [48] in that overall critical temperature T_{c} increases with the presence of interband couplings.

First, we consider the limit $N_2 \to 0$. We thereby have $x \to 1/N_1V_{11}$, which recovers the simple BCS solution. When x is expanded in terms of N_2, we have

$$x = \frac{1}{N_1V_{11}}\left(1 - \frac{N_2V_{12}^2}{N_1V_{11}^2}\right). \tag{1.89}$$

A smaller value of x gives a higher transition temperature; indeed, Eq. (1.89) indicates that the overall T_{c} is always higher with multi-bands than with a single band.

Second, we consider the limit $V_{12} \to 0$, where we have either $x \to 1/N_1V_{11}$ or $x \to 1/N_2V_{22}$. Assuming $1/N_1V_{11} \leq 1/N_2V_{22}$, for example, x can also be expanded in terms of V_{12}, yielding

$$x = \frac{1}{N_1V_{11}}\left(1 - N_2\frac{V_{12}^2}{V_{11}}\frac{1}{N_1V_{11} - N_2V_{22}}\right). \tag{1.90}$$

Given $N_1V_{11} \geq N_2V_{22}$, Eq. (1.89) also indicates T_{c} increases.

We emphasize this result in our discussions based on the GL theory, which requires validating close to T_{c}.

Collective excitation

Another unique characteristic resulting from the presence of interband couplings was proposed by Leggett, namely the collective excitation (*Leggett mode*), where the relative phase between the bands oscillate and propagate in a superconductor [49]. Although we do not discuss this characteristic here regarding relevance to this thesis, the only remarking is the presence relative phases, which can first appear in multiband superconductors and arise essentially different property from the single-band case. The Leggett mode was experimentally observed, for instance, in a typical two-band superconductor MgB_2 [31].

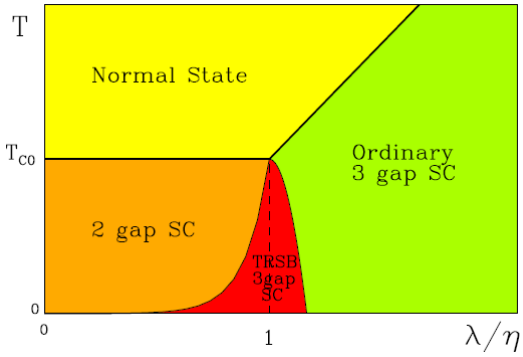

Figure 1.8: Phase diagram for superconductivity order parameters based on a three-band BCS model, including the TRSB state. Reprinted with permission from [52]. Copyright 2010 by the American Physical Society.

1.4.2 Time-reversal symmetry breaking (TRSB) in multiband superconductivity

The question "Does the *two-band* theory suffice as a general multiband theory?" naturally arises. The answer is "No" when we consider combination of multiple interband couplings required for a more complete discussion on multiband superconductors with more than three bands contributing. We shall review the further novel property of multiband superconductors.

In addition to the fact that superconductivity is understood as a spontaneous breaking of the gauge symmetry, the most intriguing aspect in multiband superconductivity is the possibility that other symmetry breaking mechanisms may arise. The idea that time-reversal symmetry breaking (TRSB) in a superconductor with multiple condensations was first proposed by D. F. Agterberg *et al.* in view of $CeCo_2$, $CeRu_2$, and LaB_6 which have been known as hosts of unconventional Fermi surface topologies [50, 51]. They assumed the pairing state was caused by the unusual BCS mechanism in substances of cubic and hexagonal symmetries where several Fermi surface pockets are centered at or around some high symmetry points of the Brillouin zone. Their conclusion was that the symmetry imposed on the multiple pocket positions could give rise to a multidimensional nontrivial superconducting order parameter. More specifically, time-reversal symmetry in the pairing state is broken, even with s-wave superconductivity.

The TRSB state was invoked recently by V. Stanev and Z. Tešanović inspired by the discovery that Fe-based superconductors also possess multiple superconducting condensates [52]. They considered a simple microscopic model with multiple bands connected via repulsive pair-scattering terms, and thereby found three possible superconducting order parameters, one of which breaks time-reversal symmetry to relax the frustration between intercomponent couplings, as shown in the phase diagram in Fig. 1.8. Later on, other pairings such as $s + id$ symmetry [53, 54] or $s + is$ symmetry [55] as well as junctions structures [56, 57] have also been discussed.

Based on the new concept of multiband TRSB superconductivity, various interesting properties have been intensively studied recently. The TRSB state in principle has two energy-degenerate chiral ground states analogous to the state in spin-triplet superconductivity. An initial analysis of the GL free energy revealed a chiral domain structure and associated fractional vortices [58, 59].

Collective excitations in the multiband TRSB superconductivity were also readily studied [60, 61, 62]. Generally, the mass of the Leggett mode is proportional to the strength of the interband couplings, and in multiband superconductivity, heavy mass makes excitation and detection difficult. However, a surprising feature was pointed out that the mass of the Leggett mode becomes small close to the TRSB transition and vanishes at the transition point, making it stable and detectable by Raman spectroscopy, for example, and would serve as a 'smoking gun' for the TRSB transition [63].

1.4.3 Multicomponent GL theory for TRSB superconductivity

As introduced in Sec. 1.1, the GL theory is a powerful approach to discuss magnetic properties or stability of states. Motivated by novelties in multiband TRSB superconductivity, this section is devoted to reviewing the principal framework used in this thesis. Termed the *multicomponent* GL theory, a stability condition and phenomenological properties of the TRSB state are discussed as performed by X. Hu and Z. Wang [64].[9]

The GL free-energy density functional for a multicomponent superconductor is derived from the BCS theory in the same way as with two components [65, 66],

$$f = \sum_{j=1,2,3} \left[\alpha_j |\psi_j|^2 + \frac{\beta_j}{2} |\psi_j|^4 + \frac{1}{2m_j} \left| (\frac{\hbar}{i}\nabla - \frac{2e}{c}\mathbf{A})\psi_j \right|^2 \right] - \sum_{j<k} \gamma_{jk}(\psi_j \psi_k^* + \text{c.c.}) + \frac{1}{8\pi}(\nabla \times \mathbf{A})^2, \tag{1.91}$$

where summations run over the number of components. In the following discussion, a three-component system is considered for simplicity and without loss of generality. The coefficients are conventionally defined as

$$\alpha_j(T) = \alpha_j(0)\left(\frac{T}{T_{cj}} - 1\right) \qquad \alpha_j(0) > 0 \tag{1.92}$$

where T_{cj}'s are the critical temperatures for individual components without the couplings, and β_j's are positive constants. γ_{jk}'s stand for the intercomponent couplings and can be either positive or negative, corresponding to attractive or repulsive coupling, respectively.

As illustrated in Fig. 1.9, attention is paid to the combination of intercomponent coupling parameters. If $\gamma_{12}\gamma_{23}\gamma_{13} > 0$ holds, as for the *time-reversal symmetry reserved* (TRSR) state, the system behaves as a single-band superconductivity.[10] In contrast, $\gamma_{12}\gamma_{23}\gamma_{13} < 0$ represents a TRSB state on which we now focus. Hereafter, we treat explicitly a system where all γ_{jk}'s are negative, noting that a simple gauge transformation in Eq. (1.91) links it to the other possible instances.

The multicomponent GL equations are derived from the free-energy density functional in Eq. (1.91) by a variational method,

$$\alpha_j \psi_j + \beta_j |\psi_j|^2 \psi_j + \frac{1}{2m_j}\left(\frac{\hbar}{i} - \frac{2e}{c}\mathbf{A}\right)^2 \psi_j - \gamma_{jl}\psi_l - \gamma_{jn}\psi_n = 0, \tag{1.93}$$

and for supercurrents,

$$\frac{c}{4\pi}\nabla \times \nabla \times \mathbf{A} = \sum_j \frac{2e\hbar}{m_j}|\psi_j|^2 \left(\nabla\phi_j - \frac{2\pi}{\Phi_0}\mathbf{A}\right), \tag{1.94}$$

where j, l, n are indices of the components and ϕ_j the phase of the order parameter.

Stability condition of the TRSB state

Around the critical point, which itself is to be determined, the order parameters in the bulk follow the linearized equations of Eq. (1.93),

$$\begin{bmatrix} \alpha_1 & -\gamma_{12} & -\gamma_{13} \\ -\gamma_{12} & \alpha_2 & -\gamma_{23} \\ -\gamma_{13} & -\gamma_{23} & \alpha_3 \end{bmatrix} \begin{bmatrix} \psi_1 \\ \psi_2 \\ \psi_3 \end{bmatrix} = \mathbf{Q} \cdot \mathbf{\Psi} = \mathbf{0}, \tag{1.95}$$

with coupling matrix $\mathbf{Q}$. The critical temperature T_c in composite superconductivity is given by the highest temperature where the determinant of $\mathbf{Q}$ becomes zero,

$$\alpha_1\alpha_2\alpha_3 - 2\gamma_{12}\gamma_{23}\gamma_{13} - \alpha_1\gamma_{23}^2 - \alpha_2\gamma_{13}^2 - \alpha_3\gamma_{12}^2 = 0. \tag{1.96}$$

[9] This section is reprinted excerpt with permission from [64]. Copyright 2012 by the American Physical Society.
[10] The GL theory for TRSR superconductivity is discussed in Appendix B.

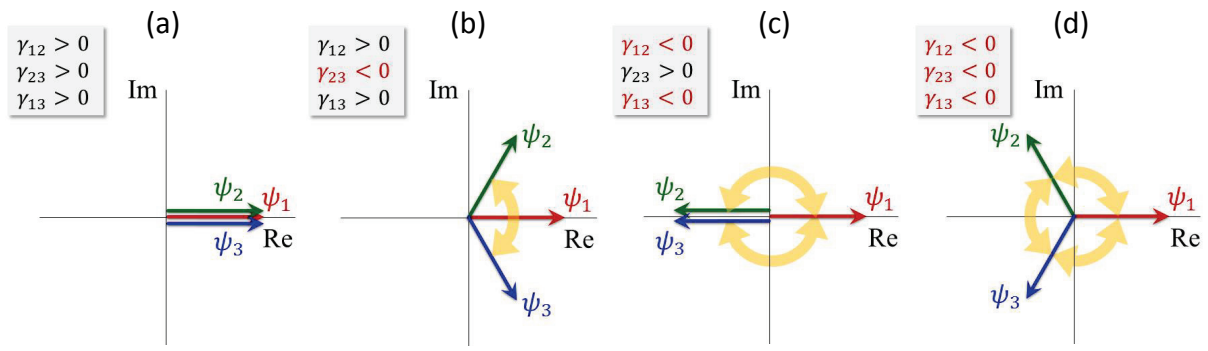

Figure 1.9: Schematics of the phase configuration for the three-component system. The cases (b) and (d) represent the TRSB state with nontrivial intercomponent phases $\phi_{jk} \equiv \phi_k - \phi_j \neq 0, \pi$, whereas the cases (a) and (c) the TRSR state with trivial values $\phi_{jk} = 0, \pi$.

According to Sylvester's criterion[11] [67], one has $\alpha_j > 0$ and $\alpha_j \alpha_k - \gamma_{jk}^2 \geq 0$ at T_c. This is appropriate because the critical temperature in composite superconductivity is above those for each single component, and not below those in the two-component superconductivity, despite negative couplings (see Sec. 1.4). If Eq. (1.96) has a single root at $T = T_c$, or equivalently, if there are two independent vectors in the coupling matrix $\mathbf{Q}$, the ratios between the order parameters given by Cramer's rules for the components of the matrix $\mathbf{Q}$ should be real. The order parameters for three-component superconductivity can then be taken as real numbers, apart from a common phase factor, as for single- and two-component superconductivity. Equation (1.96) has a doubly degenerate root, or equivalently, there is only one independent vector in $\mathbf{Q}$, when

$$\alpha_1 \alpha_2 - \gamma_{12}^2 = \alpha_1 \alpha_3 - \gamma_{13}^2 = \alpha_2 \alpha_3 - \gamma_{23}^2 = 0 \tag{1.97}$$

at T_c, because

$$\sum_{j<k} \epsilon_j \epsilon_k = \sum_{j<k} (\alpha_j \alpha_k - \gamma_{jk}^2) \tag{1.98}$$

with ϵ_j the eigenvalues of $\mathbf{Q}$ and each term in the second summation nonnegative. The single independent vector in the coupling matrix $\mathbf{Q}$ leaves room for complex order parameters in Eq. (1.96) despite the fact that all parameters in $\mathbf{Q}$ are real. It is clear that this situation occurs in a system with three or more components, and hence has no counterpart in single- or two-component superconductivity. Equation (1.97) is the first condition for a TRSB state specified by complex order parameters. It is easy to see that relations in Eq. (1.97), as well as the associated ones $\alpha_j \gamma_{kl} + \gamma_{jk} \gamma_{kl} = 0$, correspond to single zeros, because $\gamma_{jk} \neq 0$. One finds,

$$\frac{\alpha_k \alpha_l - \gamma_{kl}^2}{\alpha_j \alpha_l - \gamma_{jl}^2} = \frac{\alpha_k + \gamma_{jk} \gamma_{kl} / \gamma_{jl}}{\alpha_j + \gamma_{jk} \gamma_{jl} / \gamma_{kl}} = \left(\frac{\gamma_{kl}}{\gamma_{jl}} \right)^2 \tag{1.99}$$

at $T = T_c$.

The order parameters in the bulk for $T \lesssim T_c$ are given by

$$\begin{bmatrix} \alpha_1 + \beta_1 \psi_1^2 & -\gamma_{12} & -\gamma_{13} \\ -\gamma_{12} & \alpha_2 + \beta_2 \psi_2^2 & -\gamma_{23} \\ -\gamma_{13} & -\gamma_{23} & \alpha_3 + \beta_3 \psi_3^2 \end{bmatrix} \begin{bmatrix} \psi_1 \\ \psi_2 \\ \psi_3 \end{bmatrix} = \mathbf{Q}' \cdot \mathbf{\Psi} = \begin{bmatrix} 0 \\ 0 \\ 0 \end{bmatrix}. \tag{1.100}$$

Setting ψ_1 real, which is always possible, the imaginary parts of ψ_2 and ψ_3 obey

$$\begin{bmatrix} \alpha_2 + \beta_2 \psi_2^2 & -\gamma_{23} \\ -\gamma_{23} & \alpha_3 + \beta_3 \psi_3^2 \end{bmatrix} \begin{bmatrix} \mathrm{Im}(\psi_2) \\ \mathrm{Im}(\psi_3) \end{bmatrix} = \begin{bmatrix} 0 \\ 0 \end{bmatrix}. \tag{1.101}$$

[11] Sylvesters criterion is a necessary and sufficient criterion to determine whether a Hermitian matrix $\mathbf{M}$ is positive-definite, namely all the principal minors of $\mathbf{M}$ should be nonnegative.

Therefore, for complex order parameters, one has $\alpha_3\beta_2|\psi_2|^2 + \alpha_2\beta_3|\psi_3|^2 \simeq -\alpha_2\alpha_3 + \gamma_{23}^2$ up to $O(t)$ with $t \equiv (T_c - T)/T_c$. In the same way, one obtains two other similar relations, and thus

$$\begin{bmatrix} 0 & \alpha_3\beta_2 & \alpha_2\beta_3 \\ \alpha_3\beta_1 & 0 & \alpha_1\beta_3 \\ \alpha_2\beta_1 & \alpha_1\beta_2 & 0 \end{bmatrix} \begin{bmatrix} |\psi_1|^2 \\ |\psi_2|^2 \\ |\psi_3|^2 \end{bmatrix} = \mathbf{A}' \cdot \mathbf{\Psi} = \begin{bmatrix} -\alpha_2\alpha_3 + \gamma_{23}^2 \\ -\alpha_1\alpha_3 + \gamma_{13}^2 \\ -\alpha_1\alpha_2 + \gamma_{12}^2 \end{bmatrix}. \tag{1.102}$$

We then arrive at the following temperature dependence of the order parameters up to $O(t)$,

$$|\psi_j|^2 \simeq -\frac{\alpha_j + \gamma_{jk}\gamma_{kl}/\gamma_{kl}}{\beta_j}. \tag{1.103}$$

The relation $\alpha_1 - \gamma_{12}\psi_2/\psi_1 - \gamma_{13}\psi_3/\psi_1 = 0$ from Eq. (1.95) is then equivalent to

$$\frac{\alpha_1}{\sqrt{\beta_1}} + \frac{\alpha_2}{\sqrt{\beta_2}} e^{i\phi_{21}} + \frac{\alpha_3}{\sqrt{\beta_3}} e^{i\phi_{31}} = 0, \tag{1.104}$$

for $T \lesssim T_c$, where $\phi_{21}(\phi_{31})$ is the phase difference between $\psi_2(\psi_3)$ and ψ_1. Clearly, the condition for a stable state of complex order parameters is equivalent to that of a triangle formed by three segments:

$$\frac{\alpha_j}{\sqrt{\beta_j}} + \frac{\alpha_k}{\sqrt{\beta_k}} > \frac{\alpha_l}{\sqrt{\beta_l}}, \tag{1.105}$$

for $T \lesssim T_c$ with $j \neq k \neq l$. The above result can be derived from any of the three relations in Eq. (1.95), as there is only one independent vector there. A phase diagram for the equilibrium state for a three-component superconductor with frustrated intercomponent couplings is displayed in Fig. 1.10(a).

The relations (1.97) and (1.105) constitute the complete set of conditions for the stability of a state with complex order parameters, i.e., TRSB superconductivity. The special case with isotropic parameters discussed previously satisfies these conditions. A phase transition at a lower temperature between the TRSB and TRSR states is possible for appropriate temperature-dependent parameters (see Fig. 1.10(a)), where interesting physics is expected.

Properties of multicomponent TRSB superconductivity

Based on the multicomponent GL theory in the previous section, phenomenological properties in the TRSB state were also investigated in Ref. [64].

To analyze the coherence length, we concentrate on instances where the order parameters have an isotropic bulk value and equal effective masses in two of the three components. We give an infinitesimal distortion to one of the components and estimate the propagation of this distortion in the system. Unique to the present TRSB state, the distortion propagates in a manner different from that in isotropic components. Therefore, an essentially anisotropic system should be treated, where $\alpha_1 = \alpha_2 = \alpha_3 \equiv \alpha$, $\beta_1 = \beta_2 = \beta_3 \equiv \beta$ and $\gamma_{12} = \gamma_{23} = \gamma_{13} \equiv \gamma$ yielding an amplitude for the order parameter in the bulk of $|\psi_j| = \sqrt{-(\alpha+\gamma)/\beta} \equiv \psi_0$ with the critical point at $\alpha + \gamma = 0$ and phase differences of $\phi_{21} = -\phi_{31} = 2\pi/3$.

As displayed in Fig. 1.10(c), an infinitesimal stretch in the component with a possibly different effective mass (m_1) $\psi_1 = (1+\delta_1)\psi_0$ at $x = 0$ causes distortions in the other two components with the same effective mass (m_{23}) $\psi_2 = (1+\delta_2)\psi_0 \exp[i(2\pi/3 + \delta_3)]$ and $\psi_3 = (1+\delta_2)\psi_0 \exp[i(2\pi/3 + \delta_3)]$. All the distortions decay exponentially into the bulk ($x \to \infty$) with a length scale of the order of the coherence length. In the present TRSB state, the distortions in the amplitudes and phases generally are dependent one with the other, because the phase differences are determined by the amplitudes (see Eq. (1.104)); this is in contrast with superconductivity without TRSB.

The GL equation for ψ_1 with spatial variation

$$\alpha_1\psi_1 + \beta\psi_0^2\psi_1 - \gamma(\psi_2 + \psi_3) = \frac{\hbar^2}{2m_1}\frac{\partial^2\psi_1}{\partial x^2} \tag{1.106}$$

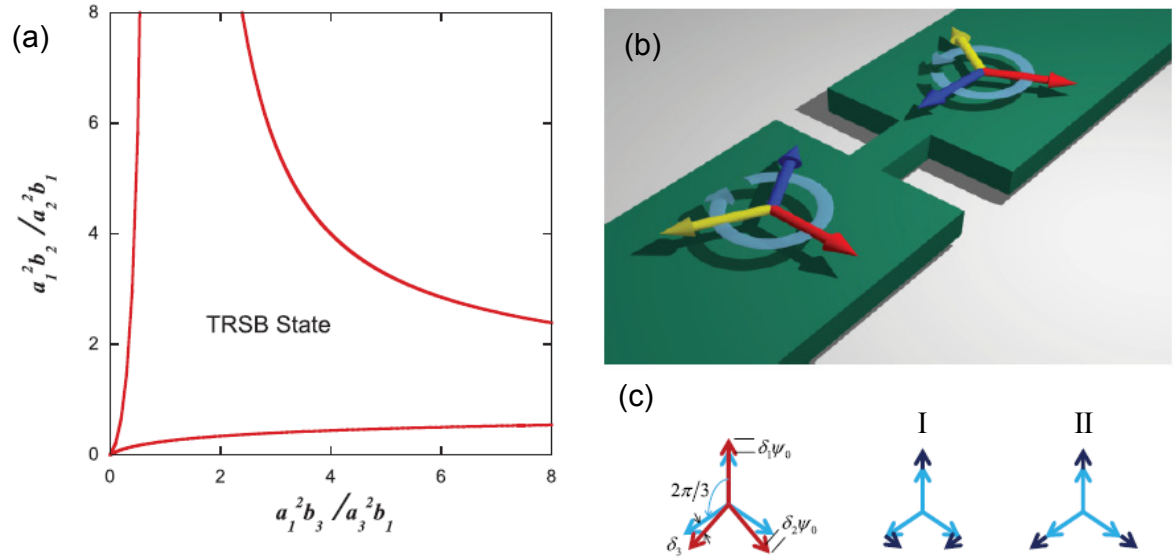

Figure 1.10: (a) Phase diagram for a three-component superconductor with stable TRSB superconductivity at the central part and TRSR superconductivity at the corners. (b) Two chiral TRSB states with intrinsically complex order parameters of a three-component superconductor in a Josephson junction with a constriction structure. (c) Definitions of distortions in complex order parameters with equal bulk amplitude (left), and two characteristic distortions of mode-I and mode-II (right). Reprinted with permission from [64]. Copyright 2012 by the American Physical Society.

is reduced to

$$(\alpha + 3\beta\psi_0^2)\delta_1 + \gamma\delta_2 + \sqrt{3}\gamma\delta_3 = \frac{\hbar^2}{2m_1}\frac{\partial^2\delta_1}{\partial x^2}, \tag{1.107}$$

where only the lowest-order infinitesimal distortions are considered. Similarly, one has the following two equations for the other two components:

$$\frac{\gamma}{2}\delta_1 + \left(\alpha + 3\beta\psi_0^2 + \frac{\gamma}{2}\right)\delta_2 - \frac{\sqrt{3}\gamma}{2}\delta_3 = \frac{\hbar^2}{2m_{23}}\frac{\partial^2\delta_2}{\partial x^2}, \tag{1.108}$$

$$\frac{\sqrt{3}\gamma}{2}\delta_1 - \frac{\sqrt{3}\gamma}{2}\delta_2 + \left(\alpha + \beta\psi_0^2 - \frac{\gamma}{2}\right)\delta_3 = \frac{\hbar^2}{2m_{23}}\frac{\partial^2\delta_3}{\partial x^2}. \tag{1.109}$$

$$\tag{1.110}$$

For exponentially decaying distortions $\delta_j = A_j \exp(-\sqrt{2}x/\xi)$, one has

$$\begin{bmatrix} -2\alpha - 3\gamma - \frac{\hbar^2\xi^{-2}}{m_1} & \gamma & \sqrt{3}\gamma \\ \gamma/2 & -2\alpha - 5\gamma/2 - \frac{\hbar^2\xi^{-2}}{m_{23}} & -\sqrt{3}\gamma/2 \\ \sqrt{3}\gamma/2 & -\sqrt{3}\gamma/2 & -3\gamma/2 - \frac{\hbar^2\xi^{-2}}{m_{23}} \end{bmatrix} \begin{bmatrix} A_1 \\ A_2 \\ A_3 \end{bmatrix} = \begin{bmatrix} 0 \\ 0 \\ 0 \end{bmatrix}, \tag{1.111}$$

where the bulk order parameter $\psi_0 = \sqrt{-(\alpha+\gamma)/\beta}$ has been included. The coherence length ξ of the system is determined by the zero determinant of the above coupled linear equations. Interestingly, associated with the doubly degenerate roots at T_c in the present TRSB state, two divergent ξ's exist as solutions to the above equation:

$$\frac{\hbar^2\xi^{-2}}{-(\alpha+\gamma)m_1} = \frac{3m_{23}}{2m_1}\frac{2 + \frac{m_{23}}{m_1} \pm \sqrt{(\frac{m_{23}}{m_1})^2 - \frac{4m_{23}}{3m_1} + \frac{4}{3}}}{1 + \frac{2m_{23}}{m_1}}, \tag{1.112}$$

up to $O(t)$.

The ratios between the A_j's (the distortion amplitudes) are given by

$$\frac{A_2}{A_1} = -\frac{R}{2(3-2R)},$$
$$\frac{A_3}{A_1} = -\frac{\sqrt{3}(2-R)}{2(3-2R)}, \tag{1.113}$$

where R is defined by the right-hand side of Eq. (1.112). For $m_1 = m_{23}$, one finds that the solution with minus sign in Eq. (1.112) is specified by $R = 1$, and $A_2/A_1 = -1/2$ and $A_3/A_1 = \sqrt{3}/2$ (mode-I as shown in Fig. 1.10(c)), whereas the solution with plus sign in Eq. (1.112) is specified by $R = 2$, and $A_2/A_1 = 1$ and $A_3/A_1 = 0$ (mode-II as shown in Fig. 1.10(c)). Whereas mode-II is conventionally associated with just variations in the amplitudes of the order parameters, known as superconductivity without TRSB, mode-I is novel in which these variations are coupled and is specific to the TRSB state.

Other quantities for the present superconductivity are obtained straightforwardly. The London penetration depth λ is obtained from the multicomponent GL equations for supercurrent Eq. (1.94),

$$\lambda^{-2} = \frac{4\pi(2e)^2}{c^2}\left(-1 - \frac{\gamma_{12}\gamma_{13}}{\alpha_1\gamma_{23}}\right)\sum_j \frac{\alpha_j}{\beta_j m_j}. \tag{1.114}$$

The thermodynamic critical field $H_{\rm tc}$ is derived using the form of the order parameters in Eq. (1.103),

$$\frac{H_{\rm tc}^2}{8\pi} = \frac{1}{2}\left(1 + \frac{\gamma_{12}\gamma_{13}}{\alpha_1\gamma_{23}}\right)^2 \sum_j \frac{\alpha_j^2}{\beta_j}. \tag{1.115}$$

Additionally, the nucleation field H_n at which superconductivity appears upon lowering the magnetic field is found to be

$$H_{\rm n} = \frac{\Phi_0}{2\pi}\frac{-1-\gamma_{12}\gamma_{13}/\alpha_1\gamma_{23}}{\sum_{j<k} L_j^2 L_k^2}\left(\sum_j L_j^2 + \sqrt{\sum_j L_j^4 - \sum_{j<k} L_j^2 L_k^2}\right), \tag{1.116}$$

with $L_j^2 = \hbar^2/2\alpha_j m_j$.

As introduced in Sec. 1.1, superconductors are classified as either type-I or type-II by the condition $H_{\rm n} < H_{\rm tc}$ or $H_{\rm n} > H_{\rm tc}$, respectively. In single-component superconductors, or in general superconductors with TRSR, the ratio between the these two fields is given by $\sqrt{2}\lambda/\xi$. Therefore, the GL parameter $\kappa \equiv \lambda/\xi = 1/\sqrt{2}$ separates type-I and type-II superconductors. In a superconductor with TRSB, clearly $H_{\rm tc} \neq \Phi_0/2\sqrt{2}\pi\xi\lambda$ and $H_{\rm n} \neq \Phi_0/2\pi\xi^2$ based on Eqs. (1.115) and (1.116). This conclusion implies that the GL parameter κ is insufficient in classifying the present TRSB superconductivity, and magnetic properties such as vortex states remained unclear.

1.5 Summary: Vortex Matter in Unconventional Superconductors

In this introductory chapter of this thesis, I have highlighted;

- Principal magnetic properties and vortex states in conventional superconductors;
- Multibandness and dimensionality in unconventional superconductors; and
- Theoretical framework for multiband (or multicomponent) superconductors.

Table 1.1: Superconductivity characteristics and electronic structures of cuprates, MgB_2, and Fe-based superconductors [43].

	Cuprates	MgB_2	Fe-based
Relevant elements to superconductivity	Cu $3d_{x^2-y^2}$–O $2p_\alpha$	B $2p_\sigma$, $2p_\pi$	Fe $3d$
Number of condensates (N)	$N = 1$	$N = 2$	$N \geq 3$
Pairing mechanism	Spin fluctuation	Phonon	Spin/Orbital fluctuation
Pairing symmetry	$d_{x^2-y^2}$	s	$s_\pm/s_{++}$
Electronic state of parent material	AFM Mott insulator	Paramagnetic metal	AFM metal (semi-metal)
Anisotropy parameter γ	$10^0 \sim 10^{2-3}$	$1 \sim 5$	$1 \sim 10$

To begin, I introduced the two fundamental theories, i.e. GL and BCS theories. Based on the GL theory, I have focused on the magnetics properties in superconductors, and especially on the analytical derivation of the vortex state, and how it plays an important role in the magnetic properties. I have also reviewed the BCS theory to discuss the temperature dependence of the gap function, and how the GL formalism is derived.

Next, I reviewed the current understanding of relevant unconventional superconductors, namely cuprates, MgB_2, and Fe-based superconductors, which are noted for typically high T_c. Table 1.1 summarizes the features of the electronic structures and physical properties of them. For the cuprate superconductors, superconductivity arises when either hole or electron carriers are doped in the CuO_2 plane. The Fermi level exists in the Cu $3d_{x^2-y^2}$-O $2p_\alpha$ degenerate band, and thus only a single electronic band is involved in superconductivity. In contrast, Fe-based superconductors have been found to have five Fe $3d$ bands crossing the Fermi level resulting in multiband superconductivity according to band calculations and experimental studies. MgB_2 was introduced as a well-established two-band superconductor in which $2p_\sigma$ and $2p_\pi$ bands in boron are involved in the Fermi level.

Finally, I reviewed early and recent theories for multiband superconductors, and emphasized that a straightforward extension performed in the two-band case is not appropriate for the multiband case when the interband couplings are frustrated, namely time-reversal symmetry breaking (TRSB). The multiband TRSB superconductor is essentially novel where both gauge and time-reversal symmetries are spontaneously broken. Based on such exotic superconductors, intensive studies have been undertaken within both the BCS and GL theories, and novel characteristics in the multiband TRSB superconductor have been investigated. However, magnetic properties such as vortex states have not been well studied owing to the complexity of the order parameters, although the multicomponent GL theory indeed indicates that TRSB superconductivity cannot be classified as either type-I or type-II by the conventional GL parameter κ.

I shall thereby discuss the following issues as objectives of this thesis:

1. To characterize vortex structure in a multiband TRSB superconductor
2. To explore novel magnetic properties and classification of multiband TRSB superconductors
3. To suggest experimental methods for identifying a TRSB state

For these objectives, I employ numerical approaches based on the multicomponent GL theory. In Chapter 2, the temperature dependence of the TRSB stability condition is discussed based on the BCS gap functions; this is useful for constructing H-T phase diagrams. Also, I explain principal parameterization used in numerical simulations. In Chapter 3, vortex structure in the multiband TRSB superconductor is discussed to clear item 1 above. In Chapter 4, novel vortex states and H-T phase diagrams of multiband TRSB superconductivitor are discussed in response to items 2 and 3. In

Chapter 5, typical magnetization curves (M-H curves) are modeled which can be easily approached experimentally in fulfilling item 3 as well.

Moreover, dimensionality is also an interesting characteristic in the recently discovered unconventional superconductors, which commonly consist of layered structure. The strength of the dimensionality is typically characterized by the anisotropy parameter $\gamma \equiv \xi_{ab}/\xi_c$, where $\xi_c(\xi_{ab})$ is the coherence length perpendicular (parallel) to the superconductivity planes. In the (quasi) two-dimensional superconductors, the conventional scheme describing vortices in an isotropic systems is no longer valid because the vortex structure is strongly related to the coherence length.

A typical but unambiguous example is the cuprate superconductor, which exhibits significantly large anisotropy parameter of order $\gamma = 10 \sim 100$. Indeed, the vortex states in the cuprate superconductors have been investigated for some time and various vortex states and phase diagrams are now well established. Whereas all these studies were performed for vortices perpendicular fields to the planes ($H \perp ab$), vortex states in a parallel field ($H \parallel ab$) are in contrast unclear although theoretical studies indicate novel vortex states.

In this thesis, such vortex states in structurally layered systems, i.e. Josephson vortex (JV), are discussed motivated by the experimental results observing the dynamics of JVs. I then purpose to identify novel JV states by means of a comparative study between numerical simulations and experimental approaches.

Chapter 2

Temperature Dependence of the TRSB State

2.1 Stability Condition of the TRSB State with Gap Functions $\Delta_j(T)$

A stability condition for the TRSB state was discussed in Ref. [64] based on the multicomponent GL theory, which is valid near the critical temperature T_c. In this section, We employ the temperature-dependent BCS gap functions to explore the stability condition of the TRSB state for the finite-temperature regime which is useful when constructing H-T phase diagrams.

The BCS Hamiltonian for single-band superconductivity is extended straightforwardly to the multiband case [26],

$$\begin{aligned}\mathcal{H} = \sum_{j\leq N}\Big[\sum_{\mathbf{k}_j,\sigma}\xi_{\mathbf{k}_j}c^{\dagger}_{\mathbf{k}_j\sigma}c_{\mathbf{k}_j\sigma} - \sum_{\mathbf{k}_j,\mathbf{k}'_j}V_{jj}c^{\dagger}_{\mathbf{k}_j\uparrow}c^{\dagger}_{-\mathbf{k}_j\downarrow}c_{-\mathbf{k}'_j\downarrow}c_{\mathbf{k}'_j\uparrow}\Big] \\ - \sum_{j\neq l,j,l\leq N}\sum_{\mathbf{k}_j,\mathbf{k}_l}V_{jl}c^{\dagger}_{\mathbf{k}_j\uparrow}c^{\dagger}_{-\mathbf{k}_j\downarrow}c_{-\mathbf{k}'_l\downarrow}c_{\mathbf{k}'_l\uparrow},\end{aligned} \tag{2.1}$$

with $N \geq 3$. The second and third terms correspond to the intra- and inter-band couplings, respectively. The coupled self-consistent BCS gap equations for multiband superconductors are derived straightforwardly using a mean-field approach [6],

$$\begin{aligned}\Delta_j =& V_{jj}N_j(0)\Delta_j\int_{-\hbar\omega_D}^{\hbar\omega_D}\frac{d\xi_j}{2E_j}\tanh\Big(\frac{E_j}{2k_BT}\Big) \\ &+\sum_{j\neq l}V_{jl}N_l\Delta_l\int_{-\hbar\omega_D}^{\hbar\omega_D}\frac{d\xi_l}{2E_l}\tanh\Big(\frac{E_l}{2k_BT}\Big),\end{aligned} \tag{2.2}$$

with $\Delta_j = -\sum_{\mathbf{k}_j}V_{jj}\langle c_{-\mathbf{k}_j\downarrow}c_{\mathbf{k}_j\uparrow}\rangle - \sum_{j\neq l}\sum_{\mathbf{k}_l}V_{jl}\langle c_{-\mathbf{k}_l\downarrow}c_{\mathbf{k}_l\uparrow}\rangle$ and $E_j = \sqrt{\xi_j^2 + |\Delta_j|^2}$; here, an identical cut-off energy $\hbar\omega_D$ is taken in all bands for simplicity. The coupled BCS equations for the three-band case are rewritten,

$$\begin{bmatrix} g_{11}-f_1(E_1,T) & g_{12} & g_{13} \\ g_{12} & g_{22}-f_2(E_2,T) & g_{23} \\ g_{13} & g_{23} & g_{33}-f_3(E_3,T)\end{bmatrix}\begin{bmatrix}\Delta_1\\ \Delta_2\\ \Delta_3\end{bmatrix} = \begin{bmatrix}0\\0\\0\end{bmatrix}, \tag{2.3}$$

where

$$f_j(E_j,T) = N_j(0)\int_{-\hbar\omega_D}^{\hbar\omega_D}\frac{d\xi_j}{2E_j}\tanh\left(\frac{E_j}{2k_BT}\right), \tag{2.4}$$

and $g_{jl} = [\mathbf{V}^{-1}]_{jl}$ with

$$\mathbf{V} = \begin{pmatrix} V_{11} & V_{12} & V_{13} \\ V_{12} & V_{22} & V_{23} \\ V_{13} & V_{23} & V_{33} \end{pmatrix}.$$

Let us focus on the solution of Eq. (2.3) with complex gap functions that specify a TRSB state, where there is only one independent vector in Eq. (2.3). Clearly, setting Δ_1 real, which is always possible, one has the following equation,

$$\begin{bmatrix} g_{22} - f_2(E_2, T) & g_{23} \\ g_{23} & g_{33} - f_3(E_3, T) \end{bmatrix} \begin{bmatrix} \mathrm{Im}(\Delta_2) \\ \mathrm{Im}(\Delta_3) \end{bmatrix} = \begin{bmatrix} 0 \\ 0 \end{bmatrix}. \tag{2.5}$$

For the nontrivial solution, one obtains a relation for the absolute values of the gap functions:

$$[g_{22} - f_2(E_2, T)]\,[g_{33} - f_3(E_3, T)] = g_{23}^2. \tag{2.6}$$

Similarly, one has two other relations. The three relations then yield

$$[g_{jj} - f_j(E_j, T)]^2 = \frac{g_{jl}^2 g_{jn}^2}{g_{ln}^2}, \tag{2.7}$$

where $j \neq l \neq n$. Noticing that, in the matrix in Eq. (2.3), all diagonal terms $(g_{jj} - f_j)$ take the same sign as seen from Eq. (2.6), and there is only one independent vector, one can show that $(g_{jj} - f_j)$ and $g_{jl}g_{jn}/g_{ln}$ have the same sign. The relations Eq. (2.7) therefore are rewritten as

$$f_j(E_j, T) = g_{jj} - \frac{g_{jl}g_{jn}}{g_{ln}}. \tag{2.8}$$

Interestingly, they take the same form as for the single-band case, except that the intraband coupling is renormalized by the interband couplings.

There is only one independent vector in the matrix in Eq. (2.3),

$$\frac{\Delta_1}{g_{23}} + \frac{\Delta_2}{g_{13}} + \frac{\Delta_3}{g_{12}} = 0, \tag{2.9}$$

which actually permits complex solutions for Eq. (2.3). From Eq. (2.9), to find a complex solution, one needs to form a triangle using the three segments $|\Delta_j(T)/g_{ln}|$, and therefore

$$\left|\frac{\Delta_j(T)}{g_{ln}}\right| + \left|\frac{\Delta_l(T)}{g_{jn}}\right| > \left|\frac{\Delta_n(T)}{g_{jl}}\right|. \tag{2.10}$$

While varying the temperature, one of these three inequalities may be broken, whereby the system makes a transition to a TRSR state where phase differences between the order parameters take trivial values, i.e. 0 or π. More specifically, the TRSB-to-TRSR state transition takes place when one of the inequalities is replaced by an equality

$$\left|\frac{\Delta_j(T)}{g_{ln}}\right| = \left|\frac{\Delta_l(T)}{g_{jn}}\right| + \left|\frac{\Delta_n(T)}{g_{jl}}\right|. \tag{2.11}$$

The critical temperature of a TRSB superconductor can be derived from Eq. (2.8) by setting $\Delta_j = 0$,

$$N_j(0) \ln \frac{2e^{\gamma}\hbar\omega_{D_j}}{\pi k_B T_c} = g_{jj} - \frac{g_{jl}g_{jn}}{g_{ln}}, \tag{2.12}$$

with the Euler constant $\gamma = 0.577215\cdots$. In the following discussion, we focus on multiband superconductors with a TRSB state as an equilibrium bulk state.

Figure 2.1 shows results from numerical calculations based on the gap functions obtained using the mean-field approximation discussed here. In Fig. 2.1(a), the three gaps functions are equivalent as in the single-band BCS model with $\Delta(0)/k_B T_c = 1.76$. In contrast, in Fig. 2.1(d), kinks appear in the temperature dependence of the three $\Delta_j(T)$ at which the inequality Eq. (2.10) is broken (see Fig. 2.1(f)).

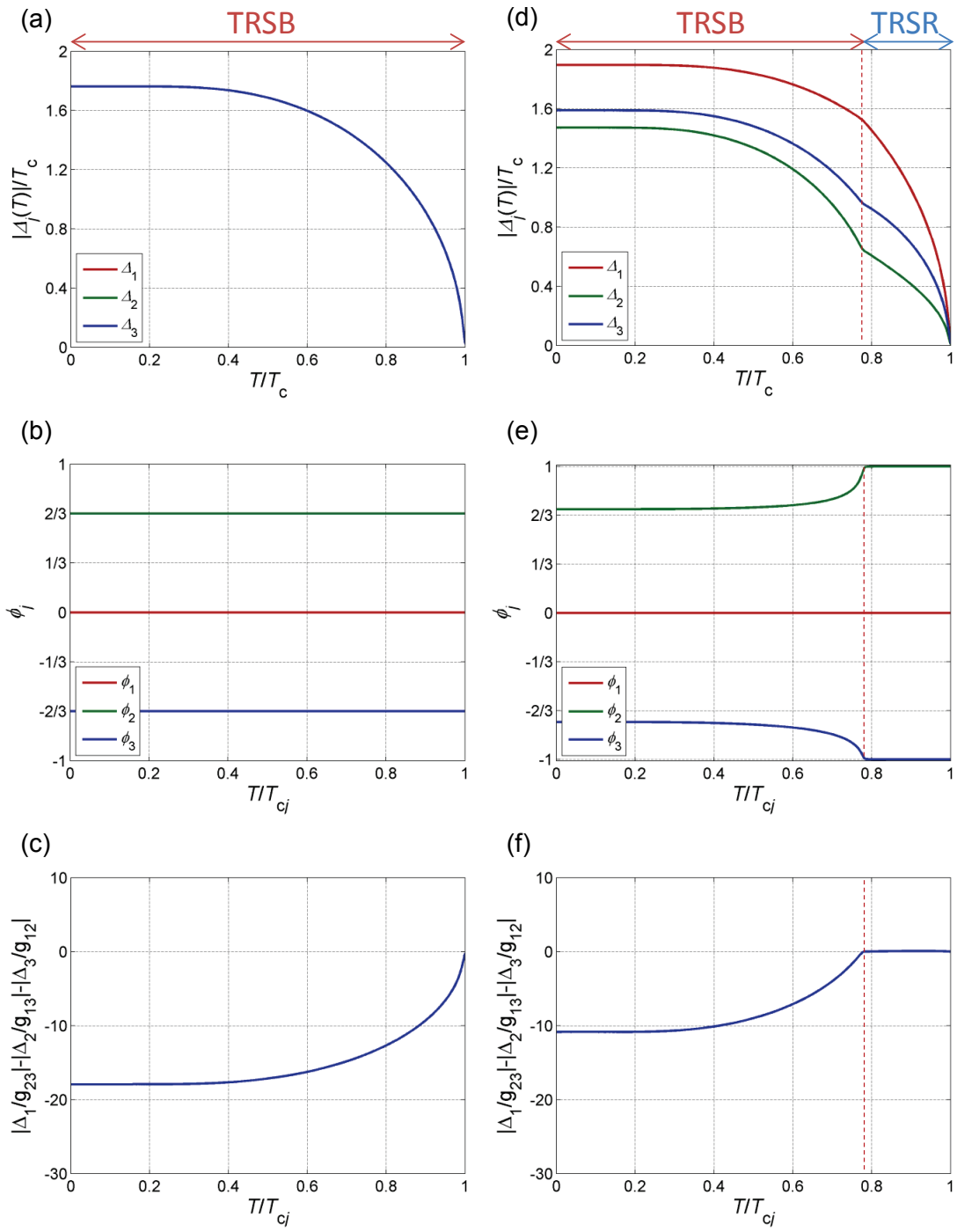

Figure 2.1: Temperature dependence of gap functions $\Delta_j(T)$ obtained from numerical calculations. Both $|\Delta_j(T)|$ and T are normalized by the overall critical temperature T_c. Parameters are given as (a-c) complete isotropic system: $(V_{12}, V_{23}, V_{13}) = (-0.2, -0.2, -0.2)$ and (d-f) anisotropic system: $(V_{12}, V_{23}, V_{13}) = (-0.2, -0.18, -0.21)$ for the interband couplings, with identical intraband couplings $V_{11} = V_{33} = V_{33} = 0.5$ and density of states $N_j(0) = 0.5$. Panels (a, d) and (b, e) are amplitude and phases of gaps (The phase of the first-band is fixed as $\phi_1 = 0$). Panels (c, f) show the stability of the TRSB state in terms of the inequality relation $|\Delta_1/g_{23}| - |\Delta_2/g_{13}| - |\Delta_3/g_{12}| < 0$.

2.2 Derivation of Multicomponent GL Equations

In focusing on the behavior of the gap functions sufficiently close to the overall T_c, the problem can be stated in terms of the GL formalism. By expanding the coupled BCS equations in Eq. (2.3) near T_c in the same way as in Sec. 1.2, we obtain the multiband version of the GL equations (except for gradient terms),

$$\left(g_{jj} - N_j(0)\ln\frac{2e^\gamma\hbar\omega_D}{\pi k_B T}\right)\Delta_j + \frac{7\zeta(3)N_j(0)}{16(\pi k_B T_c)^2}|\Delta_j|^2\Delta_j + g_{jl}\Delta_l + g_{jn}\Delta_n = 0, \tag{2.13}$$

with $\zeta(3)$ the Riemann zeta-function. By comparing with the conventional expression for the GL equations obtained from Eq. (1.91) and taking the order parameters as $\psi_j = \Delta_j$ [65, 66, 59, 64, 68], one has

$$\begin{aligned}\alpha_j(T) &= -\left[N_j(0)\ln\frac{2e^\gamma\hbar\omega_D}{\pi k_B T} - g_{jj}\right],\\ \beta_j &= \frac{7\zeta(3)N_j(0)}{16(\pi k_B T_c)^2},\\ \gamma_{jl} &= -g_{jl}.\end{aligned} \tag{2.14}$$

Additionally, the m_j's can be found in the same way as for single-band superconductors by neglecting the cross terms between different bands, as done in the other works [65, 66, 59, 64, 68].

2.3 Parameterization for Numerical Simulation

In exploring the magnetic properties in multicomponent TRSB superconductors, an analytic treatment of the vortex states for a TRSB superconductor is very difficult because amplitudes and phases of the order parameters are spatially intertwined; hence, a numerical approach is taken. As the parameterization in numerical simulations is always an important consideration, we begin with a discussion of our choice of numerical parameters in connection with analytical solutions.

Recalling the discussion in Sec. 1.4.3 of the thermodynamic field H_{tc} and nucleation field H_n in a TRSB superconductor, we here consider a simple case, namely that the second and third bands are the same but differ from the first band. In this case, the two characteristic fields are rewritten as

$$H_{tc} = 2\sqrt{\frac{2\pi}{\beta_1}}\left(-\alpha_1 - \frac{\gamma_{12}\gamma_{13}}{\gamma_{23}}\right)\left(\frac{1}{2} + \frac{r_\alpha^2}{r_\beta}\right)^{1/2}, \tag{2.15}$$

$$H_n = 2\kappa_1\sqrt{\frac{2\pi}{\beta_1}}\left(-\alpha_1 - \frac{\gamma_{12}\gamma_{13}}{\gamma_{23}}\right)\frac{r_\alpha r_m + 2 + |r_\alpha r_m - 1|}{2 + 1/r_\alpha r_m}, \tag{2.16}$$

with $r_\alpha = \alpha_{2,3}/\alpha_1$, $r_\beta = \beta_{2,3}/\beta_1$, $r_m = m_{2,3}/m_1$ and $\kappa_1 = (m_1 c/2e\hbar)\sqrt{\beta_1/2\pi}$ as a material-dependent parameter for the first component.

As the simplest but nontrivial case, we set $r_\alpha = 1$, $r_\beta = 1$ and $\gamma_{12} = \gamma_{23} = \gamma_{13}$ corresponding to an isotropic bulk state, and vary the mass ratio r_m between 0 and 1.[1] In this case, the ratio between the nucleation and thermodynamic fields is

$$\rho = H_n/H_{tc} = \kappa_1\frac{3r_m}{2r_m+1}\sqrt{\frac{2}{3}}. \tag{2.17}$$

[1] To see the magnetic response of the intercomponent phases, it is convenient to focus on the regime $r_m < 1$ where the second and third components become smaller than the first, and the TRSB state is suppressed by the magnetic field; the response cannot be seen easily when $r_m > 1$ and the second and third components are equivalent.

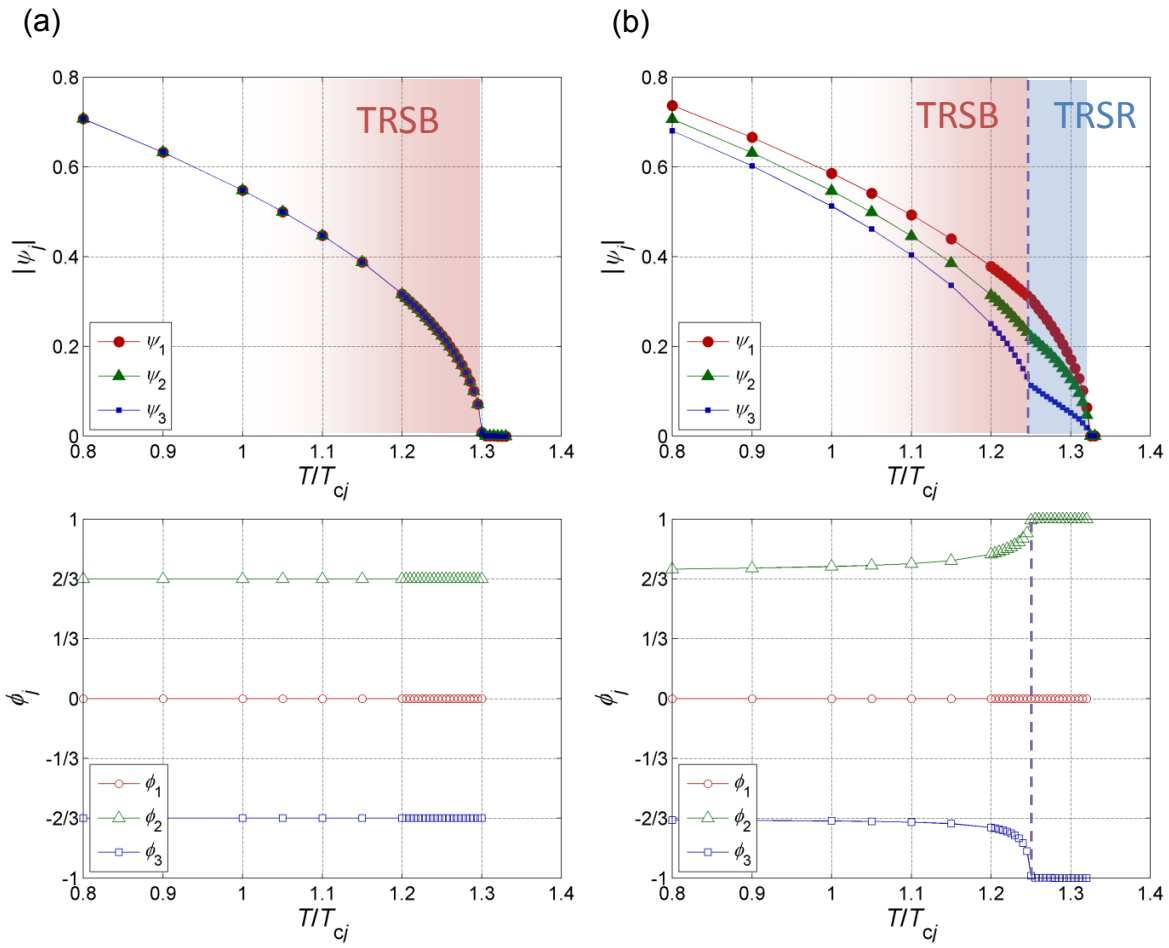

Figure 2.2: Temperature dependence of the order parameters ψ_j in the bulk, represented in polar form with (top) amplitude $|\psi_j|$ and (bottom) phase ϕ_j, obtained using a TDGL method with inter-component couplings (a) isotropic case: $(\gamma_{12}, \gamma_{23}, \gamma_{13}) = (-0.3, -0.3, -0.3)$, and (b) anisotropic case: $(\gamma_{12}, \gamma_{23}, \gamma_{13}) = (-0.32, -0.3, -0.28)$.

As for a single-component superconductor, the magnetic responses of the multicomponent superconductors change drastically across $\rho = H_{\rm n}/H_{\rm tc} = 1$, which corresponds to a characteristic value of κ_1

$$\kappa_1^* = \frac{2r_m + 1}{3r_m}\sqrt{\frac{3}{2}}. \tag{2.18}$$

Hereafter, we perform our numerical study by varying the value of κ_1.[2]

For our numerical calculation based on the multicomponent GL theory, a time-dependent Ginzburg-Landau (TDGL) method is employed. Figure 2.2 shows the temperature dependence of the order parameters in the bulk using the TDGL method. As shown in Fig. 2.2(a), the complete isotropic case preserves the TRSB state over the whole temperature regime up to $T_{\rm c}$. In the TDGL calculation used in the following discussions, the system temperature is set at $T = 0.97T_{\rm c}$ where the GL theory is valid. Note that as shown in Fig. 2.2(b), when the bulk character is anisotropic, the TRSB state becomes unstable near $T_{\rm c}$. As I explore the magnetic properties in a TRSB superconductor using the multicomponent GL theory near $T_{\rm c}$, such *anisotropic bulk* cases are neglected for simplicity.

[2]Our these parameterization does not affect the bulk values, but establishes the response to the fields which is the aspect of greater interest.

Chapter 3

Unconventional Vortex State in Multicomponent TRSB Superconductors

As introduced in Chap. 2, the TRSB state emerges in the system of multiple order parameters with frustrated inter-component couplings, where phase differences among order parameters are neither 0 nor π. Based on the multicomponent GL theory for the TRSB state, it has been indicated that there are more than two coherence lengths diverging at $T_{\rm c}$, and the nucleation field $H_{\rm n}$ and the thermodynamic field $H_{\rm tc}$ have been derived analytically [64]. It is found that the well known GL number $\kappa = \lambda/\xi = 1/\sqrt{2}$ is not appropriate any more for categorizing the TRSB superconductors.

In this chapter, we numerically investigate vortex states in the TRSB superconductors by adopting the time-dependent Ginzburg-Landau (TDGL) approach extended to multi-component system, focusing on the vicinity of the critical temperature where the GL approach is justified. We first analyze the structure of a single vortex, and compare it within that in single-component superconductors. We then investigate the stable configuration of multiple vortices.

For the TDGL calculation here, we obey the condition discussed in Chap. 2 based on the ratio between $H_{\rm tc}$ and $H_{\rm n}$. The parameters which decide bulk properties are given simply as $\alpha_1 = \alpha_2 = \alpha_3, \beta_1 = \beta_2 = \beta_3$ and $\gamma_{12} = \gamma_{23} = \gamma_{13}$, but only masses are parameterized as $m_2 = m_3 = r_m \cdot m_1$ with $0 < r_m < 1$. For these parameters, the amplitudes of three order parameters are equivalent, and phase differences are $2\pi/3$ in the bulk state. For $\rho \equiv H_{\rm n}/H_{\rm tc} < 1$, type-I superconductivity appears associated with the first-order transition from the Meissner state to the normal state. While for $\rho > 1$, penetration of vortices into a bulk sample is expected. To investigate vortex solutions by the TDGL method, a periodic boundary condition is adopted to fix the number of vortices in a system (See App. A for details).

This chapter is partly reproduced from; Y. Takahashi, Z. Huang and X. Hu, *Physica C* **493**, 82 (2013).

3.1 Single-Vortex Solution

Using the TDGL method, single-vortex structures in the TRSB superconductor are demonstrated. We here consider the two cases that the mass ratio $r_{\rm m}$ is taken as $r_{\rm m} = 1$ and $r_{\rm m} = 0.3$, with threshold value $\kappa_1^* \approx 1.22$ and $\kappa_1^* \approx 2.18$, respectively. For the present TDGL calculation, the material parameter κ_1 is fixed as $\kappa_1 = 2.5$.

Figure 3.1 shows the TDGL result for single-vortex solution. Parameters are taken as $\kappa_1 = 2.5, \gamma_{jk} = -0.3|\alpha_{10}|$, and $T = 0.97T_{\rm c}$. To characterize the vortex structures quantitatively, I try to fit the order parameters by $f(r) \approx \tanh(r/\xi)$ and the magnetic flux density by $b(r) \approx \Phi_0/(2\pi\lambda^2)K_0(r/\lambda)$, as discussed in Sec. 1.1 for for single-component superconductors. It is clearly

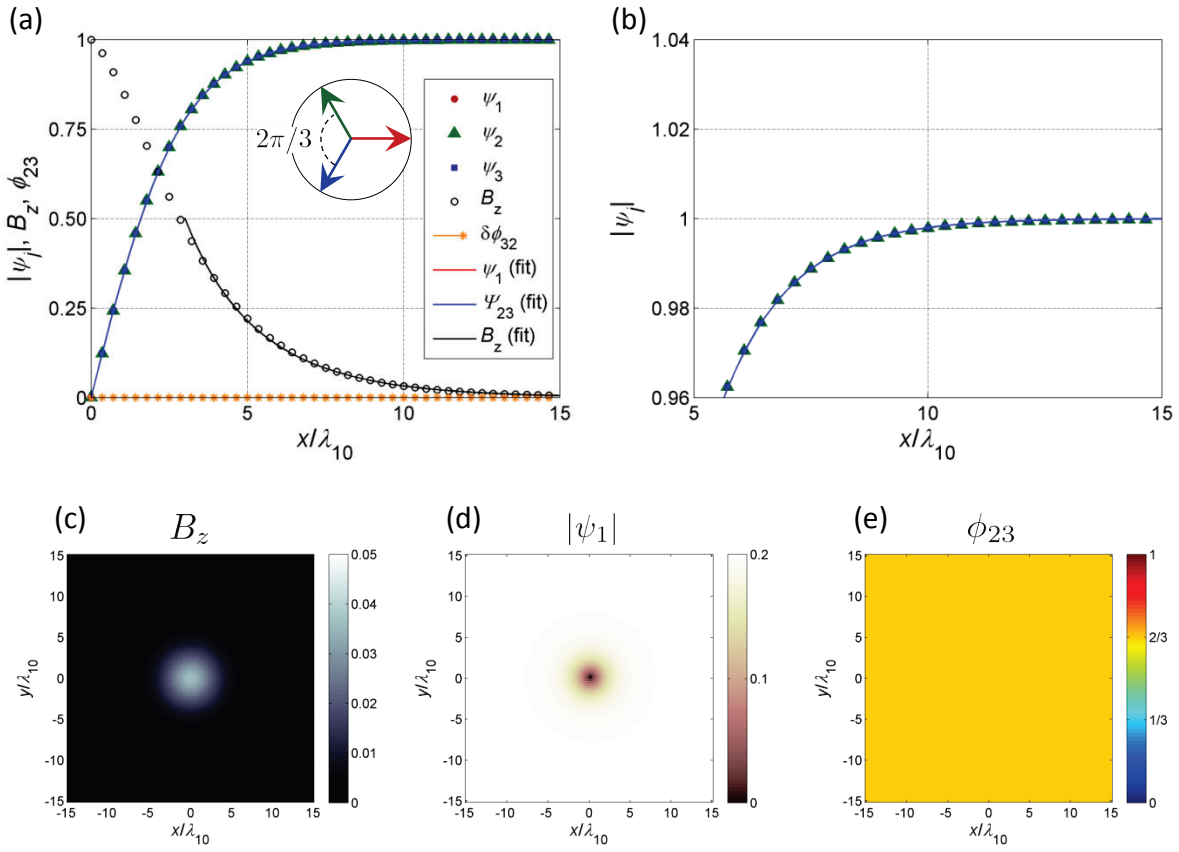

Figure 3.1: Single vortex structure in a multicomponent TRSB superconductor of isotropic mass ratio ($r_m = 1$). Parameters are given as $\kappa_1 = 2.5, \gamma_{jk} = -0.3|\alpha_{10}|$ and $T = 0.97T_c$. (a) Vortex structure in radial direction denoting TDGL results (marks), fittings (lines) and deviation of intercomponent phase ($\phi_{23} = \phi_3 - \phi_2$) from $2\pi/3$ (stem plots). $|\psi_j|$ and ϕ_{23} are normalized by the bulk values, and B_z is normalized by the value at the center of vortex core. (b) Enlarged view of panel (a) near bulk values of order parameters. Bottom panels represent the simulation boxes for (c) B_z, (d) $|\psi_1|$ and (e) ϕ_{23}.

seen that good agreements are achieved with $\xi = 2.9$ and $\lambda = 3.4$. Because the fitting function for the magnetic field density $b(r)$ is applicable at the region where order parameters are almost recovered to bulk values, the fitting result seems acceptable with cut-off at $r \sim \xi$. The phase differences between the three components hold the bulk value of $2\pi/3$ in the whole space. Therefore, the vortex structure in the isotropic system is essentially same as that in conventional single-component superconductors.

In contrast, the vortex structure in the anisotropic system of $r_m = 0.3$ in Fig. 3.2 shows differences from the isotropic case. We obtain two recovery lengths of order parameters with $\xi_1 \approx 3.1$ and $\xi_{23} \approx 3.9$ for respectively $|\psi_1|$ and $|\psi_{2,3}|$, and a penetration depth of the magnetic field with $\lambda \approx 2.5$. Actually, as seen in the Fig. 3.2(b), the amplitudes of order parameters cannot be fitted by the functions away from the vortex core. Additionally, the phase difference between second and third order parameters deviates from the bulk value of $2\pi/3$ as indicated by the stem plots. Due to the magnetic flux density in the vortex core, the order parameters are suppressed with coupled distortions of amplitudes and phases.

We hereby characterize that there are multiple length scales, namely recovery lengths of each order parameter $|\psi_j|$, phase modulation $\delta\phi_{23}$ and penetration depth λ. Figure 3.3 shows temperature dependence of the multiple length scales for the anisotropic mass ratio of $r_m = 0.3$. It is notable that

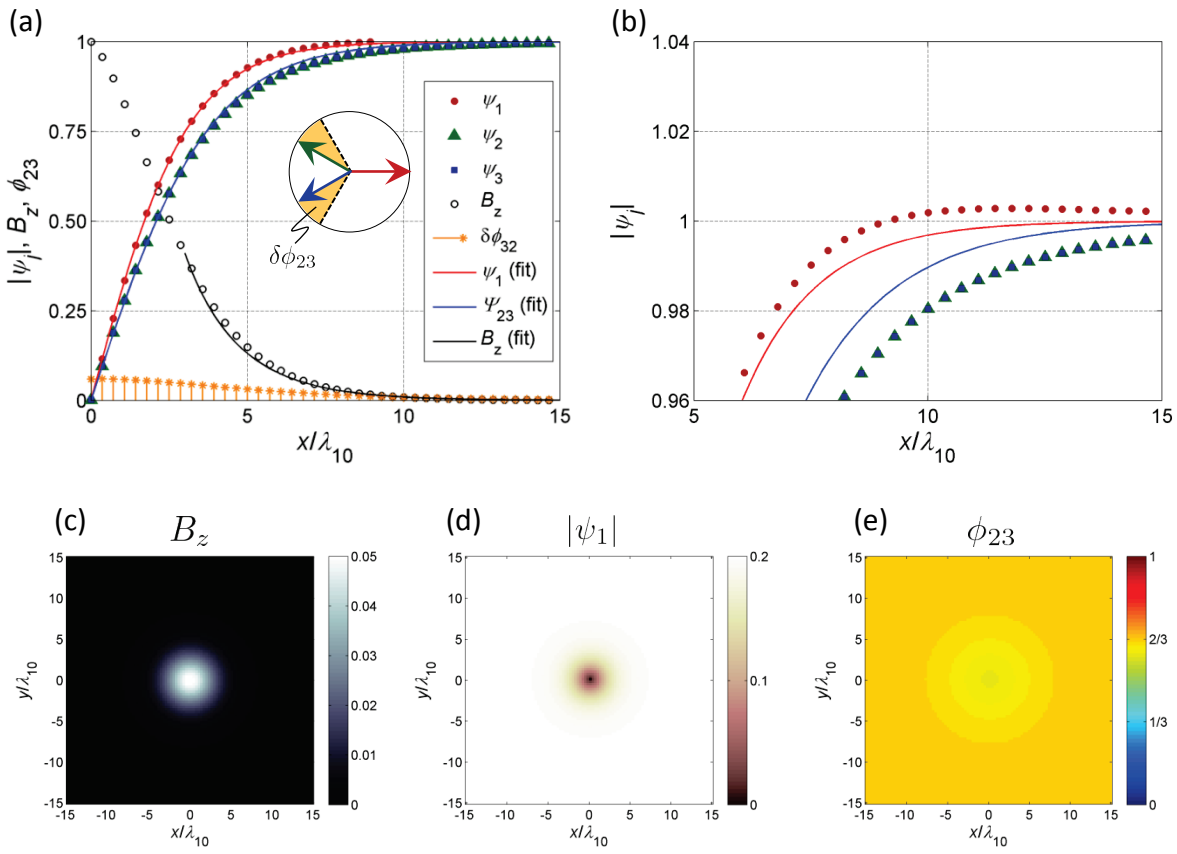

Figure 3.2: Same as Fig. 3.1 except for $r_m = 0.3$.

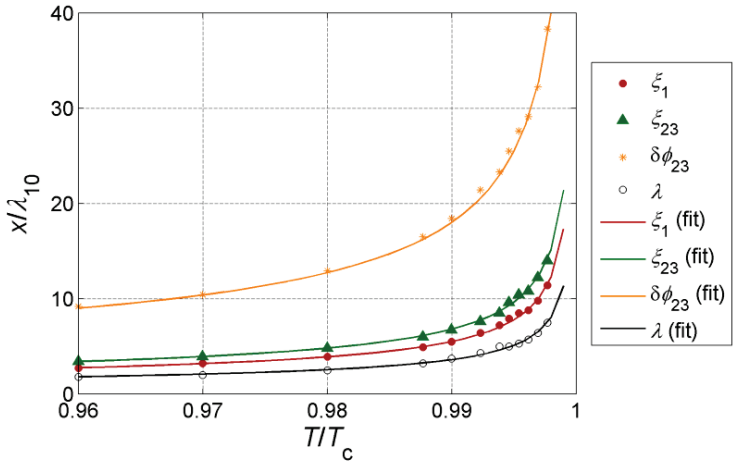

Figure 3.3: Temperature dependence of multiple length scales diverging up to the critical temperature T_c as $\propto (1 - T/T_c)^{-1/2}$. Parameters are $r_m = 0.3$ and $\kappa_1 = 2.5$.

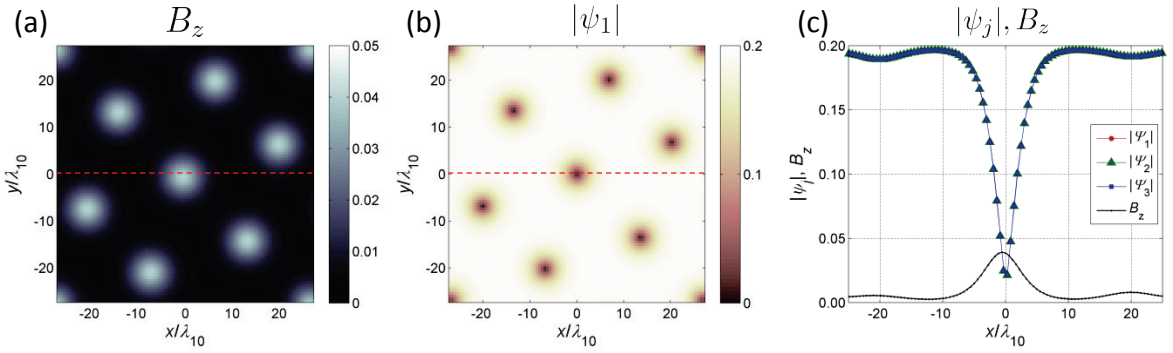

Figure 3.4: 8-vortex solution in the isotropic system $r_m = 1$ ($\kappa_1^* \approx 1.22$) calculated with $\kappa_1 = 2.0$. (a) Magnetic induction B_z. (b) Amplitudes of order parameters $|\psi_j|$ ($|\psi_1| = |\psi_2| = |\psi_3|$ all same here). (c) Spatial profiles of $|\psi_j|$ and B_z in the x-direction as indicated by the red line in (a) and (b).

in addition to the coherence length ξ_j and also penetration depth λ, we have another length scales associated with phase modulation between components, which are divergent with temperature up to T_c.

3.2 Multi-Vortex Solution

We next discuss interaction between vortices in a TRSB superconductor with performing TDGL calculations with multiple vortex numbers. Figure 3.4 shows a result of multi-vortex configurations for the isotropic system of ($r_m = 1$) where conventional vortex structure is confirmed as seen in Fig. 3.1. As expected, a typical vortex-lattice configuration can be found same as that in single-component superconductors. Such a vortex-lattice configuration can be seen any κ_1 values with $\kappa_1 > \kappa_1^*$.

On the other hand, interesting vortex configuration is found for the anisotropic system of $r_m = 0.3$. Fig. 3.5 shows the results for $\kappa_1 = 2.25$ which is slightly above $\kappa_1^* \approx 2.18$ for this mass ratio. As seen in Fig. 3.5 (b) for the order parameters, eight separated vortices clearly form a "cluster", which indicates that the vortex-vortex interaction is attractive in long range and repulsive in short range. It is noted for Fig. 3.5(a), referring to the magnetic flux density, tjat separation of magnetic fluxes is obscure. This is probably corresponding to a larger penetration depth than the distances between neighboring vortices. Figure 3.5(c) refers to the profiles of the vortices across the x-axis direction. It

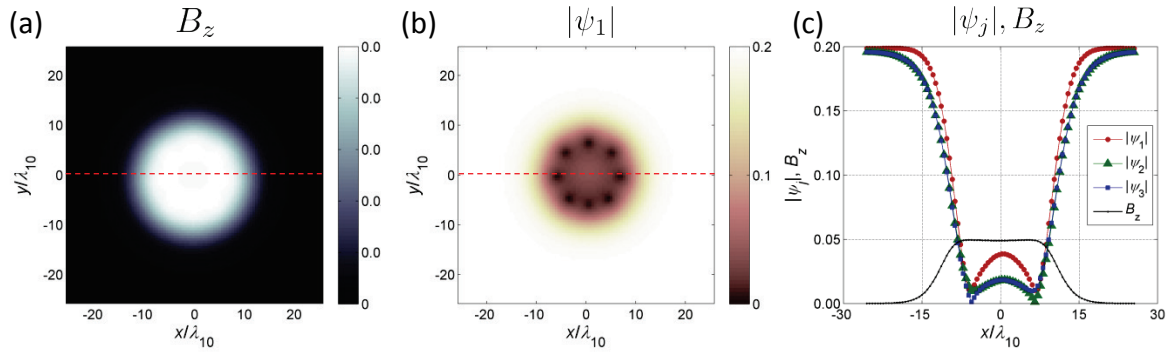

Figure 3.5: 8-vortex solution in the anisotropic system $r_m = 0.3$ ($\kappa_1^* \approx 2.18$) calculated with $\kappa_1 = 2.25$. (a) Magnetic induction B_z. (b) Amplitudes of order parameters $|\psi_j|$. (c) Spatial profiles of $|\psi_j|$ and B_z in the x-direction as indicated by the red line in (a) and (b).

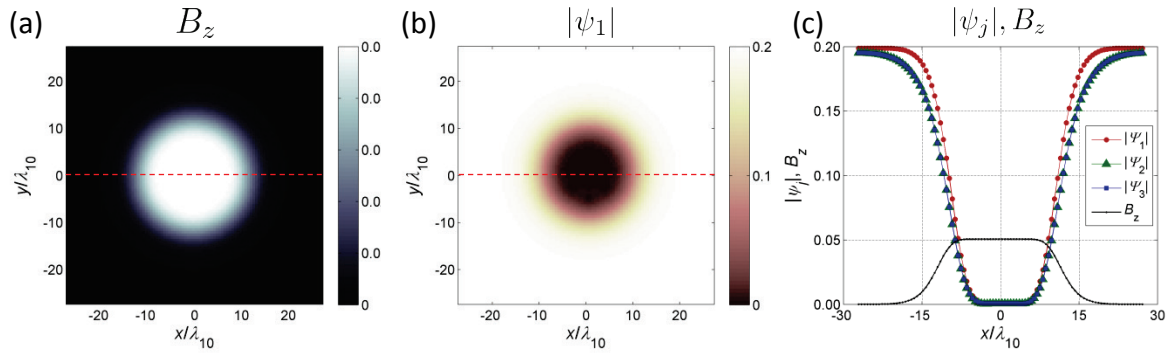

Figure 3.6: Same as Fig. 3.5 except for $\kappa_1 = 2.1$.

is obvious that the amplitudes of order parameters recover to finite values at the center of the domain region.

For comparison, we present in Fig. 3.6 the results for $\kappa_1 = 2.1$ which is slightly below $\kappa_1^* = 2.18$. One finds a giant vortex state with $N = 8$ vorticity which indicates the type-I nature. In the normal region, the order parameters are completely suppressed by the magnetic field as seen in Fig. 3.6(c), in sharp contrast with that in Fig. 3.5(c).

3.3 Summary

In this chapter, we have numerically investigated both single and multiple vortex structures in the TRSB superconductivity at the vicinity of the critical temperature T_c with the TDGL approach. In the isotropic case where the three components have the equivalent strength with same inter-component couplings, the system simply behaves as type-I and type-II superconductor on the two sides of $H_n = H_{tc}$, same as single-component superconductors. However in anisotropic systems, the formation of vortex cluster is revealed for $H_n \gtrsim H_{tc}$, which cannot be observed in conventional superconductors. We will investigate further details of the mechanism for this novel vortex state in the next chapter.

Chapter 4

H-T Phase Diagram of Multicomponent TRSB Superconductors

In the previous chapter, single and multiple vortex solutions in the TRSB superconductor are studied by means of the multicomponent TDGL method. From the single-vortex solutions, we found an intrinsic vortex structure in the TRSB superconductor that there are multiple divergent length scales different from conventional one. From the multi-vortex solutions, we observed interesting vortex state in which vortices form a cluster as its equilibrium state instead of forming a typical lattice structure, at a certain condition where the nucleation field $H_{\rm n}$ is slightly larger than the thermodynamic field $H_{\rm tc}$. The appearance of such unconventional states also indicates that the TRSB superconductor is not straightforwardly categorized to type-I or type-II by the GL parameter $\kappa = \lambda/\xi = 1/\sqrt{2}$.

As a matter of fact, several numerical calculations using multicomponent GL theory exposed anomalous magnetic properties such as fractional vortices or unconventional vortex states [58, 69, 61, 59, 70, 71, 72, 73, 74]. However, a systematic study seems lacking, and magnetic phase diagrams are unclear at the moment of this writing.

For the purpose of comprehensive understanding in magnetic properties of a TRSB superconductor, we further study vortex states, especially focusing on mechanism of the exotic unconventional state, and aim to construct a H-T phase diagram in this chapter. We first discuss vortex states and a mechanism of vortex cluster simulated by the TDGL method. Then, interface energies in a TRSB superconductor is calculated for understanding classification of TRSB superconductor. Finally, all results are summarized in the H-T phase diagrams.

This chapter is reproduced with permission from; Y. Takahashi, Z. Huang and X. Hu, *J. Phys. Soc. Jpn.* **83**, 034701 (2014).

4.1 Vortex States in TRSB Superconductors

We here adopt the TDGL method again with the magnetic periodic boundary condition which confines fixed number of vortices N in the simulation box (see App. A). The results shown below are for $N = 8$, while we have confirmed the main conclusions remain valid using large systems. As a material parameters, we set as $r_{\rm m} = 0.3$ meaning anisotropic mass ratio which gives $\kappa_1^* \approx 2.18$, and κ values are parametrized.

Figure 4.1 shows vortex configurations at three distinctive parameter regimes, where $H_{\rm n} < H_{\rm tc}$ ($\kappa_1 < \kappa_1^*$), $H_{\rm n} \gtrsim H_{\rm tc}$ ($\kappa_1 \gtrsim \kappa_1^*$) and $H_{\rm n} \gg H_{\rm tc}$ ($\kappa_1 \gg \kappa_1^*$). In Fig. 4.1(a-e) where $\kappa_1 < \kappa_1^*$, we observe a typical phase separation between superconductivity and normal states which represents a type-I superconductor. This result is the same as the conventional single-component superconductors.

As seen in Fig. 4.1(a), the order parameters show different recovery lengths from normal to bulk superconductivity region due to anisotropic mass ratio r_m.

For $\kappa_1 \gtrsim \kappa_1^*$, we find an unconventional vortex state. Figures 4.1(f-k) show a vortex cluster, where multiple vortices ($N = 8$) form a domain of vortex bundle. As seen in Fig. 4.1(f), the order parameters have finite values inside the domain region which is clearly different from Fig. 4.1(a). As seen in Fig. 4.1(k), phase differences inside the cluster are either zero or π indicating a TRSR state, while the bulk region keeps a TRSB state ($\phi_{jk} = 2\pi/3$). This phase separation between TRSB and TRSR states is essential for the stability of vortex cluster. It is noted that for the vortices locating at the phase boundary the vortex cores are not overlapping for the three components.

For $\kappa_1 \gg \kappa_1^*$, Figs. 4.1(l-q) show typical triangular vortex-lattice configurations which represent a type-II superconductor. In this parameter regime, order parameter phase differences at the vortex core are slightly modulated from bulk values, and no TRSR domain can be observed.

It is noted that when the system is totally isotropic, namely $r_m = 1$, the vortex-cluster state does not appear, where modulation in amplitudes and phases in order parameters are decoupled as discussed in Ref. [64].

4.2 Interface Energy in TRSB Superconductors

In a single-component superconductor, the GL parameter $\kappa = 1/\sqrt{2}$ given by the condition $H_{\rm n} = H_{\rm tc}$ coincides with that where sign change in interface energy takes place [75, 76], which dichotomizes a superconductor into type-I or type-II. Therefore, it is interesting to evaluate interface energy in the TRSB superconductor where the vortex-cluster state appears, and thus the simple classification of type-I and type-II superconductor does not apply. For this purpose, we calculate the excess Gibbs free energy in a one-dimensional system,

$$\Gamma = \int_0^\infty (g_{\rm sH} - g_{\rm s0}) dx, \tag{4.1}$$

where, $g_{\rm sH}$ and $g_{\rm s0}$ are energy density with and without applied fields, respectively. Calculation of interface energy essentially needs a numerical approach as shown for a single-component superconductor [6] and for a two-component cases [77]. We here use the multicomponent TDGL scheme for one-dimensional system.

The boundary conditions are given,

$$\begin{aligned} &|\psi_j| = 0 \text{ and } B(x) = H_{\rm tc} \quad \text{for } x \to 0 \\ &|\psi_j| = |\psi_{j0}| \text{ and } B(x) = 0 \quad \text{for } x \to \infty \end{aligned}$$

where $|\psi_{j0}|$'s are bulk values of order parameters in each component, and $H_{\rm tc}$ is the thermodynamic field of TRSB superconductor in Eq. (2.15).

Typical interface structure is shown in Fig. 4.2(a) for $r_m = 0.3$ and $\kappa_1 = 3$. As we have seen in the single-vortex structure, there are several length scales which are intrinsically observed in a TRSB superconductor with anisotropic mass ratio. In addition to typical spatial variations for B_z and $|\psi_j|$, it should be noted that while the phase difference indicates a TRSB state ($\phi_{23} = 2\pi/3$) at the one side of bulk region ($|\psi_j|/|\psi_{j0}| = 1$ and $B_z/H_{\rm tc} = 0$), the phase difference ϕ_{23} is slightly modulated from the bulk value at the other side at the normal state ($|\psi_j|/|\psi_{j0}| = 0$ and $B_z/H_{\rm tc} = 1$).

Figure 4.2(b) shows κ_1 dependence of the interface energy Γ for several typical values of mass ratio r_m. Numerical errors are negligible in these plots. The interface energy decreases monotonically and changes its sign with increase of κ_1 at κ_1^{**}. Therefore in a TRSB superconductor, there are two typical thresholds κ_1, for example, $\kappa_1^{**} \approx 3.0$ and $\kappa_1^* \approx 2.18$ for $r_m = 0.3$, which makes it much different from a TRSR superconductor.

Based on the above results, a phase diagram for material paramters is constructed in Fig. 4.3, with two phase boundaries κ_1^* and κ_1^{**} which separate the Meissner phase, vortex-cluster phase and

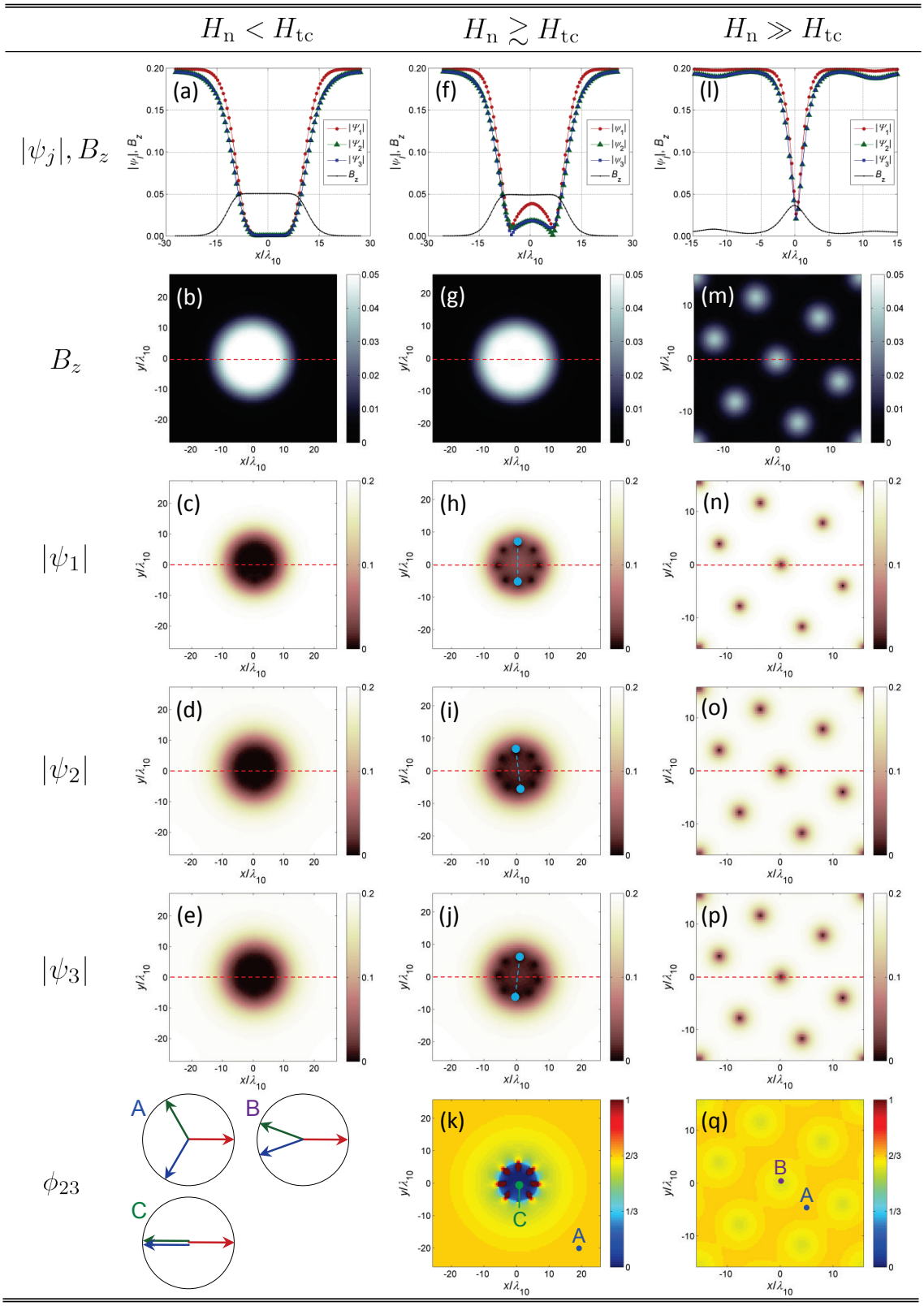

Figure 4.1: Typical vortex configurations solved by the TDGL method for (a-e) $H_n < H_{tc}$, (f-k) $H_n \gtrsim H_{tc}$ and (l-q) $H_n \gg H_{tc}$, for $\kappa_1 = 2.0$, $\kappa_1 = 2.25$ and $\kappa_1 = 6.0$, respectively, with the mass ratio $r_m = 0.3$, interband couplings $\gamma_{12} = \gamma_{23} = \gamma_{13} = -0.3|\alpha_{10}|$ and temperature $T = 0.97T_c$. Panels (a, f, l) are spatial profiles of $|\psi_1|$, $|\psi_2|$, $|\psi_3|$ and B_z along $y = 0$ (red line) on the other panels. Panels (b, g, m) denote magnetic induction B_z. Panels (c, h, n), (d, i, o), (e, j, p) denote amplitude of order parameters $|\psi_1|$, $|\psi_2|$ and $|\psi_3|$, respectively. Panels (k, q) denote phase difference between the second and third components ϕ_{23}.

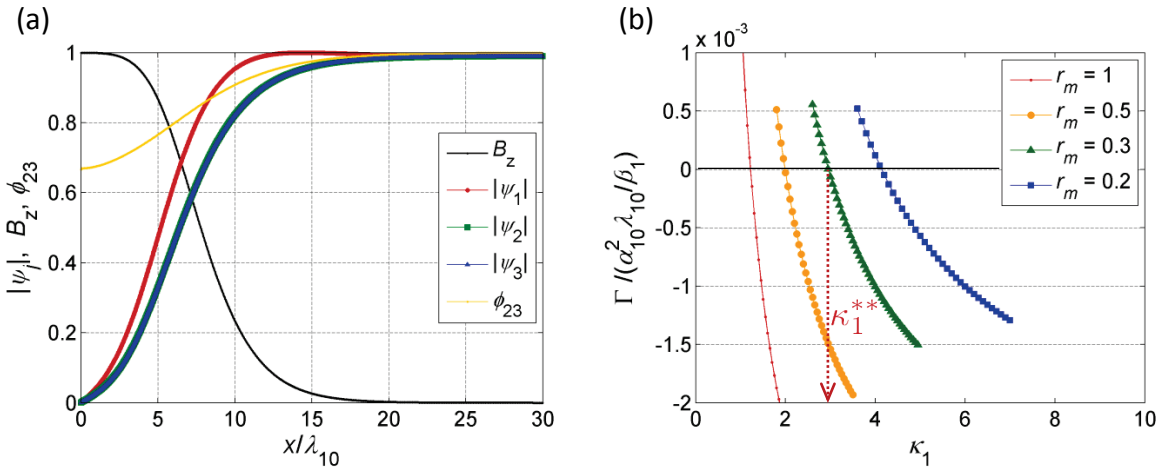

Figure 4.2: (a) Typical TDGL calculation result to evaluate the interface energy Γ representing spatial variation of $|\psi_j|$, ϕ_{23} and B_z, which are normalized by bulk values $|\psi_{j0}|$, $\phi_{23} = 2\pi/3$ and the thermodynamic field $H_{\rm tc}$, respectively. (b) κ_1 dependence of the interface energy Γ in TRSB superconductors. Γ is normalized by the thermodynamic field for the first component without inter-component coupling.

vortex lattice phase. The two phase boundaries overlap at $r_{\rm m} = 1$, which is consistent with the fact that no vortex-cluster state can be found in the isotropic system.

4.3 Vortex States at $H \lesssim H_{\rm n}$

Here we consider the field dependence of vortex states in the regime $\kappa_1^* < \kappa_1 < \kappa_1^{**}$ where a vortex cluster is observed. Variations of the system upon sweeping applied magnetic fields is simulated by changing the number of vortices N with fixed system size. Figure 4.4 shows the vortex configurations with the same material parameters and system size as those in Fig. 4.1(f-k) but with different vortex number (a) $N = 8$ and (b) $N = 36$. Figure 4.4(a) represents a vortex state at lower magnetic field, forming a typical vortex cluster state. On the other hand, a typical vortex lattice is observed in Fig. 4.4(b), and apparently the phase differences between order parameters are either 0 or π associated with a TRSR state in the whole system. Here, order parameters are suppressed by the magnetic field in different ways in accordance with effective masses m_j, which results in a breaking of the stability condition of TRSB state in Eq. (1.105). The magnetic-field-induced TRSB to TRSR transition is seen for $\kappa_1 > \kappa_1^*$.

4.4 H-T Phase Diagrams of TRSB Superconductors

In this section, we construct H-T phase diagrams of multicomponent TRSB superconductor in the three regimes (a) $H_{\rm n} < H_{\rm tc}$ ($\kappa_1 < \kappa_1^*$), (b) $H_{\rm n} \gtrsim H_{\rm tc}$ ($\kappa_1^* < \kappa_1 < \kappa_1^{**}$) and (c) $H_{\rm n} \gg H_{\rm tc}$ ($\kappa_1 > \kappa_1^{**}$).

In Fig. 4.5(a), the TRSB superconductor shows simply typical type-I property. At high magnetic fields, superconductivity with a TRSB state is totally suppressed, and transfers to a normal state ($|\psi_j| = 0$). This is essentially the same H-T phase diagram as a conventional single-component superconductor. The phase transition between Meissner and normal states is unambiguously first order.

Figure 4.5(b) shows the novel H-T phase diagram which includes the vortex-cluster state as an unconventional intermediate phase. The vortex-cluster phase is located above the lower critical field H_{c1} where vortices start to penetrate into a superconductor. For the stronger magnetic field slightly

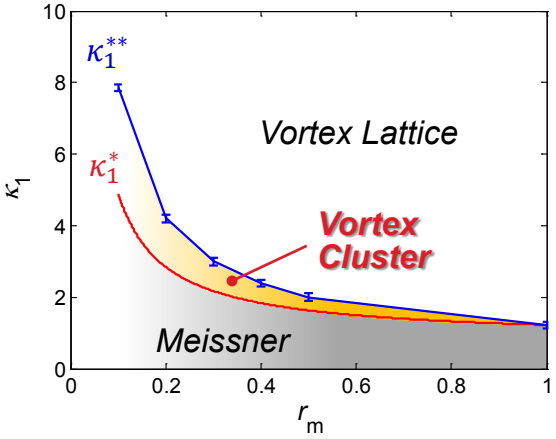

Figure 4.3: Phase diagram for vortex state in the TRSB superconductor in terms of $r_{\rm m}$ and κ_1 including the Meissner, vortex cluster and vortex lattice phases. See text for definitions.

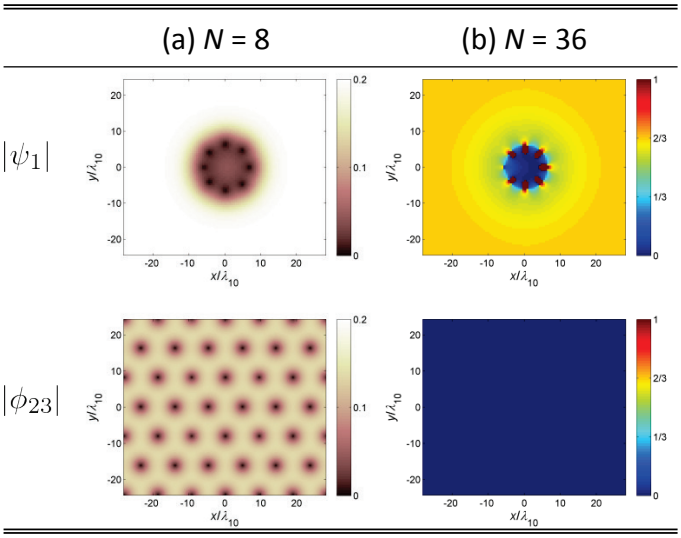

Figure 4.4: Vortex configurations representing amplitude of ψ_1 and order parameter phase difference ϕ_{23} calculated with magnetic flux number (a) $N = 8$ and (b) $N = 36$. Material parameters are same as in Fig. 4.1(d-g).

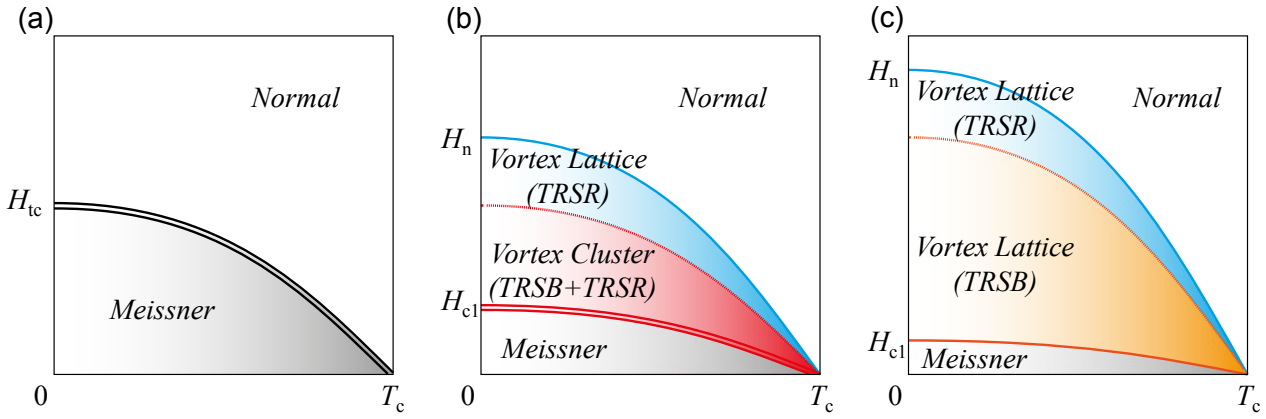

Figure 4.5: *H-T* phase diagrams for multicomponent superconductors with frustrated intercomponent couplings. Three diagrams are characterized by conditions: (a) $H_{\rm n} < H_{\rm tc}$ ($\kappa_1 < \kappa_1^*$), (b)$H_{\rm n} \gtrsim H_{\rm tc}$ ($\kappa_1^* < \kappa_1 < \kappa_1^{**}$) and (c) $H_{\rm n} \gg H_{\rm tc}$ ($\kappa_1 > \kappa_1^{**}$). The double and single lines represent first- and second-order transition, respectively. The dashed line represents the TRSB-TRSR transition.

below the nucleation field $H_{\rm n}$, a conventional vortex lattice with TRSR state appears as shown in Fig. 4.4.

The phase transition between the vortex cluster and the Meissner states is likely not continuous. The second-order transition at $H_{\rm c1}$ in a type-II superconductor is understood by additional Gibbs free energy ΔG due to vortex penetration represented by [6]

$$\Delta G = G_s\big|_{\text{first flux}} - G_s\big|_{\text{no flux}} = \frac{B}{\Phi_0}\epsilon_1 + \sum F_{ij} - \frac{BH}{4\pi},$$

where ϵ_1 is vortex line energy and $F_{ij} = \frac{\Phi_0^2}{8\pi^2\lambda^2}K_0(\frac{r_{ij}}{\lambda})$ is vortex interaction energy with the zeroth Bessel function K_0. For conventional case with repulsive vortex interaction, the energy cost is $\Delta G \approx 0$ because B is much small inside the superconductor ($B \approx 0$), and the interaction energy is also negligible ($F_{ij} \approx 0$) as inter-vortex distance is large enough. However when vortices form a cluster as observed in the TRSB superconductor, vortices penetrate into a superconductor feeling finite interaction energy F_{ij}, and consequently the system will see a finite energy jump ΔG which corresponds naturally to a first-order transition.

Finally, Fig. 4.5(c) shows the *H-T* phase diagram for $H_{\rm n} \gg H_{\rm tc}$ ($\kappa_1 > \kappa_1^{**}$). Since the vortex lattice state is observed at magnetic fields $H_{\rm c1} \leq H \leq H_{\rm n}$, the phase diagram is essentially same as the single component case. However, it is remarked that there are two regimes in terms of order parameter phase configurations. For a low magnetic field regime, order parameter phases are locally modulated only in a vortex core, and the overall system preserves a TRSB state. For a high magnetic field slightly below $H_{\rm n}$, the system transfers to a TRSR state as seen in Fig. 4.4. Between the two states, vortex configurations do not show obvious differences and inter-vortex distance changes proportionally to strength of applied magnetic field.

4.5 Discussions

Using a numerical approach on multicomponent GL theory, we have revealed that, in a multicomponent superconductor with frustrated intercomponent couplings, a vortex-cluster state appears at an intermediate magnetic field regime between Meissner and vortex lattice states when the material parameters satisfy $H_{\rm n} \gtrsim H_{\rm tc}$. While numerical results are shown explicitly for the case where the material parameter of the first component κ_1 and mass ratios between the components r_m are varied whereas the other parameters relevant to a bulk value of order parameter are put the same,

the appearance of a vortex-cluster state is general for all possible parameters as far as the stability conditions of a TRSB state discussed in Chap. 2 are satisfied except for the isotropic case.

The vortex-cluster state is expected to be observable by conventional vortex imaging methods. It is also interesting to examine the behavior of magnetization around H_{c1}. The magnetization curve will be different from either that of type-I or that of type-II superconductor. Careful experiments are required and such unique magnetic behavior will also support the novelty of a TRSB superconductor.

It is appropriate to make some discussions on the nature of transition between the vortex cluster and vortex lattice. Since the spatial symmetry is different between the two states, a weak first-order transition is expected. However, in the present work we could not find clear evidences for it since no thermodynamic quantity has been calculated directly. On the other hand, the nature of the TRSB-TRSR transition in Fig. 5(c) is a more subtle issue. This transition has only been discussed in absence of magnetic field (and thus without any vortex) [52, 63]. While it was argued to be first order [52], a numerical analysis indicated a continuous transition [63]. Therefore, the nature of TRSB-TRSR transition remains to be an issue to be addressed in future works.

The vortex-cluster state associated with domain separation of the time-reversal symmetry has been also reported in the numerical studies based on the three-component GL theory [61, 69]. It is mentioned in these studies that vortex cores of individual components do not overlap at the domain boundary, suggesting the existence of *fractional vortices*. In the present study, similar vortex-cluster structure is observed as indicated on the panels in Fig. 4.1(h-j), where blue lines denote orientation of the vortex cluster. However, separation of the cores is still unclear, and possibility of fractional vortices should be studied further. While fractional vortices which appear at the boundary between two chiral TRSB superconductors were studied well [59, 58, 69], those at a boundary between TRSB and TRSR states are also interesting.

4.6 Summary

Magnetic properties of multiband superconductors with frustrated interband couplings are investigated by means of the multicomponent Ginzburg-Landau (GL) theory, and we have investigated response of the novel superconducting state to an external magnetic field. When parameters satisfy the condition $H_{\rm n} \gtrsim H_{\rm tc}$, with $H_{\rm n}$ the nucleation field and $H_{\rm tc}$ the thermodynamic field, we have revealed the novel H-T phase diagram including the unconventional vortex state, namely *vortex cluster*, which cannot be categorized to either type-I or type-II. The vortex cluster is associated with local domain separation between time-reversal symmetry broken and time-reversal symmetry reserved states, and it is expected to appear via a first order transition from the Meissner state. We have studied the interface energy in a time-reversal-symmetry broken superconductor, and found that material parameters for sign change in the interface energy do not coincide with those for $H_{\rm tc} = H_{\rm n}$.

Chapter 5

Magnetization Curves of Multicomponent TRSB Superconductors

The H-T phase diagrams for multicomponent superconductors with frustrated intercomponent couplings are constructed that includes the unconventional vortex state (*vortex-cluster* (VC)) located above the lower critical field H_{c1} at which vortices start to penetrate a superconductor. It is well established in conventional type-II superconductors that the phase transition at H_{c1} is second-order as the excess vortex-line energy and negative interface energy are compensated, and the vortex-interaction energy is negligible because of the repulsion [6]. However, when the vortex interaction is not simply repulsive, as in the VC state, such a conventional scenario is not appropriate and the phenomenological behavior at H_{c1} is nontrivial. Whereas all previous discussions on the vortex states in multicomponent superconductors have been based on equilibrium states, we pay special attention to the transient vortex states that arise in for example the magnetization process.

For this purpose, the TDGL method is an added useful approach that enables the magnetization process of a superconductor to be simulated subject to a boundary condition associated with the applied magnetic fields. we here employ this method to model the magnetization (M-H) curves of multicomponent superconductors with frustrated intercomponent couplings, and discuss the dynamics of vortex penetration at H_{c1}. The numerical details are explained in App. A

To discuss vortex penetration, the choice of boundary conditions is an important issue that directly affects conclusions. As introduced in App. A, we employ the two boundary conditions for the *superconductor-ferromagnet* (SC-FM) and *superconductor-insulator* (SC-I) interfaces, and compare the results. The disadvantage to note in using the S-I boundary condition is that vortices at H_{c1} are excessively screened at the boundary and larger applied fields than H_{c1} are needed [78]. This screening is inconvenient when probing the VC phase.

Because we shall focus on macroscopic properties, the simulation box is prepared as large as possible so as to contain many vortices even at H_{c1}. The size of the simulation box is set at $150\lambda_{10} \times 130\lambda_{10}$. The modeled magnetization curves are thereby sufficiently smooth, which differ markedly from those for mesoscopic systems.[1]

[1] M-H curves in mesoscopic systems show "step-like" behaviors because vortex penetration into a system causes a finite energy difference owing to boundary effects.

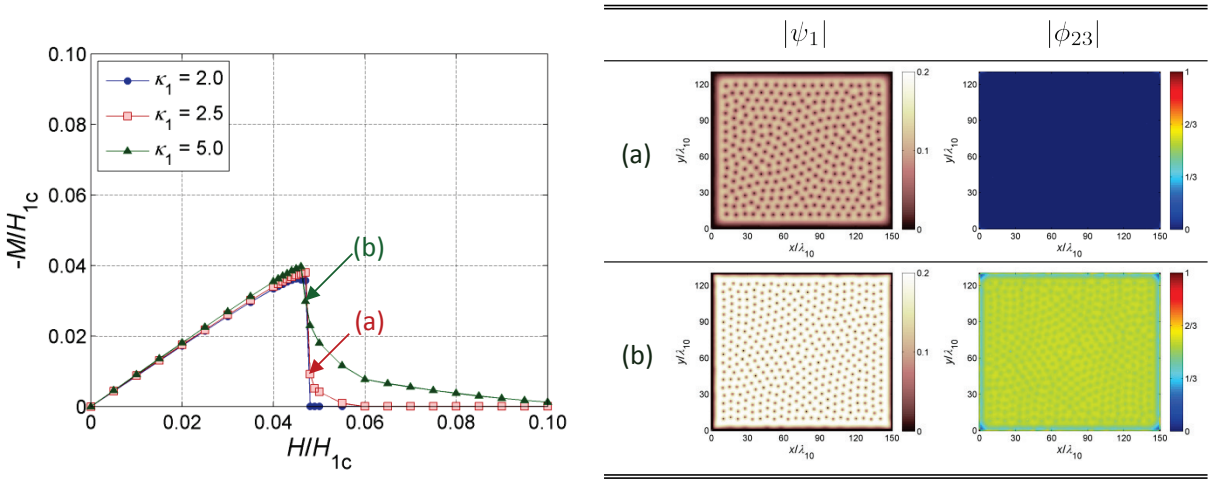

Figure 5.1: (Left panel) Magnetization (M-H) curves of multicomponent superconductors with frustrated intercomponent couplings subject to the SC-FM boundary condition, in comparison with typical material parameters for type-I, type-VC, and type-II with $\kappa_1 = 2.0, 2.5$ and 5.0 with common $r_m = 0.3$, respectively. (Right Panel) (a) and (b) show images of the system at H_{c1} (indicated by arrows in the left panel) representing $|\psi_1|$ and ϕ_{23}.

5.1 M-H Characteristics

SC-FM boundary condition

We begin our discussion of characteristics by looking at M-H curves obtained by applying the SC-FM boundary condition; see left panel in Fig. 5.1. Typical material parameters are used: $r_{\rm m} = 0.3$ and $\kappa_1 = 2.0$, 2.5, and 5.0 corresponding to type-I ($H_{\rm n} < H_{\rm tc}$), type-VC[2] ($H_{\rm n} \gtrsim H_{\rm tc}$), and type-II ($H_{\rm n} \gg H_{\rm tc}$), respectively.

Focusing on each magnetization behavior at H_{c1} where the M-H curves start to drop, we find that the type-VC superconductor shows an abrupt jump in magnetization as in type-I superconductors, but still displays finite diamagnetism.

The small diamagnetism at H_{c1} actually indicates the presence of a typical vortex state associated with a TRSR state, as seen in Fig. 5.1(a), which represents images of $|\psi_1|$ and ϕ_{23} for the system. In this instance, no VC state can be found, and the system transforms completely into a TRSR from the TRSB state.

In contrast, both type-I and type-II superconductors exhibit typical M-H curves, which feature a *magnetization jump* following the phase transition from the superconductivity to normal state, and a *continuous change* associated with conventional vortex penetration. Both behaviors are consistent with the H-T phase diagrams discussed in Chap. 4.

SC-I boundary condition

We next present M-H curves obtained using the S-I boundary condition; see Fig. 5.2. All material parameters are the same as for the previous case.

In a type-VC superconductor, we see no vortex state and superconductivity is almost suppressed. This result can be understood as an enhanced screening because of SC-I boundary effects, and therefore the VC state is overshadowed. The small diamagnetism in the M-H curve stems from slight surface superconductivity at the edge of the simulation box, as seen in the image for $|\psi_1|$ (Fig. 5.2(a)).

An interesting behavior is found even in a type-II superconductor in that the M-H curve exhibits an unexpected magnetization jump at H_{c1}. As seen in Fig. 5.2(b), we find a typical vortex-lattice

[2]For convenience, we call this parameter regime "type-VC".

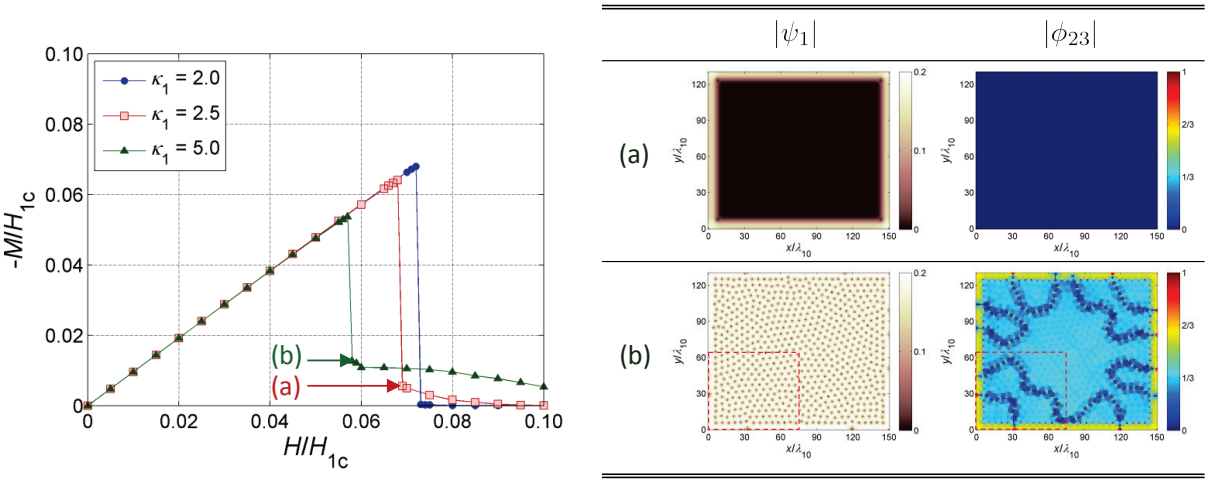

Figure 5.2: Same as for Fig. 5.1 except the SC-I boundary condition is used.

configuration associated with a TRSB state, whereas intercomponent phase differences are suppressed from the bulk value $2\pi/3$ by interior magnetic fields. Note that the cause of a stripe-like structure indicating a TRSR state is discussed in the next section.

5.2 Vortex Penetration Dynamics

To clarify the anomalous behavior in M-H curves at H_{c1}, we next discuss the time-dependence of the vortex states when the magnetic fields are applied to a multicomponent TRSB superconductor.

Collective vortex penetration

Using the SC-FM boundary condition, we have found typical vortex configurations at H_{c1} both in type-VC and type-II superconductors associated with TRSR and TRSB states, respectively. To begin, Fig. 5.3 shows as a reference the time-dependence of the vortex configurations for type-II superconductors at $H = 0.048H_{c1}$. Generally, in a conventional type-II superconductor, vortices penetrate a system diffusively and are distributed forming (locally) a triangular lattice. Such typical vortex penetration dynamics can be observed here.

In contrast, Fig. 5.4 shows the time-dependence of the vortex configurations for type-VC superconductors at the same field. In this instance, we find that the vortex penetration is always associated with domain separation between the TRSB and TRSR states as evident in panel (d) for the intercomponent phase difference ϕ_{23}. As seen in the magnetic flux density B_z, vortices are collectively entering the superconductor but are confined to the TRSR domain, forming a typical vortex-lattice configuration. Such *collective vortex penetration* is considered unique to vortex dynamics in type-VC superconductors.

Fractional vortex penetration

For the M-H curves of type-II superconductors subject to the SC-I boundary condition, we have also found an anomalous behavior at H_{c1} showing abrupt changes in magnetization. When we look closely at the vortex penetration process along the edge of the system, an interesting phenomenon can be seen, namely the creation and annihilation of *fractional vortices*.

Fig. 5.5 shows the evolution of the vortex configurations at certain time-steps for the different order parameters $|\psi_j|$ and phase difference. Each sequence corresponds to an enlarged view of the red box from in Fig. 5.2(b). First, we clearly find that within the system two *chiral* TRSB states appear indexed by the initial vortex entering. The two domains change with time as the vortex configuration

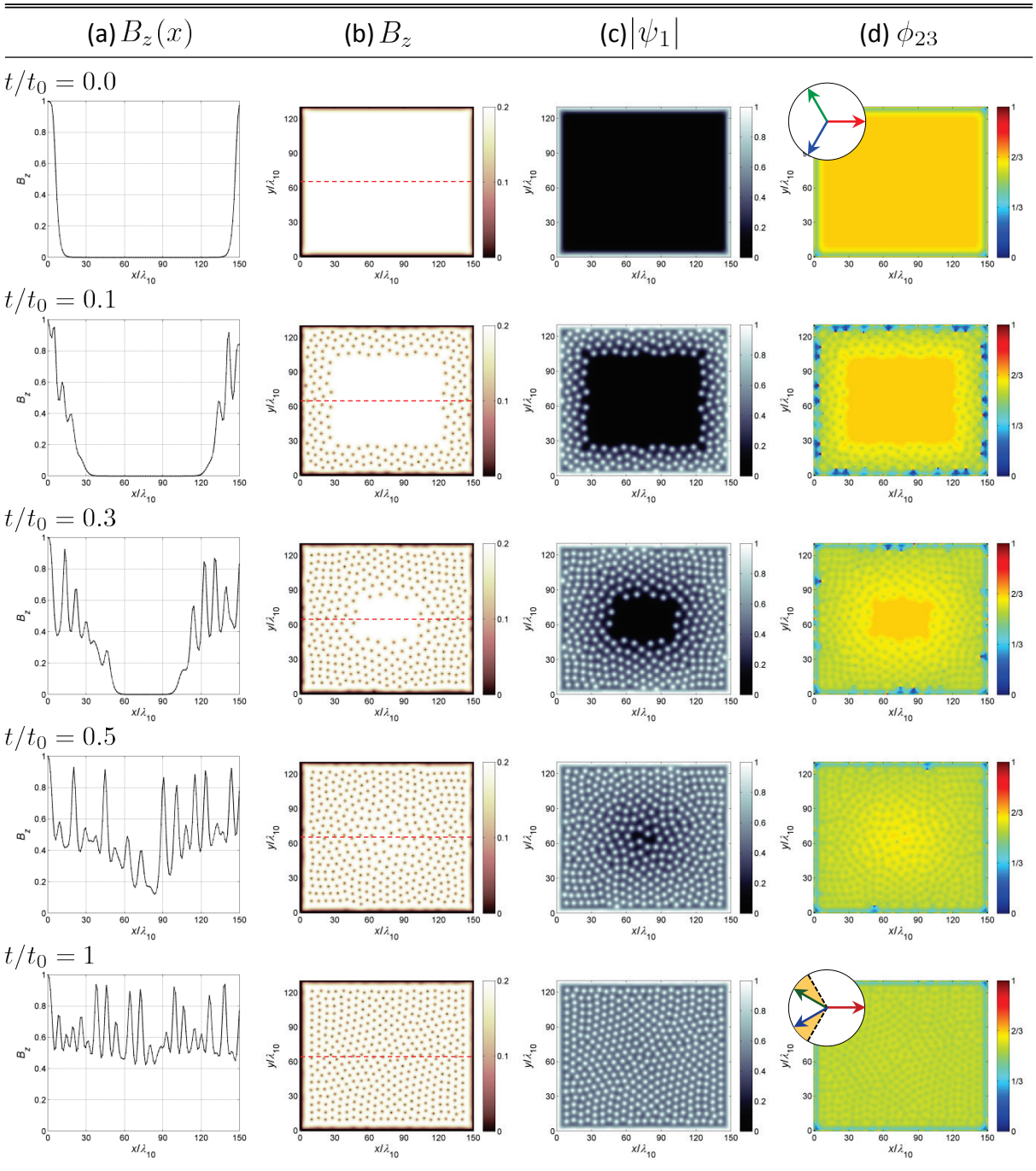

Figure 5.3: Time-dependence of vortex states at H_{c1} in a multicomponent TRSB superconductor (type-II). Material parameters are $r_m = 0.3$ and $\kappa_1 = 5.0$ satisfying the condition $H_n \gg H_{tc}$. (a) Spatial profiles of the magnetic flux density B_z along the red line in the panel (b), system images of (b) B_z, (c) amplitude of the order parameter for the first-component $|\psi_1|$, and (d) intercomponent phase difference ϕ_{23}. Values of magnetic flux density B_z are normalized as $B'_z = B_z/H_{c1}$ (the prime has been dropped). The SC-FM boundary condition is used here, and t_0 is the relaxation time for the equilibrium state.

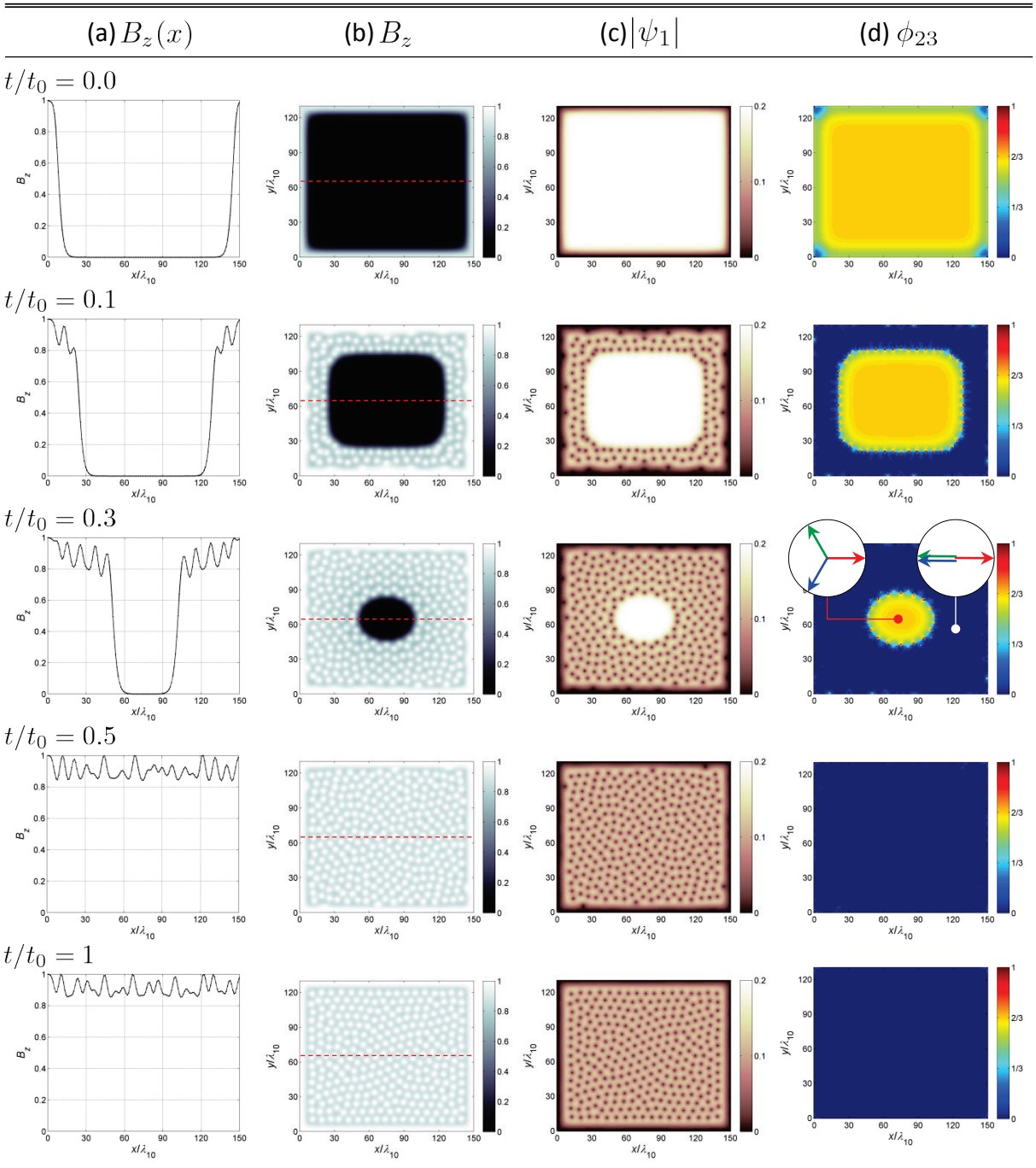

Figure 5.4: Same as for Fig. 5.3 except the material parameters are $r_m = 0.3$ and $\kappa_1 = 2.5$ satisfying $H_{\rm n} \gtrsim H_{\rm tc}$ (type-VC).

evolves. Furthermore, along the chiral domain walls marked by red dashed lines in the images, the vortex cores are dissociated, indicating *fractional vortex*; this dissociation is especially clear near the system edge.

Indeed, the occurrence of fractional vortices was discussed in Ref. [58], focusing on the domain boundaries between the two chiral TRSB states. Also, based on the two-component London theory, the spatial variation of the intercomponent phase ϕ_{jk} allows for a fractional vortex solution at the surface [79]. The origin of the fractional vortices in this simulation is considered as essentially similar to the two-component case. The dissociation of vortex cores in this system is triggered by similar mechanisms. It should be emphasized that the degree of freedom in the intercomponent phases yields entirely novel properties, which also has a close relationship with TRSB.

5.3 Discussion

For the unique material parameters of the type-VC superconductors satisfying the condition ($H_{\rm n} \gtrsim H_{\rm tc}$), we have focused on the anomalous change in magnetization at $H_{\rm c1}$ as depicted in the M-H curves. Strictly speaking, a similar magnetic response can be observed in the so-called low-κ superconductors, where the GL parameter κ is slightly larger than $1/\sqrt{2}$ [80]. In such superconductors, the vortex interaction is small and any vortex configuration is nearly degenerate [76] resulting also in sharp changes in magnetization. Therefore, the experimental identification of the type-VC superconductor will require accurate characterization of magnetic properties.

We find no vortex-clustering when the SC-I boundary condition is imposed. Increasing the applied fields, the system is suppressed almost in a normal state except the surface superconductivity. In view of the experimental observation of the VC state, the screening effect of the superconductors is crucially obstructive, as we have seen the inconsistent results between SC-FM and SC-I boundary conditions. For probing the VC state, one should experience reducing magnetic fields or temperature (i.e. field-cool), where internal vortices are not affected by the screening.

Collective vortex penetration is a remarkable hallmark of TRSB states in multiband superconductors. Time-dependent imaging (e.g. Lorentz microscopy) of the magnetic-flux density will provide a powerful means to observe this phenomenon. As the parameters for the time-scale are arbitrary in the present calculation, further improvements are required to simulate experimental situations.

5.4 Summary

By means of the TDGL method subject to the finite boundary conditions, we have analyzed M-H curves and vortex penetration dynamics at the lower critical field $H_{\rm c1}$ in multicomponent superconductors with frustrated intercomponent couplings. In the unique parameter regime where the thermodynamic critical field and nucleation field satisfy the condition $H_{\rm n} \gtrsim H_{\rm tc}$, we have identified anomalous magnetic behaviors at $H_{\rm c1}$ where abrupt magnetization changes occur associated with a phase transition between the TRSB and TRSR states. Novel vortex penetration dynamics, namely *collective vortex penetration*, is expected to be explored with a view to reduce surface screening. Even in the parameter regime for type-II superconductivity ($H_{\rm n} \gg H_{\rm tc}$), anomalous vortex penetration is expected following the occurrence of fractional vortices at the surfaces of samples. The range of characteristics shown should be given particular attention as a means to probe TRSB in multiband superconductors with $s_{\pm}$ symmetry.

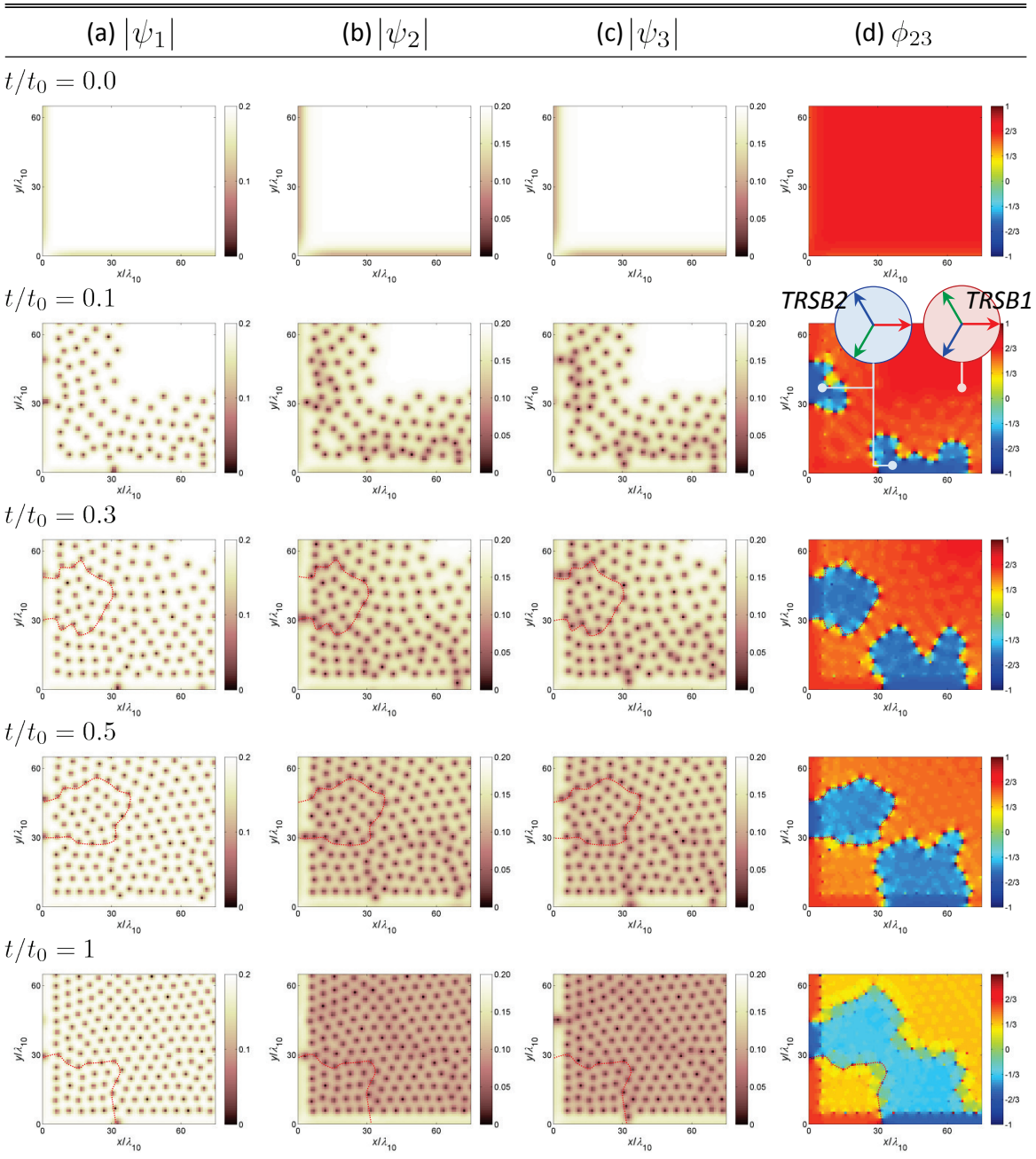

Figure 5.5: Time-dependence of vortex configurations at the system boundary. The images, showing an enlarged view of the enclosed area indicated in Fig. 5.2(b), represent the amplitude of the order parameters $|\psi_j|$ and the intercomponent phase difference $\phi_{23} = \phi_3 - \phi_2$. The range of ϕ_{23} is changed here to $-\pi \leq \phi_{23} \leq +\pi$ to emphasize the two chiral TRSB states.

Chapter 6

Probing Commensurate Ground States of Josephson Vortex in Layered Superconductors

Up to the previous chapter, we have discussed novel vortex states in which the multibandness plays an important role, and found essentially different vortex structure where multiple divergent coherence lengths exist as a consequence of time-reversal symmetry breaking. Regarding unconventionality of vortex structure, as a matter of fact, various studies have been undertaken for long time triggered by emergence of new superconductivity mechanisms. Among them, intensive efforts might have been devoted to copper-oxide (cuprate) high temperature superconductors (HTSCs) motivated not only by their extremely high critical temperatures T_c, but also by manifold vortex states and phase transitions originated their common features of dimensionality and thermal fluctuation.

In this chapter, we briefly review the vortex states in cuprate HTSCs and discuss interesting dynamics of interlayer vortices, which are governed by intrinsic vortex structure and commensurability between vortex lattice constants and two-dimensional layered structure.

This chapter is reproduced with permission from; Y. Takahashi, M.-B. Luo, T. Nishizaki, N. Kobayashi and X. Hu, *J. Nanosci. Nanotechnol.* **14**, 2859 (2014).

6.1 Backgrounds

As introduced in Chap. 1, a general H-T phase diagram in conventional type-II superconductors consists essentially of the Meissner and vortex states. However, discovery of cuprate HTSCs has totally renewed such a basic picture, and sparked further interests on vortex states. It was sooner understood that the mean-field theory of vortex states is not applicable any more for the cuprate HTSCs due to their intrinsic features;

1. Strong two-dimensionality: Crystalline structure of cuprate HTSCs possesses two-dimensional (2D) superconductivity planes (CuO_2 planes) and insulator layers, which are periodically stacked in a nano-scale along the c-axis (perpendicular to CuO_2 planes).

2. Strong thermal fluctuations: Thermal fluctuations dominate the vortex states in a wide temperature region due to high critical temperature.

For example, such these features can be seen in resistivity measurements. When magnetic fields are applied perpendicular to CuO_2 layers, resistivity starts to drop gradually with decrease of temperature at a certain point which correspond to the upper crirtical field $H_{c2}(T)$, but remains finite values until the melting transition temperature T_m where the resistivity becomes completely zero. This is caused

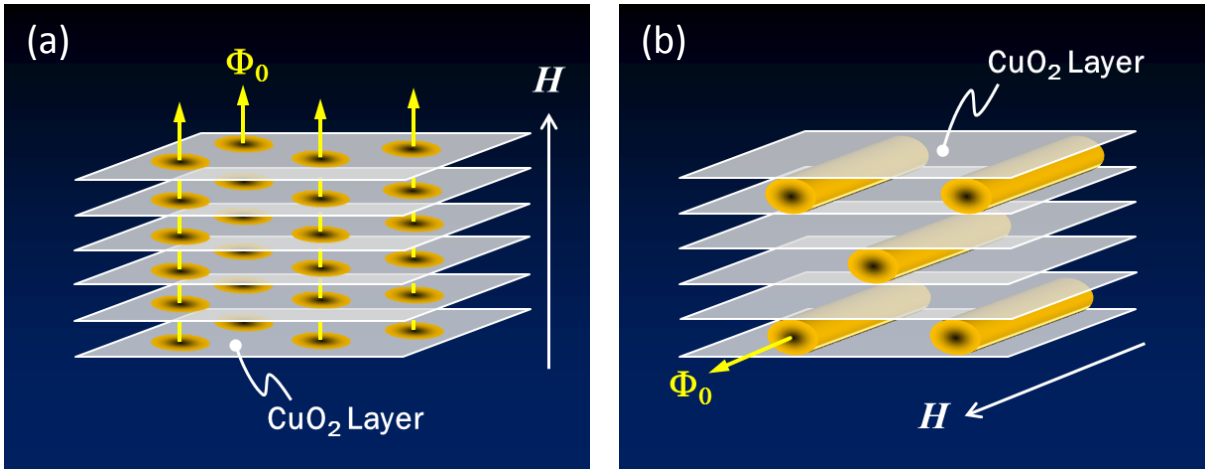

Figure 6.1: Schematics of vortex states in cuprate superconductors. (a) Vortex state in perpendicular magnetic fields to CuO_2 planes (pancake vortices). (b) Vortex state in parallel magnetic fields to CuO_2 planes (Josephson vortices).

by the strong two-dimensionality and superconductivity fluctuation due to extremely small coherence length in the cuprate system.[1]

Cuprate HTSCs are extremely type-II superconductors since the coherence length ξ is small, typically in the order of 10 nm, whereas the penetration depth λ is contrastively large, typically in the order of 1000 nm, in *ab*-plane for instance. Therefore, it is remarked that vortices in cuprate HTSCs are essentially nano-scale objects, and that competition between the comparable vortex-core size and interlayer separation may generate unconventional effects in macroscopic observables. On the other hand, nano-scale manipulations of vortices are required in view of future applications of cuprate HTSCs.

When the magnetic field is applied perpendicular to the CuO_2 planes, vortex cores of the normal state appear in the superconducting planes. As seen in Fig. 6.1(a), the vortex currents are confined within CuO_2 planes and form suppressed vortex structure with the core size typically of the coherence length ξ_{ab} along the CuO_2 plane and ξ_c along the *c*-axis. Such a vortex is called a *pancake vortex*, and the thermodynamic properties of the pancake-vortex state have been investigated soon after the discovery of cuprates HTSC. The pancake vortices in each CuO_2 planes store magnetic flux lines coupled *weakly* each other via interlayer Josephson effect, and the vortex lines behave as elastic objects. Nowadays, it is well established that the vortices in cuprate HTSC take various states. Unique phase transitions such as first-order vortex-lattice melting and continuous vortex-glass transition induced by point-like defects are well understood by now [81, 82, 83, 84, 85]. Furthermore, the variety of vortex states provided an interesting playground familiar as *vortex matter* for a good model of thermodynamic physics. Figure 6.2 shows a typical *H*-*T* phase diagram established in $YBa_2Cu_3O_y$ (YBCO) [86].

When the magnetic field is applied parallel to the CuO_2 planes, the layered structure gives birth to more interesting vortex states. It is considered that the periodic layered structure provides a stack of intrinsic Josephson junctions (IJJs) where the superconductivity planes are separated by the insulator layers and coupled by the Josephson effect [87]. The magnetic fluxes are localized in the insulator layers between the superconductivity planes to save the energy costs. Such localization of interlayer vortices is known as the *intrinsic pinning effect* [88]. The interlayer vortex is called as *Josephson vortex* (JV) as shown in Fig. 6.1(b).

[1]The strength of thermal fluctuation in cuprate HTSCs is obvious by the Ginzburg number $G_i \equiv 16\pi^3\kappa^4\gamma(k_BT_c)^2/\Phi_0^3H_{c2}(0)$ approximated as $\sim 10^{-2}$, in contrast to conventional superconductors such as Nb ($T_c \sim 9.3$ K, $G_i \sim 10^{-10}$) and $NbSe_2$ ($T_c \sim 7.2$ K, $G_i \sim 10^{-4}$).

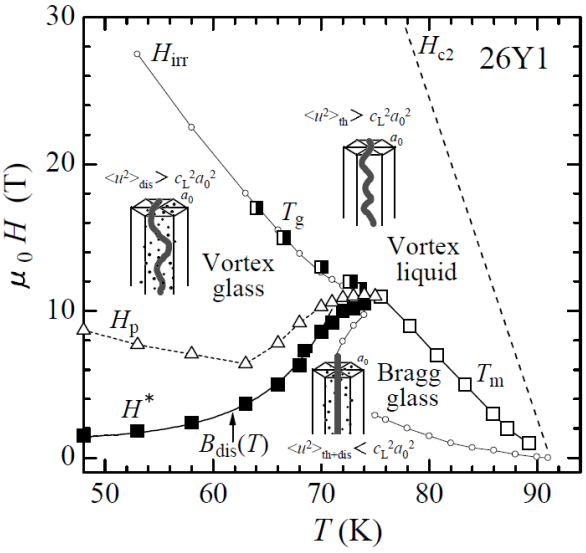

Figure 6.2: Vortex-matter phase diagram in untwinned $YBa_2Cu_3O_y$ [86]. © 2000 IOP Publishing. Reproduced by permission of IOP Publishing. All rights reserved.

The thermodynamic properties of interlayer JVs have been attracting significant interests [89, 90], and novel vortex states including vortex smectic [91, 92] and Kosterlitz-Thouless phase [93] have been proposed theoretically so far. The phase diagram of JV states has also been investigated experimentally [94, 95, 96, 97, 98, 99]. To determine the phase boundary between liquid and lattice phase of JVs, drops in in-plane (ab) resistivity upon temperature decrease were used. Interestingly, the phase boundary (melting line) exhibited remarkable oscillatory which was understood to be caused by the commensuration of JV lattice with the layered structure [94, 95, 99]. In the present work, I probe deeply into the JV-lattice phase by the flow dynamics, and try to derive better understanding on the ground-state JV lattice as the function of magnetic fields.

In the ground state of a JV system, the vortex-lattice constant along the c-axis should be Ns, with N an integer and s the separation between neighboring CuO_2 layers, due to the intrinsic pinning effect, in sharp contrast to the Abrikosov vortex-lattice for which the vortex-lattice constant is determined purely by the strength of magnetic fields and can be continuous. Figure 6.3(a) shows typical JV lattice configurations which satisfy the commensurability condition [92, 100], where the horizontal lines correspond to superconductivity layers (CuO_2) and the length is rescaled by the anisotropy parameter γ ($x \to x/\gamma$). The magnetic fields for the two standard JV lattices, where one of the main axes is either parallel or perpendicular to the CuO_2 layers, are given by

$$\begin{aligned} \text{A-lattice: } B &= \frac{\sqrt{3}\Phi_0}{2\gamma(Ns)^2}, \\ \text{B-lattice: } B &= \frac{\Phi_0}{2\sqrt{3}\gamma(Ns)^2}, \end{aligned} \tag{6.1}$$

where Φ_0 is the magnetic flux quantum.

In addition to the above two JV lattice orientations, rotational JV lattices have also been proposed [100, 101], which are characterized by a unit vector $\mathbf{r} = m\mathbf{e_1} + n\mathbf{e_2}$ as shown in Fig. 6.3(b), where $\mathbf{r}$ denotes the vector between nearest-neighbor vortices in the same layer, and $\mathbf{e_1}$ and $\mathbf{e_2}$ are unit vectors of the triangular vortex lattice. Based on this definition, the corresponding magnetic field is given by

$$\text{R-lattice: } B = \frac{\sqrt{3}}{2}\frac{\phi_0}{N^2(n^2+nm+m^2)\gamma s^2}. \tag{6.2}$$

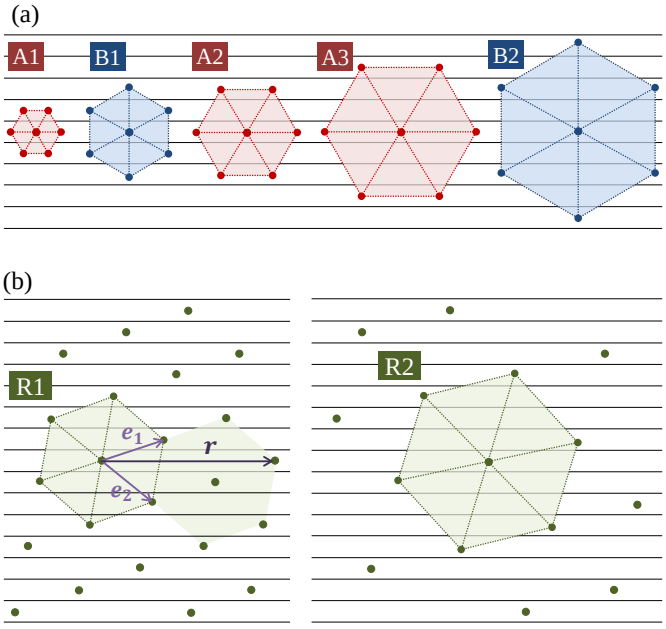

Figure 6.3: Josephson vortex (JV) lattices satisfying the commensurability condition. The x-axis is rescaled by the anisotropy parameter γ. Solid horizontal lines (black) correspond to the CuO_2 planes. (a) A-type and B-type JV lattices in order of magnetic field strength. (b) Rotational JV lattices: R1-lattice is defined with the commensurability condition $(n, m, N) = (2, 1, 1)$, and R2-lattice with $(n, m, N) = (3, 1, 1)$.

In the present work, we try to illuminate the flux-flow dynamics of the A-, B- and R-lattices. First, the flux-flow resistivity of JVs under various magnetic fields is simulated in terms of Langevin dynamics. The oscillatory behavior of resistivity upon the magnetic field is then related to the commensurate JV lattices. Next, experimental results for bulk single crystals of under-doped YBCO are presented, where an oscillation in the resistivity with magnetic field has also been observed. Finally we compare the both results by simulations and experiments and give a conclusion.

6.2 Theoretical Approach

6.2.1 Model and simulation details

We consider a superconductor of layered structure with applied magnetic field parallel to the layers. The model system is a stack of superconductivity planes of thickness d and period s, as shown schematically in Fig. 6.4. In the Langevin dynamics at zero temperature, the overdamped equation of motion for the i-th JV at position $\vec{r}_i$ is described

$$\eta \frac{d\vec{r}_i}{dt} = \sum_{j \neq i}^{N_\mathrm{v}} \vec{F}^{\mathrm{vv}}(\vec{r}_i - \vec{r}_j) + \sum_{k=1}^{N_\mathrm{p}} \vec{F}^{\mathrm{vp}}(\vec{r}_i - \vec{R}_k) + \vec{F}_{\mathrm{lp}} + \vec{F}_{\mathrm{L}}, \tag{6.3}$$

where η is the viscosity coefficient, N_v and N_p are the total number of JVs and point-like pins, respectively; JVs feel the following forces: F^{vv} JV-JV repulsion, F^{vp} attractive interaction between

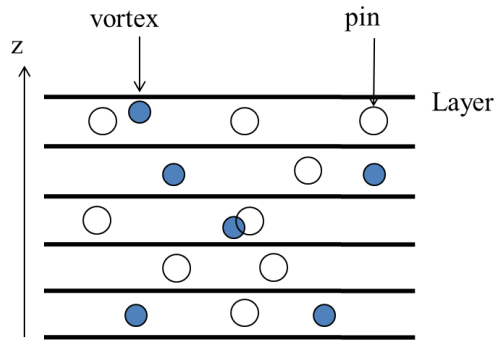

Figure 6.4: Schematic picture of simulation model.

JV and point-like pinning center, $F^{\rm lp}$ pinning potential by periodic layered structure,

$$\begin{aligned}
\vec{F}^{\rm vv}(\vec{r_{ij}}) &= \frac{\epsilon_0}{\lambda_{ab}} K_1(r_{ij}/\lambda_{ab})\hat{r}_{ij}, \\
\vec{F}^{\rm vp}(\vec{r_{i\rm p}}) &= -A_{\rm p}\epsilon_0 \frac{2r_{i\rm p}}{R_{\rm p}^2}\Theta(r_{i\rm p}-R_{\rm p})\hat{r}_{i\rm p}, \\
\vec{F}_{\rm lp}(r_{i\rm p}) &= F_{\rm lp}^0 \sin(2\pi z/s)\hat{z},
\end{aligned} \tag{6.4}$$

and the in-plane uniform Lorentz force F_L.

The parameters are given as follows: the penetration depth in ab plane $\lambda_{ab} = 2000$ Å, interlayer distance $s = 12$ Å and the anisotropy parameter $\gamma = 36$, corresponding to under-doped YBCO, pin density of $0.8/\lambda^2$, pin size of $R_{\rm p} = 0.38s$, strengths of point pinning of $A_{\rm p} = 0.05$ and layer pinning of $F_{\rm lp}^0 = 1.0$. The units for length, energy, temperature, force and time are taken as λ_{ab}, ϵ_0, ϵ_0/k_B, ϵ_0/λ_{ab} and $\eta\lambda_{ab}^2/\epsilon_0$. The resistivity in our simulation is calculated in connection with flux-flow velocity v as $\rho = E/J = vB\Phi_0/F$, where the relations $E = vB$ and $F = J\Phi_0$ have been used. In dimensionless form, the resistivity in the system size S is simply given by $\rho = vN_{\rm v}/FS$.

6.2.2 Field dependence of resistivity

Figure 6.5 displays the magnetic-field dependence of resistivity caused by the JV flow for several typical driving forces $F = 0.034$, 0.040, 0.042, and 0.046. An oscillation of resistivity upon magnetic field sweeping is clearly observed. As the values of the magnetic fields corresponding to the typical vortex structures are indicated (see Eq. (6.1)), one can see that the peaks in resistivity occur roughly at the magnetic fields corresponding to the commensurate JV lattices.

I have also paid attention to the driving-force dependence of modes in flux-flow dynamics, with typical vortex configurations and the statistics of vortex velocity shown in Fig. 6.6. Figure 6.6(a) is for JV flow state under a relatively large driving force $F = 0.046$. For A2-lattice, many JVs are pinned and dislocations are generated which suppress coherent motions of JVs. On the other hand, dislocations are rare for R1-lattice, and JVs move coherently at this driving force. This property of R1-lattice can be understood as a consequence of the fact that the Burgers vector is not parallel to layers [102].

Figure 6.6(b) is for a relatively small driving force $F = 0.034$. In this case, dislocations permit creep motions for A2-lattice, whereas R1-lattice is totally pinned. As a result, resistivity of R1-lattice can be smaller than A2-lattice one at weak driving force as seen in Fig. 6.5.

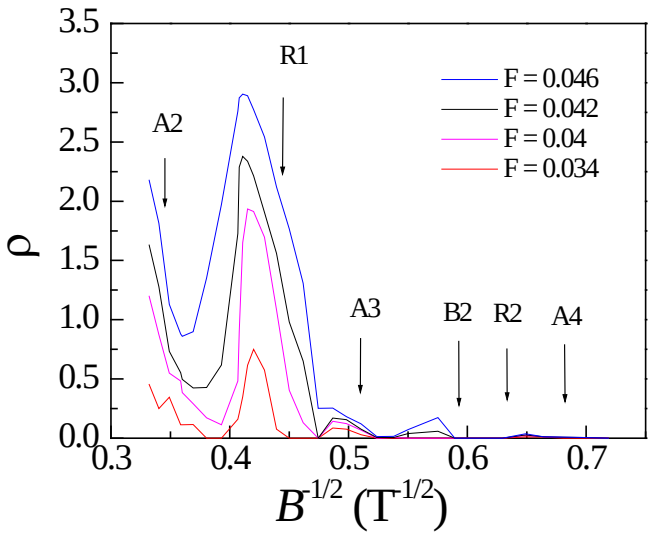

Figure 6.5: Magnetic field dependence of flux-flow resistivity simulated by the Langevin dynamics at $T = 0$. Characteristic magnetic fields calculated from the commensurability conditions are indicated with arrows.

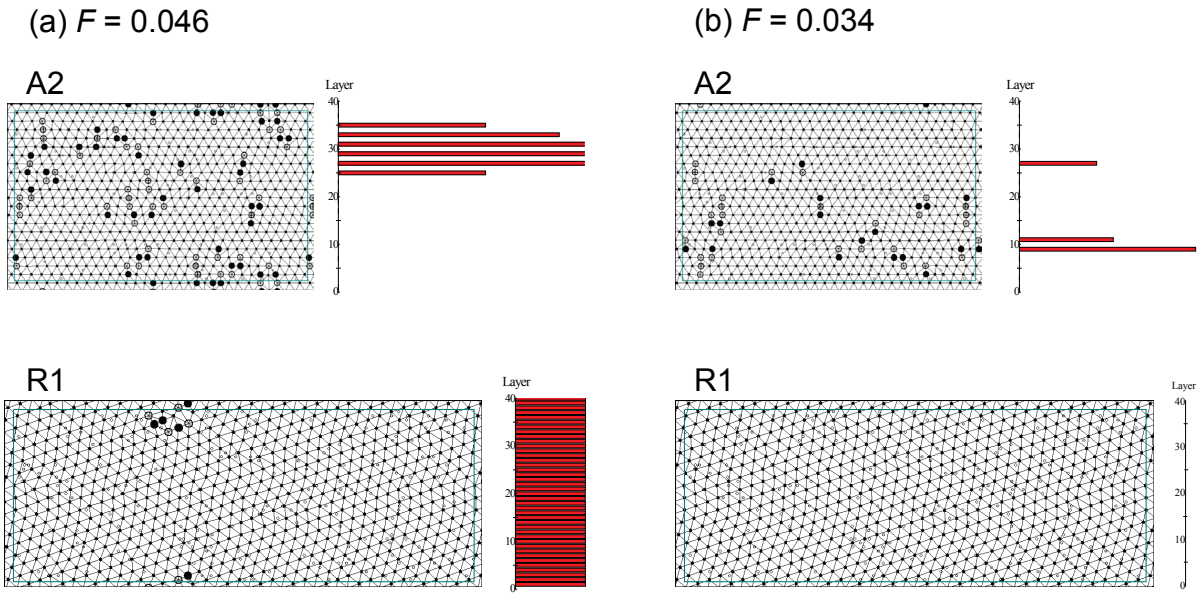

Figure 6.6: Typical configurations of Josephson vortices (JVs) for (a) $F = 0.046$ and (b) $F = 0.034$, with charts at righthand side for the distributions of flow velocities at different layers.

6.3 Experimental Approach

6.3.1 Experimental setup

Resistivity due to the JV flow has been investigated in single crystals of $YBa_2Cu_3O_y$ (YBCO). As the anisotropy parameter for optimum doped YBCO is comparably small as $\gamma \simeq 8$, JV lattices with small lattice constant cannot not be reached experimentally, since A2-lattice, for example, corresponds to $H \approx 40$ T (see Eqs. (1) and (2)). To overcome this difficulty, I synthesized high-quality single crystals of underdoped YBCO with sufficiently large anisotropy parameter $\gamma \simeq 50$, which makes it possible to investigate the flux-flow resistivity in JV lattices with small lattice constants under experimentally accessible magnetic fields [99].

High quality single-crystals of YBCO were grown by a self-flux method using a Y_2O_3 crucible [86]. The oxygen content y was controlled by the annealing condition under 1 bar nitrogen at 475°C for 5 days [99]. Underdoped YBCO was successfully obtained with critical temperature $T_c \simeq 30$. The anisotropy parameter of this sample is estimated as $\gamma \simeq 50$ using the empirical relation between the critical temperature T_c and the anisotropy parameter [103, 104, 105].

Because of the orthorhombic crystalline structure of YBCO, single crystals possess twin boundaries which work as pinning potentials. In order to avoid this undesirable effect, I extracted untwinned domains by cutting off the twin boundaries. Electric resistivity along the c-axis $\rho_c(T, H)$ was measured by a conventional dc four-probe method with current density $J \geqq 5$ (A/cm^2). Magnetic field direction is fine-tuned parallel to the layers $H \parallel ab$ ($\theta = 0°$) by the two-axial rotational sample holder. The following results are all obtained with high alignment precision of $\Delta\theta < 0.05°$.

6.3.2 Experimental results

Figure 6.7 shows the temperature dependence of c-axis resistivity $\rho_c(T)$. The inset is for resistivity in a wide field range of magnetic fields ($0 \leqq \mu_0 H \leqq 15$ T). At the higher magnetic field $\mu_0 H > 5$ T, the resistivity drops to zero monotonically upon temperature decrease. However, the resistivity at $\mu_0 H = 1$ T shows anomalous behavior that the resistivity once decreases until a characteristic temperature T_1, but increases up to another characteristic temperature T_2, then finally decreases again to zero. Similar behaviors are observed at several magnetic fields in the regime $0 < \mu_0 H < 5$ T. However, at $\mu_0 H = 0.1$ and 2 T, a conventional monotonic behaviors are seen.

The magnetic field dependence of c-axis resistivity $\rho_c(H)$ has been measured in detail between the two characteristic temperatures T_1 and T_2. Figure 6.8 shows $\rho_c(H)$ at $T = 24$ K. As seen in the inset, the resistivity oscillates clearly against the applied magnetic field H. In order to illuminate the relation between the resistivity oscillation and the JV lattice commensurability condition, the resistivity with respect to $B^{-1/2}$ is replotted as shown in the main panel of Fig. 6.8. It becomes clear that the peak positions of resistivity locate at the magnetic fields associated with the A-lattices given in Eq. (6.1), with the anisotropy parameter $\gamma = 50$ when the interlayer distance $s = 11.7$ nm and flux quantum $\Phi_0 = 2.068 \times 10^{-15}$ Wb are taken into account. It is remarked that this anisotropy parameter γ agrees perfectly with the estimation from the critical temperature T_c of this sample as discussed above. The peak positions remain unchanged for current densities $J = 5, 7.5$ and 10 A/cm^2. When the current density is much higher ($J > 30$ A/cm^2), the oscillatory behavior disappears.

In addition to the peaks of A-lattice with large lattice constants, we observe two resistivity peaks associated with R1-lattice and B2-lattice. To the best of our knowledge, this is the first experimental result which signatures the existence of the nontrivial R1-lattice.

6.4 Discussions

Several comments should be made as follows. First, while many peaks in resistivity are observed in experiments with high precision, the present simulation fails to see peaks with large lattice constants

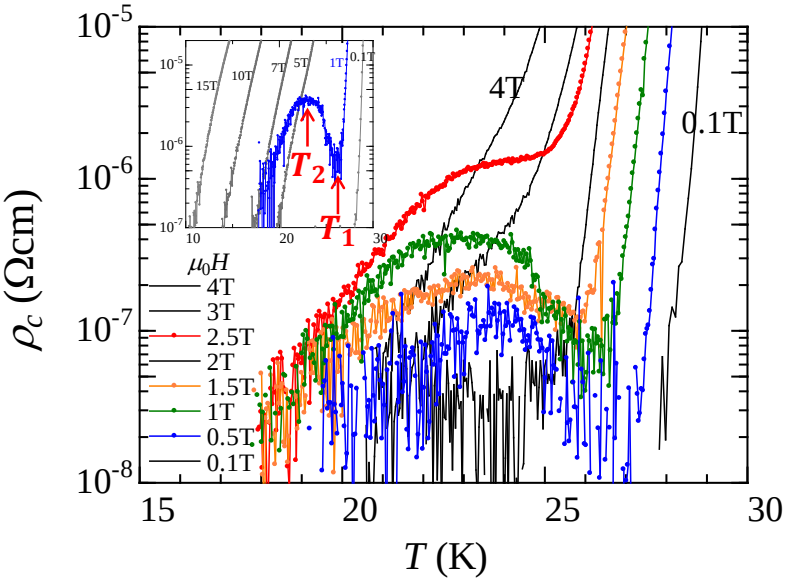

Figure 6.7: Temperature dependence of c-axis resistivity for magnetic fields $\mu_0 H \leq 5$ T. Inset: resistivity in the wide range of magnetic fields $0 \leq \mu_0 H \leq 15$ T. The arrows indicate the characteristic temperatures T_1 and T_2 between which anomalous behaviors in resistivity are observed.

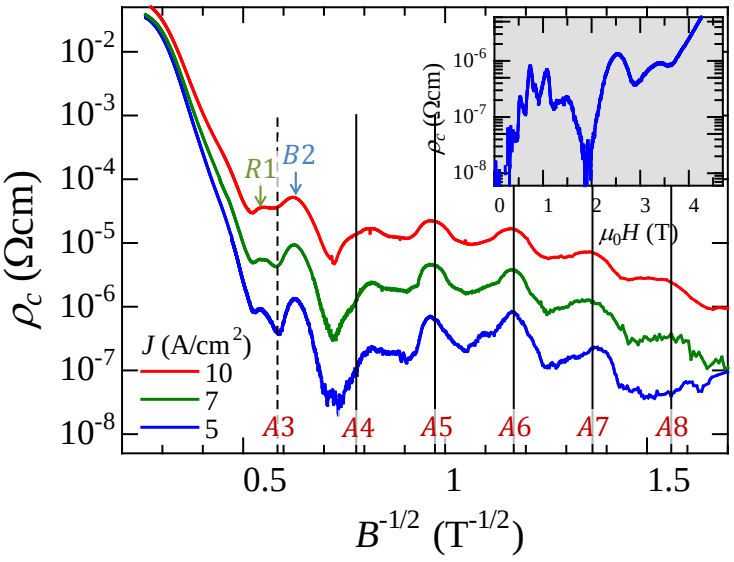

Figure 6.8: c-axis resistivity versus rescaled magnetic field $B^{-1/2}$ for current densities $J = 5.0, 7.0, 10.0$ A/cm^2 at $T = 24.0$ K. Inset: c-axis resistivity versus magnetic field in linear scale for $J = 5.0$ A/cm^2.

and thus needs further improvement. Secondly, as seen in Fig. 6.8, the A3-lattice yields a resistivity dip instead of a peak, in contrast to other A-lattices with higher indices. For the second point, it is noticed that dependence of the resistivity on the strength of driving force varies with the lattice configuration, as shown in Fig. 6.6. It may also be caused by the so-called *smectic* phase in between the JV crystal and liquid at high magnetic fields [92], which should modify the flux-flow dynamics. All these points should be addressed in future works.

6.5 Summary

To summarize, we have investigated flow dynamics of Josephson vortices in cuprate superconductors, both theoretically and experimentally. Our simulation based on the Langevin dynamics has revealed oscillatory behaviors in the Josephson vortex flow resistivity associated with the commensurability condition between vortex lattice and the layered structure. An oscillatory resistivity has also been observed in high-quality single crystals of underdoped $YBa_2Cu_3O_y$ with large anisotropy parameter. From the theoretical and experimental results, a nontrivial Josephson-vortex lattice has been figured out for the first time.

Chapter 7

Conclusion and Outlook

In this thesis I have studied novel vortex states in recent unconventional superconductors where *multibandness* or *dimensionality* produces nontrivial magnetic properties of superconductivity.

In terms of "multibandness", I have reviewed the BCS and GL theories with the view to investigate multiband superconductivity, and illuminated an exotic superconductivity state, namely the TRSB state induced by frustrated interband couplings. Although various unique properties in multiband TRSB superconductivity were revealed through intensive theoretical work, magnetic properties such as the vortex states had not been well studied. Motivated by the preceding analytic study on the TRSB state based on multicomponent GL theory, I have the explored the magnetic properties of multicomponent TRSB superconductivity employing a TDGL method extended to the multicomponent system to treat the magnetic response of superconductors where amplitudes and phases of the order parameters are spatially intertwined. The principal conclusions are summarized as follows:

- I have analyzed single vortex structures in multicomponent TRSB superconductors, and identified multiple divergent length scales, namely 1) recovery lengths for each order parameter, 2) spatial modulations of intercomponent phases, and 3) the magnetic-field penetration depth. This multiplicity of length scales originates with the degrees of freedom in the intercomponent phases, which is intrinsic to multicomponent systems. When the intercomponent phases are exceptionally locked, the problem is simply reduced to single-component case.

- With systematic calculations of the vortex interaction in multicomponent TRSB superconductors, H-T phase diagrams are constructed classifying these superconductors into three categories based on the thermodynamics field $H_{\rm tc}$ and nucleation field $H_{\rm n}$: type-I ($H_{\rm n} < H_{\rm tc}$), *type-VC* ($H_{\rm n} \gtrsim H_{\rm tc}$), and type-II ($H_{\rm n} \gg H_{\rm tc}$). When the material-dependent parameters satisfy the condition $H_{\rm n} \gtrsim H_{\rm tc}$, a novel vortex state appears where multiple vortices form a cluster associated with the domain separation between the TRSB and TRSR states. Whereas the boundary between type-I and type-VC is given by the two characteristic fields, the boundary between type-VC and type-II is given by a sign change in the interface energy Γ for multicomponent TRSB superconductivity. The two criteria $H_{\rm n} = H_{\rm tc}$ and $\Gamma = 0$ do not coincide in multicomponent TRSB superconductivity.

- I have used the TDGL method to model magnetization (M-H) curves for multicomponent TRSB superconductors and highlighted vortex penetration dynamics at the lower critical field $H_{\rm c1}$. For type-VC, M-H curves show anomalous behavior where vortices start to penetrate a superconductor collectively induced by the domain separation of TRSB and TRSR. This is a consequence of the unique VC state above the $H_{\rm c1}$ seen in the H-T phase diagram. For type-II, the M-H curves still show anomalous behavior at $H_{\rm c1}$. Here, the creation and annihilation of fractional vortices occur at the sample edge caused by intercomponent phase modulation.

Both anomalous behaviors at H_{c1} are expected to be a probe of the TRSB state in multiband superconductors.

In terms of "dimensionality", I have focused on interlayer vortices known as Josephson vortices (JVs) in high-T_c cuprate superconductors. When external fields are applied parallel to the layers, magnetic fluxes are confined between the superconducting layers and localized by the interlayer Josephson effect. The JV ground states can be identified by their oscillatory resistivity resulting from the JV dynamics governed by commensuration between the periodicity of the superconductivity layers and JV lattice constants. Motivated by the experimental result observing the unexpected oscillatory resistivity from the JV dynamics in a cuprate superconductor ($YBa_2Cu_3O_y$) with anisotropy parameter $\gamma \sim 50$, I have analyzed the novel JV dynamics based on a Langevin dynamics scheme for JV dynamics. The principal finding is:

- I have identified a nontrivial flow mode for the *rotational* JV lattice in addition to trivial flow modes for the parallel and perpendicular JV lattices.

At the time of writing, a TRSB state in multiband superconductors has note been experimentally observed. Possible candidates are the Fe-based superconductors with $s_\pm$ pairing because of their multibandness with more than three superconductivity condensates and the existence of repulsive interband couplings. Future efforts to explore the exotic superconductivity are intently desired. Because magnetic properties are generally one of the more fundamental features measured experimentally, the above conclusions on the magnetic properties in multicomponent TRSB superconductors are expected to be a useful and convenient indication of exotic superconductivity in addition to the other smoking-gun evidence provided by other related work.

It is interesting to see layered crystalline structures as beeing significant in superconductors, even in Fe-based superconductors, which draws in the work on interlayer JVs in this thesis. Recently, a JV state was experimentally identified in an Fe-based superconductor despite a comparably smaller anisotropy parameter $\gamma \sim 4 - 6$ [106]. Because JVs are localized by the interlayer Josephson effect, the multiband effect on JV states are entirely nontrivial with competition between interlayer and interband couplings.

Appendix A

Time-Dependent Ginzburg-Landau Method

The time-dependent Ginzburg-Landau (TDGL) method is generally used to simulate the phenomenological magnetic response of superconductors as performed in the early studies of thin films such as nucleation [107, 108], magnetization [109], and $I-V$ characteristics [110]. Furthermore, the TDGL method has been used recently to simulate vortex states in mesoscopic systems to study geometric effects triggered by experimental developments in micro-fabrication techniques [78, 111, 112, 113, 114].

This appendix is devoted to explain the computational details of the TDGL method for multicomponent superconductors that has been used in this thesis.

A.1 TDGL Equations

The TDGL equations govern the dynamics of the superconductivity order parameter $\psi(\mathbf{r},t)$ and the electromagnetic vector potential $\mathbf{A}(\mathbf{r},t)$. The conventional TDGL equations for a single-component superconductor [115] is extended to multicomponent form by introducing a component index j as in the approach used for the two-component case [116],

$$\frac{\hbar^2}{2m_iD_i}\left(\frac{\partial}{\partial t}+i\frac{2e}{\hbar}\Phi\right)\psi_j=-\frac{\delta f}{\delta\psi_j^*}, \tag{A.1}$$

$$\frac{\sigma}{c}\left(\frac{1}{c}\frac{\partial\mathbf{A}}{\partial t}+\nabla\Phi\right)=-\frac{\delta f}{\delta\mathbf{A}}, \tag{A.2}$$

with D_j the diffusion constant, σ the normal conductivity, Φ the electric potential, and f the multicomponent GL free-energy density functional in Eq. (1.91). By choosing an appropriate gauge, we take $\Phi=0$ and for simplicity ignore details of the dynamic relaxation process. Here, time is in units of $\tau_1=\xi_1^2/D_1$ and the normal conductivity σ is in units of $c^2\tau_1/4\pi\lambda_1^2$.

A.2 Dimensionless Forms

For calculational convenience, we introduce dimensionless quantities. Length scales are based on those for the first-component of individual single-component case (i.e. $\gamma=0$) at $T=0$; the coherence length $\xi_{10}=\sqrt{\hbar^2/2m_1|\alpha_{10}|}$ and the penetration depth $\lambda_{10}=\sqrt{m_1c^2\beta_1/8\pi|\alpha_{10}|e^2}$ with definition $\alpha_{10}\equiv\alpha_1(T)|_{T=0}$. The dimensionless quantities are defined as,

$$x=\lambda_{10}x',\quad \psi_j=\psi_{10}\psi_j',\quad \gamma_{jk}=|\alpha_{10}|\gamma_{jk}',$$
$$f=\frac{H_{1c}^2}{4\pi}f',\quad \mathbf{A}=\lambda_{10}H_{1c}\sqrt{2}\mathbf{A}',\quad \mathbf{B}=H_{1c}\sqrt{2}\mathbf{B}',\quad \mathbf{J}=\frac{2e\hbar\psi_{10}^2}{m_1\xi_{10}}\mathbf{J}', \tag{A.3}$$

where $|\psi_{10}|^2 = |\alpha_{10}|/\beta_1$ and $H_{1c} = \sqrt{4\pi|\alpha_{10}|\psi_{10}^2}$ are the bulk OP and thermodynamic critical field of the individual first-component at $T = 0$, respectively. $\mathbf{B}$, $\mathbf{A}$, and $\mathbf{J}$ are the magnetic induction, the vector potential and the supercurrents, respectively. Based on these dimensionless quantities, the multicomponent GL free-energy density functional in Eq. (1.91) is rewritten by dropping the prime,

$$f = \sum_j \left[\frac{\alpha_{j0}}{\alpha_{10}} \epsilon_j |\psi_j|^2 + \frac{\beta_j}{2\beta_1} |\psi_j|^4 + \frac{m_1}{m_j} \left| \left(\frac{\nabla}{i\kappa_1} - \mathbf{A} \right) \psi_j \right|^2 \right] - \sum_{j<k} \gamma_{j,k} (\psi_j \psi_k^* + \text{c.c.}) + (\nabla \times \mathbf{A})^2, \quad \text{(A.4)}$$

with a material-dependent parameter for the first-component $\kappa_1 = \lambda_{10}/\xi_{10} = (m_1 c/2e\hbar)\sqrt{\beta_1/2\pi}$, and temperature terms $\epsilon_j = (T/T_{cj} - 1)$ with corresponding critical temperature T_{cj} for each component.

A.3 Numerical Techniques

We numerically solve the TDGL equations based on the finite difference approximation. When we assume that the line-tension of the vortex lines is high, the problem is simplified to a two-dimensional calculation. To maintain gauge invariance after discretization [117], we introduce an auxiliary vector of so-called *link variables*,

$$\begin{aligned} U_x(x,y) &= \exp\left(-i\kappa_1 \int_{x_n}^{x_{n+1}} A_x(\eta, y) d\eta \right), \\ U_y(x,y) &= \exp\left(-i\kappa_1 \int_{y_n}^{y_{n+1}} A_y(x, \zeta) d\zeta \right), \end{aligned} \quad \text{(A.5)}$$

where vector $\mathbf{x_n} = (x_n, y_n)$ is an arbitrary reference point, and U_μ with $\mu = x, y$ is complex valued and unimodular as $U_\mu^* = U_\mu^{-1}$.

Using the link variables, the TDGL equations are rewritten as,

$$\frac{m_1 D_1}{m_j D_j} \frac{\partial \psi_j}{\partial t} - \frac{m_1}{m_j} \frac{1}{\kappa_1^2} \sum_{\mu=x,y} U_\mu^* \frac{\partial^2 (U_\mu \psi_j)}{\partial \mu^2} + \frac{\alpha_1}{|\alpha_j|} \psi_j + \frac{\beta_j}{\beta_1} |\psi_j|^2 \psi_j - \sum_{j<k} \gamma_{jk} \psi_k = 0, \quad \text{(A.6)}$$

$$\sigma \frac{\partial \mathbf{A}}{\partial t} + \nabla \times \nabla \times \mathbf{A} = \mathbf{J}_s, \quad \text{(A.7)}$$

where $\mathbf{J}_s = (J_{s,x}, J_{s,y})$ is given,

$$J_{s,\mu} = \sum_j \frac{m_1}{m_j} \left(\frac{1}{2i\kappa_1} \left[U_\mu^* \psi_j^* \frac{\partial (U_\mu \psi_j)}{\partial \mu} - U_\mu \psi_j \frac{\partial (U_\mu^* \psi_j^*)}{\partial \mu} \right] \right). \quad \text{(A.8)}$$

After the discretization procedure [115] with square meshes of size h as schematically shown in Fig. A.1, the magnetic field in a mesh is calculated as,

$$B_{z;x_n,y_n} = \frac{1 - W_{z;x_n,y_n}}{i\kappa_1 h^2}, \quad \text{(A.9)}$$

with $W_{z;x_n,y_n} = U^*_{x;x_n,y_{n+1}} U^*_{y;x_n,y_n} U_{x;x_n,y_n} U_{y;x_{n+1},y_n}$, and the supercurrents as,

$$J_{s,x;x_n,y_n} = \frac{1}{2i\kappa_1 h} \sum_j \frac{m_1}{m_j} \left(U_{x;x_n,y_n} \psi^*_{j;x_n,y_n} \psi_{j;x_{n+1},y_n} - U^*_{x;x_n,y_n} \psi_{j;x_n,y_n} \psi^*_{j;x_{n+1},y_n} \right), \quad \text{(A.10)}$$

$$J_{s,y;x_n,y_n} = \frac{1}{2i\kappa_1 h} \sum_j \frac{m_1}{m_j} \left(U_{y;x_n,y_n} \psi^*_{j;x_n,y_n} \psi_{j;x_n,y_{n+1}} - U^*_{y;x_n,y_n} \psi_{j;x_n,y_n} \psi^*_{j;x_n,y_{n+1}} \right). \quad \text{(A.11)}$$

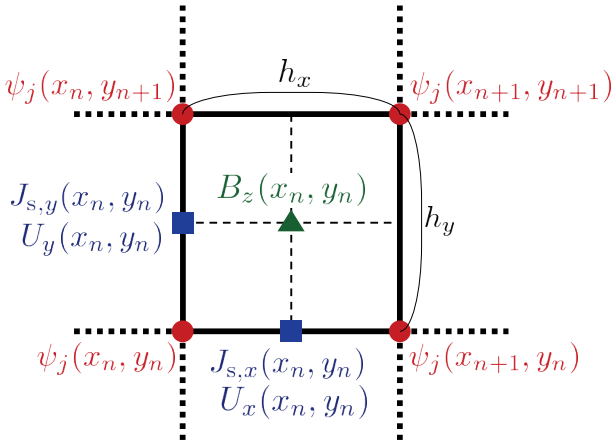

Figure A.1: Numerical discretization scheme representing the evaluation points for ψ_j's (circle), $\mathbf{J}_s$ and $\mathbf{U}$ (square), and B_z (triangle).

Finally, the TDGL equations that are to be solved take the form, for the order parameters,

$$\frac{m_1 D_1}{m_j D_j} \frac{\partial \psi_{j;x_n,y_n}}{\partial t} = \mathscr{F}_{\psi_j;x_n,y_n}, \tag{A.12}$$

where

$$\begin{aligned}\mathscr{F}_{\psi_j;x_n,y_n} = &\left(-\frac{\alpha_1}{|\alpha_j|} - \frac{\beta_j}{\beta_1}|\psi_{j;x_n,y_n}|^2\right)\psi_{j;x_n,y_n} + \sum_{j<k}\gamma_{jk}\psi_{k;x_n,y_n} \\ &+\frac{m_1}{m_j}\frac{1}{\kappa_1^2}\left(\frac{U_{x;x_n,y_n}\psi_{j;x_{n+1},y_n} + U^*_{x;x_{n-1},y_n}\psi_{j;x_{n-1},y_n} - 2\psi_{j;x_n,y_n}}{h^2}\right. \\ &\left.+\frac{U_{y;x_n,y_n}\psi_{j;x_n,y_{n+1}} + U^*_{y;x_n,y_{n-1}}\psi_{j;x_n,y_{n-1}} - 2\psi_{j;x_n,y_n}}{h^2}\right),\end{aligned} \tag{A.13}$$

and for U_x, U_y,

$$\frac{\partial U_{x;x_n,y_n}}{\partial t} = -\frac{i}{\sigma}\mathscr{F}_{U_x;x_n,y_n}, \tag{A.14}$$

$$\frac{\partial U_{y;x_n,y_n}}{\partial t} = -\frac{i}{\sigma}\mathscr{F}_{U_y;x_n,y_n}, \tag{A.15}$$

where

$$\mathscr{F}_{U_x;x_n,y_n} = \mathrm{Im}\left(\frac{W_{z;x_n,y_n} - W_{z;x_n,y_{n-1}}}{h^2} + \sum_j \frac{m_1}{m_j} U_{x;x_n,y_n}\psi^*_{j;x_n,y_n}\psi_{j;x_{n+1},y_n}\right), \tag{A.16}$$

$$\mathscr{F}_{U_y;x_n,y_n} = \mathrm{Im}\left(-\frac{W_{z;x_n,y_n} - W_{z;x_n,y_{n-1}}}{h^2} + \sum_j \frac{m_1}{m_j} U_{y;x_n,y_n}\psi^*_{j;x_n,y_n}\psi_{j;x_n,y_{n+1}}\right). \tag{A.17}$$

Equations (A.12), (A.14), and (A.15) are integrated by a one-step forward-difference technique, with time step Δt,

$$\psi_{j;x_n,y_n}(t+\Delta t) = \psi_{j;x_n,y_n}(t) + \mathscr{F}_{\psi_j;x_n,y_n}\Delta t, \tag{A.18}$$

$$U_{x;x_n,y_n}(t+\Delta t) = U_{x;x_n,y_n}(t)\exp\left(-\frac{i}{\sigma}\mathscr{F}_{U_x;x_n,y_n}\Delta t\right), \tag{A.19}$$

$$U_{y;x_n,y_n}(t+\Delta t) = U_{y;x_n,y_n}(t)\exp\left(-\frac{i}{\sigma}\mathscr{F}_{U_y;x_n,y_n}\Delta t\right). \tag{A.20}$$

A.4 Boundary Conditions

To solve the TDGL equations numerically, we impose the following two types of boundary conditions on a simulation box which yield qualitatively different situations.

Periodic boundary condition

To investigate the interaction between multiple vortices, one introduces a so-called *magnetic periodic boundary condition*, which confines a fixed number of vortices in a simulation box [117, 118, 119, 120],

$$\begin{aligned}
\psi_j(x, L_y) &= \psi_j(x, 0), \\
\psi_j(L_x, y) &= \psi_j(0, y) \exp(iy\Phi/L_y), \\
A_y(L_x, y) &= A_y(0, y) + \Phi/L_y, \\
A_y(x, L_y) &= A_y(x, 0),
\end{aligned} \tag{A.21}$$

where Φ specifies the total reduced flux as $N = \Phi/2\pi$ in the simulation box with the size L_x and L_y in the x and y directions.

This boundary condition is convenient for investigating inherent vortex interactions *as bulk* as discussed in Chapters 3 and 4, because the simulated vortex states are not affected by undesired boundary effects, as we shall discuss next.

Finite boundary condition

As studied by de Gennes using a microscopic theory [121], a general boundary condition at a surface of a finite system takes the form

$$\left(\frac{\hbar}{i}\nabla - \frac{2e}{c}\mathbf{A}\right)\psi_j\bigg|_n = \frac{i\hbar}{b}\psi_j, \tag{A.22}$$

where b is an extrapolation length from the surface to the point at which ψ_j would go to zero outside of a superconductor. The value of b will depend on the nature of the material in contact with the superconductor. The condition for limit $b \to \infty$ means that there is no current passing through the surface, namely the *superconductor-insulator* (SC-I) boundary condition. In contrast, the condition for limit $b \to 0$ corresponds to a boundary in contact with a ferromagnetic material, hence the name *superconductor-ferromagnet* (SC-FM) boundary condition. The other boundary condition for the superconductor and normal-metal depends on the appropriate intermediate value of b. In this thesis, both the SC-I and SC-FM boundary conditions are used and results compared in simulations of the magnetization process and vortex states in a finite system as discussed in Chap. 5.

A finite boundary condition is more convenient when studying vortex states or magnetization (M-H) curves affected by the sample geometry.[1] Figure A.2 shows typical M-H curves for type-I and type-II superconductors based on the introduced multicomponent TDGL method.[2] Using a large simulation box ($150\lambda_{10} \times 130\lambda_{10}$) containing hundreds of vortices, we can approach ideal M-H curves, which are different from the mesoscopic systems where only a couple of vortices are confined within the simulation box.

For the SC-FM boundary condition in Fig. A.2(a), both M-H curves of type-I and type-II superconductivity start to drop almost at the same applied field, which are qualitatively different from experiments. This is an undesired consequence of using the SC-FM boundary condition where vortices always start to penetrate at $H_{c1} \approx H_{tc}$ independent of the GL parameter κ [78].

[1] For instance, vortices near the surface will experience a *repulsive* force due to the external field, but an *attractive* force due to an "image" vortex [122].

[2] Mass ratio $r_m = 1$ is used, which yields essentially the same magnetic properties as conventional superconductors (see Chapter 3)

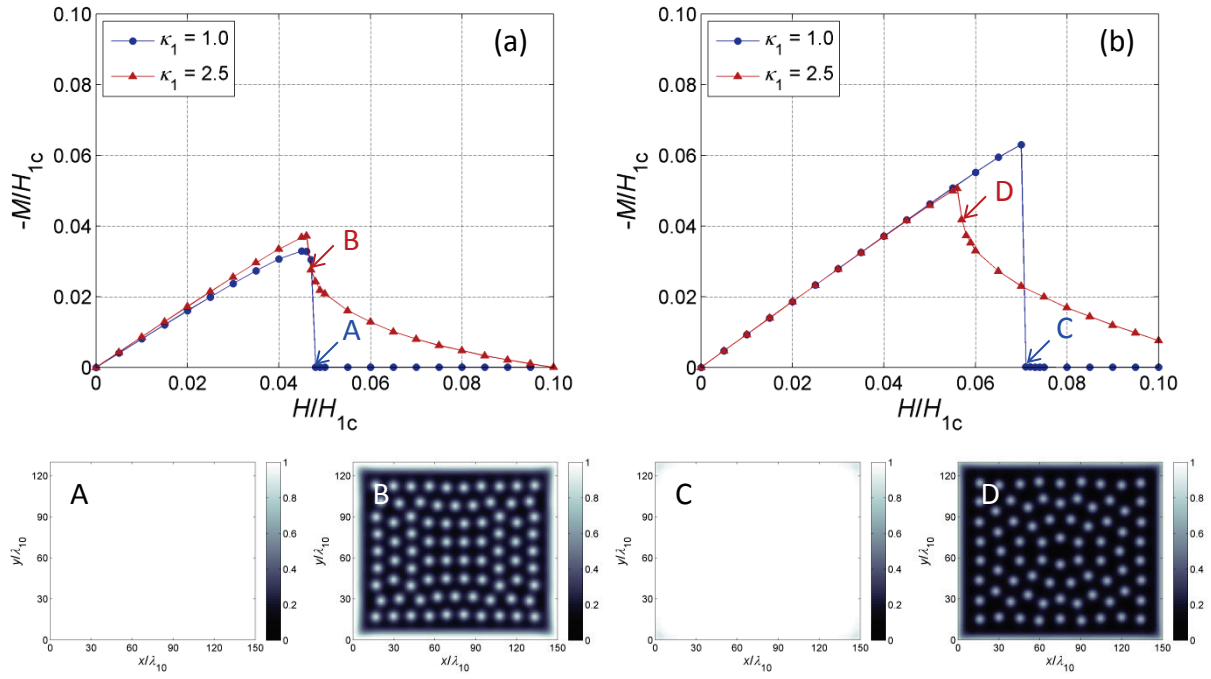

Figure A.2: Typical magnetization (M-H) curves based on the multicomponent TDGL method subject to (a) the superconductor-ferromagnet (SC-FM) and (b) the superconductor-insulator (SC-I) boundary conditions. Material parameters are given as $\kappa_1 = 1.0$ and $\kappa_1 = 2.5$ representing type-I and type-II superconductors, respectively, with $r_m = 1$ common to both. Other parameter values are the same as introduced in Chap. 2. The size of the simulation box is $150\lambda_{10} \times 130\lambda_{10}$ with square meshes of $1\lambda_{10} \times 1\lambda_{10}$. Panels A, B, C, and D represent magnetic flux density B_z (normalized by each applied field H/H_{1c}) of the simulation box at indicated points in the M-H curves.

Appendix B

Magnetic properties in TRSR superconductors

B.1 Multicomponent GL Equations for TRSR Superconductivity

We here discuss a multicomponent superconductor with intercomponent couplings *unfrustrated*, i.e. $\gamma_{12}\gamma_{23}\gamma_{13} > 0$, and analytically derive that it is similar to a single-component case close to T_c.

Around the critical temperature, the order parameters are given by the linearized version of Eq. (1.93),

$$\begin{bmatrix} \alpha_1 & -\gamma_{12} & -\gamma_{13} \\ -\gamma_{12} & \alpha_2 & -\gamma_{23} \\ -\gamma_{13} & -\gamma_{23} & \alpha_3 \end{bmatrix} \begin{bmatrix} \psi_1 \\ \psi_2 \\ \psi_3 \end{bmatrix} = \mathbf{X} \cdot \mathbf{\Psi} = \mathbf{0}. \tag{B.1}$$

The critical temperature T_c is given when the determinant of $\mathbf{X}$ becomes zero. To satisfy the condition that $\mathbf{X}$ is positive definite at $T > T_c$, all determinants of principal minors take non-negative values according to the Sylvester's criterion, namely $\alpha_j \geq 0$ and $\alpha_j\alpha_k - \gamma_{jk}^2 \geq 0$. For the case where $\mathbf{X}$ has a single zero eigenvalue at $T = T_c$ (in contrast to the case of two zero eigenvalues for the TRSB state discussed in Sec. 1.4.3 and Ref. [64]), one has $\sum_{j\neq k}\epsilon_j\epsilon_k = \sum_{j\neq k}(\alpha_j\alpha_k - \gamma_{jk}^2) > 0$ with ϵ_j the eigenvalues of $\mathbf{X}$, which indicates that at least one term in the second summation should be positive (equivalently a single zero eigenvalue), for example $\alpha_2\alpha_3 - \gamma_{23}^2 > 0$.

When $\mathbf{X}$ has two independent vectors at $T = T_c$, the ratios among order parameters for $T \leq T_c$ are given by the Cramer's rules from Eq. (B.1),

$$\begin{aligned} \frac{\psi_2}{\psi_1} &= \frac{\alpha_1\alpha_3 - \gamma_{13}^2}{\gamma_{12}\alpha_3 + \gamma_{13}\gamma_{23}} = \frac{\gamma_{12}\alpha_3 + \gamma_{13}\gamma_{23}}{\alpha_2\alpha_3 - \gamma_{23}^2}, \\ \frac{\psi_3}{\psi_1} &= \frac{\alpha_1\alpha_2 - \gamma_{12}^2}{\gamma_{13}\alpha_2 + \gamma_{12}\gamma_{23}} = \frac{\gamma_{13}\alpha_2 + \gamma_{12}\gamma_{23}}{\alpha_2\alpha_3 - \gamma_{23}^2}, \end{aligned} \tag{B.2}$$

where $\alpha_j\gamma_{kl} + \gamma_{jk}\gamma_{jl} \neq 0$ since $\alpha_j \geq 0$ and $\gamma_{jk}\gamma_{kl}\gamma_{jl} > 0$. It is noticed that the above relations indicate $\alpha_1\alpha_2 - \gamma_{12}^2 > 0$ and $\alpha_1\alpha_3 - \gamma_{13}^2 > 0$. One then arrives at

$$\begin{aligned} \frac{\psi_2^2}{\psi_1^2} &= \frac{\alpha_1\alpha_3 - \gamma_{13}^2}{\alpha_2\alpha_3 - \gamma_{23}^2}, \\ \frac{\psi_3^2}{\psi_1^2} &= \frac{\alpha_1\alpha_2 - \gamma_{12}^2}{\alpha_2\alpha_3 - \gamma_{23}^2}. \end{aligned} \tag{B.3}$$

For $T \leq T_c$, the OPs follow the coupled GL equations,

$$\begin{bmatrix} \alpha_1 + \beta_1\psi_1^2 & -\gamma_{12} & -\gamma_{13} \\ -\gamma_{12} & \alpha_2 + \beta_2\psi_2^2 & -\gamma_{23} \\ -\gamma_{13} & -\gamma_{23} & \alpha_3 + \beta_3\psi_3^2 \end{bmatrix} \begin{bmatrix} \psi_1 \\ \psi_2 \\ \psi_3 \end{bmatrix} = \mathbf{X}' \cdot \mathbf{\Psi} = \mathbf{0}.$$

Since the determinant of $\mathbf{X}'$ should be zero, one has the following OPs taking into account Eq. (B.3),

$$\begin{aligned}\psi_1^2 &\approx \frac{-K_{23}\det\mathbf{X}}{\beta_1K_{23}^2+\beta_2K_{13}^2+\beta_3K_{12}^2},\\ \psi_2^2 &\approx \frac{-K_{13}\det\mathbf{X}}{\beta_1K_{23}^2+\beta_2K_{13}^2+\beta_3K_{12}^2},\\ \psi_3^2 &\approx \frac{-K_{12}\det\mathbf{X}}{\beta_1K_{23}^2+\beta_2K_{13}^2+\beta_3K_{12}^2},\end{aligned} \tag{B.4}$$

where $K_{jk}=\alpha_j\alpha_k-\gamma_{jk}^2$ up to $O(1-T/T_\mathrm{c})$.

B.2 Properties in TRSR Superconductors

Other quantities for a TRSR superconductor are straightforwardly available with the conventional approach [6].

Penetration length

The London penetration depth λ is obtained from the GL equation for supercurrents in Eq. (1.94) multiplying ∇,

$$\nabla\times\nabla\times\mathbf{B}=-\frac{4\pi(2e)^2}{c^2}\sum_j\frac{|\psi_j|^2}{m_j}\mathbf{B}, \tag{B.5}$$

with $\nabla\times\mathbf{A}=\mathbf{B}$ and $\nabla\phi_j=0$. This can be transformed by a vector identity to the London's equation coupled with the Maxwell equation, namely $\nabla^2\mathbf{B}=\mathbf{B}/\lambda$. One then finds,

$$\begin{aligned}\lambda^{-2}&=\frac{4\pi(2e)^2}{c^2}\left(\frac{|\psi_1|^2}{m_1}+\frac{|\psi_2|^2}{m_2}+\frac{|\psi_3|^2}{m_3}\right)\\ &\approx\frac{4\pi(2e)^2}{c^2}\left(\frac{K_{23}}{m_1}+\frac{K_{13}}{m_2}+\frac{K_{12}}{m_3}\right)\frac{-\det\mathbf{X}}{\beta_1K_{23}^2+\beta_2K_{13}^2+\beta_3K_{12}^2}.\end{aligned} \tag{B.6}$$

Coherence length

In order to calculate the coherence length, we consider a one-dimensional system with the boundary condition that the order parameters recover from normal to bulk values, $|\psi_j|\to|\psi_{j0}|$ as $x\to+\infty$,

$$\begin{aligned}\frac{\hbar^2}{2m_1}\frac{\partial^2(\psi_1-\psi_{10})}{\partial x^2}=&\alpha_1(\psi_1-\psi_{10})+3\beta_1\psi_{10}^2(\psi_1-\psi_{10})\\ &-\gamma_{12}(\psi_2-\psi_{20})-\gamma_{13}(\psi_3-\psi_{30}),\\ \frac{\hbar^2}{2m_2}\frac{\partial^2(\psi_2-\psi_{20})}{\partial x^2}=&\alpha_2(\psi_2-\psi_{20})+3\beta_2\psi_{20}^2(\psi_2-\psi_{20})\\ &-\gamma_{12}(\psi_1-\psi_{10})-\gamma_{23}(\psi_3-\psi_{30}),\\ \frac{\hbar^2}{2m_3}\frac{\partial^2(\psi_3-\psi_{30})}{\partial x^2}=&\alpha_3(\psi_3-\psi_{30})+3\beta_3\psi_{30}^2(\psi_3-\psi_{30})\\ &-\gamma_{23}(\psi_2-\psi_{20})-\gamma_{13}(\psi_1-\psi_{10}).\end{aligned} \tag{B.7}$$

Taking $\psi_j-\psi_{j0}=a_j\exp(-\sqrt{2}x/\xi)$ with a single length scale ξ, the equations are rewritten,

$$\begin{bmatrix}\alpha_1+3\beta_1\psi_{10}^2-\hbar^2\xi^{-2}/m_1 & -\gamma_{12} & -\gamma_{13}\\ -\gamma_{12} & \alpha_2+3\beta_2\psi_{20}^2-\hbar^2\xi^{-2}/m_2 & -\gamma_{23}\\ -\gamma_{13} & -\gamma_{23} & \alpha_3+3\beta_3\psi_{30}^2-\hbar^2\xi^{-2}/m_3\end{bmatrix}\begin{bmatrix}a_1\\a_2\\a_3\end{bmatrix}=\mathbf{Y}\cdot\mathbf{a}=0. \tag{B.8}$$

The coherence length ξ is then obtained from $\det \mathbf{Y} = 0$,

$$\xi^{-2} \approx \frac{2}{\hbar^2} \frac{-\det \mathbf{X}}{K_{23}/m_1 + K_{13}/m_2 + K_{12}/m_3}. \tag{B.9}$$

Thermodynamic field

The thermodynamic magnetic field $H_{\rm tc}$ is equated with free energy difference between superconductivity and normal state in absence of magnetic fields in Eq. (1.91), namely $f_{\rm n} - f_{\rm sc} = \sum_{j=1,2,3} \alpha_j |\psi_j|^2 + \beta_j |\psi_j|^4$. One can readily derive with the OPs in Eq. (B.4),

$$\frac{H_{\rm tc}^2}{8\pi} \approx \frac{1}{2} \frac{(\det \mathbf{X})^2}{\beta_1 K_{23}^2 + \beta_2 K_{13}^2 + \beta_3 K_{12}^2}. \tag{B.10}$$

Nucleation field

Finally, the nucleation field $H_{\rm n}$ is derived from the linearized GL equations in the presence of fields H. Taking the gauge $A_y = Hx, A_x = 0, A_z = 0$, the OPs can be expressed $\psi_j = e^{ik_y y} e^{ik_z z} f(x)$, which yield similar forms to the Schrödinger equation,

$$-\frac{\hbar}{2m_j} f_j'' + \frac{\hbar}{2m_j} \left(\frac{2\pi H}{\Phi_0} \right)^2 (x - x_0)^2 f_j = -\left(\alpha_j + \frac{\hbar^2 k_z^2}{2m_j} \right) f_j + \gamma_{jk} f_k + \gamma_{jl} f_l, \tag{B.11}$$

where $x_0 = k_y \Phi_0 / 2\pi H$. Based on the lowest Landau level solution with $f_j = b_j \exp\left[-\frac{1}{2} \frac{2\pi H}{\Phi_0} (x - x_0)^2 \right]$, we obtain

$$\begin{bmatrix} \alpha_1 + \frac{\hbar^2}{2m_1} \left(k_z^2 + \frac{2\pi H}{\Phi_0} \right) & -\gamma_{12} & -\gamma_{13} \\ -\gamma_{12} & \alpha_2 + \frac{\hbar^2}{2m_2} \left(k_z^2 + \frac{2\pi H}{\Phi_0} \right) & -\gamma_{23} \\ -\gamma_{13} & -\gamma_{23} & \alpha_3 + \frac{\hbar^2}{2m_3} \left(k_z^2 + \frac{2\pi H}{\Phi_0} \right) \end{bmatrix} \begin{bmatrix} b_1 \\ b_2 \\ b_3 \end{bmatrix} = \mathbf{Z} \cdot \mathbf{b} = 0. \tag{B.12}$$

The nucleation field is derived with $\det \mathbf{Z} = 0$ and $k_z = 0$,

$$H_{\rm n} \approx \frac{\Phi_0}{2\pi} \frac{2}{\hbar^2} \frac{-\det \mathbf{X}}{K_{23}/m_1 + K_{13}/m_2 + K_{12}/m_3}. \tag{B.13}$$

B.3 Summary

Based on the coherence length ξ and the penetration depth λ obtained here, the characteristic fields can be rewritten as $H_{\rm tc} = \Phi_0 / 2\sqrt{2}\pi\xi\lambda$ and $H_{\rm n} = \Phi_0 / 2\pi\xi^2$. We obviously find that $H_{\rm n}/H_{\rm tc} = \sqrt{2}\lambda/\xi = \sqrt{2}\kappa$, with the GL parameter κ. Therefore, magnetic properties in a TRSR superconductor are essentially the same as a conventional single-component case.

Bibliography

[1] H. Kamerlingh Onnnes, The Superconductivity of Mercury, *Leiden Comm.* **120b, 122b, 124c** (1911).

[2] W. Meissner and R. Ochsenfeld, Ein neuer Effekt bei Eintritt der Supraleitf ahigkeit *Naturwissenschafter* **21**, 787 (1933).

[3] A. A. Abrikosov, On the Magnetic Properties of Superconductors of the Second Group, *Zh. Eksp. Teor. Fiz.* **32**, 1442 (1957).

[4] J. E. Kunzler, E. Buehler, F. S. L. Hsu, J. H. Wernick, Superconductivity in Nb_3Sn at High Current Density in a Magnetic Field of 88 kgauss, *Phys. Rev. Lett.* **6**, 89 (1961).

[5] J. Bardeen, L. N. Cooper and J. R. Schrieffer, Theory of Superconductivity, *Phys. Rev.* **108**, 1175 (1957).

[6] M. Tinkham, *Introduction to Superconductivity*, 2nd ed., (Dover, New York, 2004).

[7] L. P. Gor'kov, Microscopic derivation of the Ginzburg-Landau equations in the theory of superconductivity, *Sov. Phys. JETP* **36**, 1364 (1959).

[8] A. J. Leggett, A theoretical description of the new phases of liquid ^{3}He, *Rev. Mod. Phys.* **47**, 331 (1975).

[9] F. Steglich, J. Aarts, C. D. Bredl, W. Lieke, D. Meschede, W. Franz and H. Schäfer, Superconductivity in the Presence of Strong Pauli Paramagnetism: $CeCu_2Si_2$, *Phys. Rev. Lett.* **43**, 1892 (1979).

[10] M. Sigrist and K. Ueda, Phenomenological theory of unconventional superconductivity, *Rev. Mod. Phys.* **63**, 239 (1991).

[11] J. G. Bednorz and K. A. Müller, Possible high T_c superconductivity in the Ba-La-Cu-O system, *Z. Phys. B Condens. Matter.* **64**, 189 (1986).

[12] J. Nagamatsu, N. Nakagawa, T. Muranaka, Y. Zenitani, and J. Akimitsu, Superconductivity at 39K in magnesium diboride, *Nature* **410**, 63 (2001).

[13] Y. Kamihara, T. Watanabe, M. Hirano and H. Hosono, Iron-Based Layered Superconductor $La[O_{1-x}F_x]FeAs$ ($x = 0.05 - 0.12$) with $T_c = 26$K, *J. Am. Chem. Soc.* **130**, 3296 (2008).

[14] M. K. Wu, J. R. Ashburn, and C. J. Torng, P. H. Hor, R. L. Meng, L. Gao, Z. J. Huang, Y. Q. Wang and C. W. Chu, Superconductivity at 93 K in a new mixed-phase Y-Ba-Cu-O compound system at ambient pressure, *Phys. Rev. Lett.* **58**, 908 (1987).

[15] H. Maeda, Y. Tanaka, M. Fukutomi and T. Asano, A New High-T_c Oxide Superconductor without a Rare Earth Element, *Jpn. J. Appl. Phys.* **27**, L209 (1988).

[16] A. Schilling, M. Cantoni, J. D. Guo, and H. R. Ott, Superconductivity above 130 K in the Hg-Ba-Ca-Cu-O system, *Nature* **363**, 56 (1993).

[17] D. J. Scalapino, A common thread: The pairing interaction for unconventional superconductors, *Rev. Mod. Phys.* **84**, 1383 (2012).

[18] N. Barišić, M. K. Chan, Y. Li, G. Yu, X. Zhao, and M. Dressel, A. Smontara, and M. Greven, Universal sheet resistance and revised phase diagram of the cuprate high-temperature superconductors, *Proc. Natl. Acad. Sci.* **110**, 12235 (2013).

[19] C. Varma, High-temperature superconductivity: Mind the pseudogap, *Nature* **468**, 184 (2010).

[20] S. L. Bud'ko, G. Lapertot, C. Petrovic, C. E. Cunningham, N. Anderson and P. C. Canfield, Boron Isotope Effect in Superconducting MgB_2, *Phys. Rev. Lett.* **86**, 1877 (2001).

[21] C. Buzea and T. Yamashita, Review of the superconducting properties of MgB_2, *Supercond. Sci. Technol.* **14**, R115 (2001).

[22] X. X. Xi, Two-band superconductor magnesium diboride, *Rep. Prog. Phys.* **71**, 116501 (2008).

[23] J. Kortus, and I. I. Mazin, K. D. Belashchenko, V. P. Antropov and L. L. Boyer, Superconductivity of Metallic Boron in MgB_2, *Phys. Rev. Lett.* **86**, 4656 (2001).

[24] M. Iavarone, G. Karapetrov, A. E. Koshelev, W. K. Kwok, G. W. Crabtree, D. G. Hinks, W. N. Kang, E.-M. Choi, H. J. Kim, H.-J. Kim and S. I. Lee, Two-Band Superconductivity in MgB_2, *Phys. Rev. Lett.* **89**, 187002 (2002).

[25] I. I. Mazin, O. K. Andersen, O. Jepsen, O. V. Dolgov, J. Kortus, A. A. Golubov, A. B. Kuz'menko and D. van der Marel, Superconductivity in MgB_2: Clean or Dirty?, *Phys. Rev. Lett.* **89**, 107002 (2002).

[26] H. Suhl, B. T. Matthias and L. R. Walker, Bardeen-Cooper-Schrieffer Theory of Superconductivity in the Case of Overlapping Bands, *Phys. Rev. Lett.* **3**, 552 (1959).

[27] H. Kotegawa, K. Ishida, Y. Kitaoka, T. Muranaka and J. Akimitsu, Evidence for Strong-Coupling s-Wave Superconductivity in MgB_2: ^{11}B NMR Study, *Phys. Rev. Lett.* **87**, 127001 (2001).

[28] F. Manzano, A. Carrington, N. E. Hussey, S. Lee, A. Yamamoto and S. Tajima, Exponential Temperature Dependence of the Penetration Depth in Single Crystal MgB_2, *Phys. Rev. Lett.* **88**, 047002 (2002).

[29] D. J. Van Harlingen, Phase-sensitive tests of the symmetry of the pairing state in the high-temperature superconductors–Evidence for $d_{x^2-y^2}$ symmetry, *Rev. Mod. Phys.* **67**, 515 (1995).

[30] A. P. Mackenzie and Y. Maeno, The superconductivity of Sr_2RuO_4 and the physics of spin-triplet pairing, *Rev. Mod. Phys.* **75**, 657 (2003).

[31] G. Blumberg, A. Mialitsin, B. S. Dennis, M. V. Klein, N. D. Zhigadlo and J. Karpinski, Observation of Leggett's Collective Mode in a Multiband MgB_2 Superconductor, *Phys. Rev. Lett.* **99**, 227002 (2007).

[32] Y. Kamihara, H. Hiramatsu, M. Hirano, R. Kawamura, H. Yanagi, T. Kamiya, and H. Hosono, Iron-Based Layered Superconductor: LaOFeP, *J. Am. Chem. Soc.* **128**, 10012 (2006).

[33] Z.-A. Ren, J. Yang, W. Lu, W. Yi, X.-L. Shen, Z.-C. Li, G.-C. Che, X.-L. Dong, L.-L. Sun, F. Zhou and Z.-X. Zhao, Superconductivity in the iron-based F-doped layered quaternary compound $Nd[O_{1-x}F_x]FeAs$, *Europhys. Lett.* **82**, 57002 (2008).

[34] Z.-A. Ren, W. Lu, J. Yang, W. Yi, X.-L. Shen, Z.-C. Li, G.-C. Che, X.-L. Dong, L.-L. Sun, F. Zhou and Z.-X. Zhao, Superconductivity at 55 K in Iron-Based F-Doped Layered Quaternary Compound $Sm[O_{1-x}F_x]FeAs$, *Chin.Phys.Lett.* **25**, 2215 (2008).

[35] M. Rotter, M. Tegel and D. Johrendt, Superconductivity at 38 K in the Iron Arsenide $(Ba_{1-x}K_x)Fe_2As_2$, *Phys. Rev. Lett.* **101**, 107006 (2008).

[36] K. Sasmal, B. Lv, B. Lorenz, A. M. Guloy, F. Chen, Y.-Y. Xue and C.-W. Chu, Superconducting Fe-Based Compounds $(A_{1-x}Sr_x)Fe_2As_2$ with $A =$ K and Cs with Transition Temperatures up to 37 K, *Phys. Rev. Lett.* **101**, 107007 (2008).

[37] J. H. Tapp, Z. Tang, B. Lv, K. Sasmal, B. Lorenz, P. C. W. Chu and A. M. Guloy, LiFeAs: An intrinsic FeAs-based superconductor with $T_c = 18$K, *Phys. Rev. B* **78**, 060505 (2008).

[38] F.-C. Hsu, J.-Y. Luo, K.-W. Yeh, T.-K. Chen, T.-W. Huang, P. M. Wu, Y.-C. Lee, Y.-L. Huang, Y.-Y. Chu, D.-C. Yan and M.-K. Wu, Superconductivity in the PbO-type structure α-FeSe, *Proc. Natl. Acad. Sci.* **105**, 14262 (2008).

[39] T. M. McQueen, Q. Huang, V. Ksenofontov, C. Felser, Q. Xu, H. Zandbergen, Y. S. Hor, J. Allred, A. J. Williams, D. Qu, J. Checkelsky, N. P. Ong, and R. J. Cava, Extreme sensitivity of superconductivity to stoichiometry in $Fe_{1+\delta}Se$, *Phys. Rev. B* **79**, 014522 (2009).

[40] S. Margadonna, Y. Takabayashi, Y. Ohishi, Y. Mizuguchi, Y. Takano, T. Kagayama, T. Nakagawa, M. Takata, and K. Prassides, Pressure evolution of the low-temperature crystal structure and bonding of the superconductor FeSe ($T_c = 37$K), *Phys. Rev. B* **80**, 064506 (2009).

[41] H. Ogino, Y. Matsumura, Y. Katsura, K. Ushiyama, S. Horii, K. Kishio and J. Shimoyama, Superconductivity at 17 K in $(Fe_2P_2)(Sr_4Sc_2O_6)$: a new superconducting layered pnictide oxide with a thick perovskite oxide layer, *Supercond. Sci. Technol.* **22**, 075008 (2009).

[42] X. Zhu, F. Han, G. Mu, P. Cheng, B. Shen, B. Zeng H.-H. Wen, Transition of stoichiometric Sr_2VO_3FeAs to a superconducting state at 37.2 K, *Phys. Rev. B* **79**, 220512 (2009).

[43] K. Tanabe and H. Hosono, Frontiers of Research on Iron-Based Superconductors toward Their Application, *Jpn. J. Appl. Phys.* **51**, 010005 (2012).

[44] P. J. Hirschfeld, M. M. Korshunov and I. I. Mazin, Gap symmetry and structure of Fe-based superconductors, *Rep. Prog. Phys.* **74**, 124508 (2011).

[45] H. Ding, P. Richard, K. Nakayama, K. Sugawara, T. Arakane, Y. Sekiba, A. Takayama, S. Souma, T. Sato, T. Takahashi, Z. Wang, X. Dai, Z. Fang, G. F. Chen, J. L. Luo and N. L. Wang, Observation of Fermi-surfacedependent nodeless superconducting gaps in $Ba_{0.6}K_{0.4}Fe_2As_2$, *Europhys. Lett.* **83**, 47001 (2008).

[46] D. C. Johnston, The puzzle of high temperature superconductivity in layered iron pnictides and chalcogenides, *Adv. Phys.* **59**, 803 (2010).

[47] C. de la Cruz, Q. Huang, J. W. Lynn, J. Li, W. Ratcliff II, J. L. Zarestky, H. A. Mook, G. F. Chen, J. L. Luo, N. L. Wang and P. Dai, Magnetic order close to superconductivity in the iron-based layered $LaO_{1-x}F_xFeAs$ systems, *Nature* **453**, 899 (2008).

[48] J. Kondo, Superconductivity in Transition Metals, *Prog. Theor. Phys.* **29**, 1 (1963).

[49] A. J. Leggett, Number-Phase Fluctuations in Two-Band Superconductors, *Prog. Theor. Phys.* **36**, 901 (1966).

[50] D. F. Agterberg, V. Barzykin and L. P. Gor'kov; Conventional mechanisms for exotic superconductivity, *Phys. Rev. B* **60**, 14868 (1999).

[51] D. F. Agterberg, V. Barzykin and L. P. Gor'kov, Exotic ground states and impurities in multiband superconductors, *Europhys. Lett.* **48**, 449 (1999).

[52] V. Stanev and Z. Tešanović. Three-band superconductivity and the order parameter that breaks time-reversal symmetry, *Phys. Rev. B* **81**, 134522 (2010).

[53] W.-C. Lee, S.-C. Zhang and C. Wu, Pairing State with a Time-Reversal Symmetry Breaking in FeAs-Based Superconductors, *Phys. Rev. Lett.* **102**, 217002 (2009).

[54] C. Platt, R. Thomale, C. Honerkamp, S.-C. Zhang and W. Hanke, Mechanism for a pairing state with time-reversal symmetry breaking in iron-based superconductors, *Phys. Rev. B* **85**, 180502 (2012).

[55] S. Maiti and A. V. Chubukov, $s + is$ state with broken time-reversal symmetry in Fe-based superconductors, *Phys. Rev. B* **87**, 144511 (2013).

[56] T. K. Ng and N. Nagaosa, Broken time-reversal symmetry in Josephson junction involving two-band superconductors, *Europhys. Lett.* **87**, 17003 (2009).

[57] S.-Z. Lin, Josephson effect between a two-band superconductor with $s++$ or $s\pm$ pairing symmetry and a conventional s-wave superconductor, *Phys. Rev. B* **86**, 014510 (2012).

[58] Y. Tanaka and T. Yanagisawa, Chiral Ground State in Three-Band Superconductors, *J. Phys. Soc. Jpn.* **79**, 114706 (2010).

[59] T. Yanagisawa, Y. Tanaka, I. Hase and K. Yamaji, Vortices and Chirality in Multi-Band Superconductors, *J. Phys. Soc. Jpn.* **81**, 024712 (2012).

[60] Y. Ota, M. Machida, T. Koyama and H. Aoki, Collective modes in multiband superfluids and superconductors: Multiple dynamical classes, *Phys. Rev. B* **83**, 060507 (2011).

[61] J. Carlström, J. Garaud and E. Babaev, Length scales, collective modes, and type-1.5 regimes in three-band superconductors, *Phys. Rev. B* **84**, 134518 (2011).

[62] V. Stanev, Model of collective modes in three-band superconductors with repulsive interband interactions, *Phys. Rev. B* **85**, 174520 (2012).

[63] S.-Z. Lin and X. Hu, Massless Leggett Mode in Three-Band Superconductors with Time-Reversal-Symmetry Breaking, *Phys. Rev. Lett.* **108**, 177005 (2012).

[64] X. Hu and Z. Wang, Stability and Josephson effect of time-reversal-symmetry-broken multicomponent superconductivity induced by frustrated intercomponent coupling, *Phys. Rev. B* **85**, 064516 (2012).

[65] M. E. Zhitomirsky and V.-H. Dao, Ginzburg-Landau theory of vortices in a multigap superconductor, *Phys. Rev. B* **69**, 054508 (2004).

[66] A. Gurevich, Limits of the upper critical field in dirty two-gap superconductors, *Physica C* **456**, 160 (2007).

[67] G. Arfken, *Mathematical Methods for Physics*, 3rd ed., (Academic Press, San Diego, 1985).

[68] N. V. Orlova, A. A. Shanenko, M. V. Milošević, F. M. Peeters, A. V. Vagov and V. M. Axt, Ginzburg-Landau theory for multiband superconductors: Microscopic derivation, *Phys. Rev. B* **87**, 134510 (2013).

[69] J. Garaud, J. Carlström and E. Babaev, Topological Solitons in Three-Band Superconductors with Broken Time Reversal Symmetry, *Phys. Rev. Lett.* **107**, 197001 (2011).

[70] S.-Z. Lin and X. Hu, Phase solitons in multi-band superconductors with and without time-reversal symmetry, *New J. Phys.* **14**, 063021 (2012).

[71] E. Babaev, J. Carlström, J. Garaud, M. Silaev and J. M. Speight, Type-1.5 superconductivity in multiband systems: Magnetic response, broken symmetries and microscopic theory - A brief overview, *Physica C* **479**, 2 (2012).

[72] J. Garaud, J. Carlström, E. Babaev and J. M. Speight, Chiral $\mathbb{C}P^2$ skyrmions in three-band superconductors, *Phys. Rev. B* **87**, 014507 (2013).

[73] Y. Takahashi and Z. Huang and X. Hu, Unconventional vortex state in multicomponent superconductors with time-reversal symmetry breaking, *Physica C* **493**, 82 (2013).

[74] S. Gillis, J. Jäykkä and M. V. Milošević, Vortex states in mesoscopic three-band superconductors, arXiv:1308.4981 (2013).

[75] L. Jacobs and C. Rebbi, Interaction energy of superconducting vortices, *Phys. Rev. B* **19**, 4486 (1979).

[76] I. Luk'yanchuk, Theory of superconductors with κ close to $1/\sqrt{2}$, *Phys. Rev. B* **63**, 174504 (2001).

[77] J. Geyer, R. M. Fernandes, V. G. Kogan and J. Schmalian, Interface energy of two-band superconductors, *Phys. Rev. B* **82**, 104521 (2010).

[78] A. D. Hernández and D. Domínguez, Surface barrier in mesoscopic type-I and type-II superconductors, *Phys. Rev. B* **65**, 144529 (2002).

[79] M. A. Silaev, Stable fractional flux vortices and unconventional magnetic state in two-component superconductors, *Phys. Rev. B* **83**, 144519 (2011).

[80] E. H. Brandt and M. P. Das, Attractive Vortex Interaction and the Intermediate-Mixed State of Superconductors, *J. Supercond. Nov. Magn* **24**, 57 (2011).

[81] E. Zeldov, D. Majer, M. Konczykowski, V. B. Geshkenbein, V. M. Vinokur and H. Shtrikman, Thermodynamic observation of first-order vortex-lattice melting transition in $Bi_2Sr_2CaCu_2O_8$, *Nature* **375**, 373 (1995).

[82] X. Hu, S. Miyashita and M. Tachiki, δ-Function Peak in the Specific Heat of High- T_c Superconductors: Monte Carlo Simulation, *Phys. Rev. Lett.* **79**, 3498 (1997).

[83] X. Hu, S. Miyashita and M. Tachiki, Monte Carlo simulation on the first-order melting transition of high-T_c superconductors in $\mathbf{B} \parallel \mathbf{c}$, *Phys. Rev. B* **58**, 3438 (1998).

[84] M. B. Gaifullin, Y. Matsuda, N. Chikumoto, J. Shimoyama and K. Kishio, Abrupt Change of Josephson Plasma Frequency at the Phase Boundary of the Bragg Glass in $Bi_2Sr_2CaCu_2O_{8+\delta}$, *Phys. Rev. Lett.* **84**, 2945 (2000).

[85] T. Nishizaki and N. Kobayashi, Vortex Physics and Flux Pinning, *Studies of High Temperature Superconductors*, Vol. 48, (NOVA, New York, 2004).

[86] T. Nishizaki and N. Kobayashi, Vortex-matter phase diagram in $YBa_2Cu_3O_y$, *Supercond. Sci. Technol.* **13**, 1 (2000).

[87] R. Kleiner, F. Steinmeyer, G. Kunkel and P. Müller, Intrinsic Josephson effects in $Bi_2Sr_2CaCu_2O_8$ single crystals, *Phys. Rev. Lett.* **68**, 2394 (1992).

[88] M. Tachiki and S. Takahashi, Anisotropy of critical current in layered oxide superconductors, *Solid State Commun.* **72**, 1083 (1989).

[89] X. Hu and M. Tachiki, Structure and Phase Transition of Josephson Vortices in Anisotropic High- T_c Superconductors, *Phys. Rev. Lett.* **80**, 4044 (1998).

[90] X. Hu and M. Tachiki, Possible Tricritical Point in Phase Diagrams of Interlayer Josephson-Vortex Systems in High- T_c Superconductors, *Phys. Rev. Lett.* **85**, 2577 (2000).

[91] L. Balents and D. R. Nelson, Quantum smectic and supersolid order in helium films and vortex arrays, *Phys. Rev. B* **52**, 12951 (1995).

[92] X. Hu, M. Luo and Y. Ma, Density functional theory for the freezing transition of the vortex-line liquid with periodic layer pinning, *Phys. Rev. B* **72**, 174503 (2005).

[93] X. Hu and M. Tachiki, Decoupled two-dimensional superconductivity and continuous melting transitions in layered superconductors immersed in a parallel magnetic field, *Phys. Rev. B* **70**, 064506 (2004).

[94] S. N. Gordeev, A. A. Zhukov, P. A. J. de Groot, A. G. M. Jansen, R. Gagnon and L. Taillefer, Oscillatory Melting Temperature of the Vortex Smectic Phase in Layered Superconductors, *Phys. Rev. Lett.* **85**, 4594 (2000).

[95] T. Naito, H. Iwasaki, T. Nishizaki, S. Haraguchi, Y. Kawabata, K. Shibata and N. Kobayashi, Vortex slush regime in the Josephson vortex phase diagram of 60-K $YBa_2Cu_3O_{7-\delta}$ single crystals, *Phys. Rev. B* **68**, 224516 (2003).

[96] B. Lundqvist, Ö. Rapp and M. Andersson, Experimental evidence for a three-dimensional – two-dimensional crossover for magnetic fields parallel to the ab plane in oxygen-deficient single crystals of $YBa_2Cu_3O_{7-\delta}$, *Phys. Rev. B* **62**, 3542 (2000).

[97] B. Lundqvist, Ö. Rapp, M. Andersson and Y. Eltsev, Nearly field-independent in-plane vortex solid-to-liquid transition in the c-axis resistivity of oxygen deficient single crystals of $YBa_2Cu_3O_{7-\delta}$, *Phys. Rev. B* **64**, 060503 (2001).

[98] N. E. Hussey, H. Takagi, N. Takeshita, N. Mori, Y. Iye, S. Adachi and K. Tanabe, Melting of the vortex lattice in $YBa_2Cu_4O_8$ in parallel fields, *Phys. Rev. B* **59**, R11668 (1999).

[99] T. Nishizaki, Y. Takahashi and N. Kobayashi, Phase diagram of interlayer Josephson vortices in underdoped $YBa_2Cu_3O_y$, *Physica C* **468**, 664 (2008).

[100] Y. Nonomura and X. Hu, Energy landscape and shear modulus of interlayer Josephson vortex systems, *Phys. Rev. B* **74**, 024504 (2006).

[101] A. E. Koshelev, Ground states of the Josephson vortex lattice in layered superconductors, arXiv:cond-mat/0602341 (2006).

[102] C. Kittel, *Introduction to Solid State Physics*, 7th ed., (John Wiley & Sons, New York, 1996).

[103] T. R. Chien, W. R. Datars, B. W. Veal, A. P. Paulikas, P. Kostic, C. Gu and Y. Jiang, Dimensional crossover and oxygen deficiency in $YBa_2Cu_3O_{7-y}$ single crystals, *Physica C* **229**, 273 (1994).

[104] K. Takenaka, K. Mizuhashi, H. Takagi and S. Uchida, Interplane charge transport in $YBa_2Cu_3O_{7-y}$: Spin-gap effect on in-plane and out-of-plane resistivity, *Phys. Rev. B* **50**, 6534 (1994).

[105] K. Semba and A. Matsuda, Superconductor-to-Insulator Transition and Transport Properties of Underdoped $YBa_2Cu_3O_y$ Crystals, *Phys. Rev. Lett.* **86**, 496 (2001).

[106] P. J. W. Moll, L. Balicas, V. Geshkenbein, G. Blatter, J. Karpinski, N. D. Zhigadlo and B. Batlogg, Transition from slow Abrikosov to fast moving Josephson vortices in iron pnictide superconductors, *Nat. Mater.* **12**, 134 (2013).

[107] F. Liu, M. Mondello and N. Goldenfeld, Kinetics of the superconducting transition, *Phys. Rev. Lett.* **66**, 3071 (1991).

[108] H. Frahm, S. Ullah and A. T. Dorsey, Flux dynamics and the growth of the superconducting phase, *Phys. Rev. Lett.* **66**, 3067 (1991).

[109] R. Kato, Y. Enomoto and S. Maekawa, Computer simulations of dynamics of flux lines in type-II superconductors, *Phys. Rev. B* **44**, 6916 (1991).

[110] M. Machida and H. Kaburaki, Direct simulation of the time-dependent Ginzburg-Landau equation for type-II superconducting thin film: Vortex dynamics and $V - I$ characteristics, *Phys. Rev. Lett.* **71**, 3206 (1993).

[111] R. Kato, Y. Enomoto and S. Maekawa, Effects of the surface boundary on the magnetization process in type-II superconductors, *Phys. Rev. B* **47**, 8016 (1993).

[112] S. Kim, J. Burkardt, M. Gunzburger, J. Peterson and C.-R. Hu, Effects of sample geometry on the dynamics and configurations of vortices in mesoscopic superconductors, *Phys. Rev. B* **76**, 024509 (2007).

[113] M. V. Milošević, G. R. Berdiyorov and F. M. Peeters, Fluxonic cellular automata, *Appl. Phys. Lett.* **91**, 212501 (2007).

[114] X. H. Chao, B. Y. Zhu, A. V. Silhanek and V. V. Moshchalkov, Current-induced giant vortex and asymmetric vortex confinement in microstructured superconductors, *Phys. Rev. B* **80**, 054506 (2009).

[115] W. D. Gropp, H. G. Kaper, G. K. Leaf, D. M. Levine, M. Palumbo and V. M. Vinokur, Numerical Simulation of Vortex Dynamics in Type-II Superconductors, *J. Comput. Phys.* **123**, 254 (1996).

[116] S.-Z. Lin and X. Hu, Vortex states and the phase diagram of a multiple-component Ginzburg-Landau theory with competing repulsive and attractive vortex interactions, *Phys. Rev. B* **84**, 214505 (2011).

[117] H. G. Kaper and M. K. Kwong, Vortex configurations in type-II superconducting films, *J. Comput. Phys.* **119**, 120 (1995).

[118] M. M. Doria, J. E. Gubernatis and D. Rainer, Virial theorem for Ginzburg-Landau theories with potential applications to numerical studies of type-II superconductors, *Phys. Rev. B* **39**, 9573 (1989).

[119] M. M. Doria, J. E. Gubernatis and D. Rainer, Solving the Ginzburg-Landau equations by simulated annealing, *Phys. Rev. B* **41**, 6335 (1990).

[120] Z. D. Wang and C.-R. Hu, Numerical relaxation approach for solving the general Ginzburg-Landau equations for type-II superconductors, *Phys. Rev. B* **44**, 11918 (1991).

[121] P. G. de Gennes, *Superconductivity of Metals and Alloys*, (Benjamin, New York, 1966).

[122] C. P. Bean and J. D. Livingston, Surface Barrier in Type-II Superconductor, *Phys. Rev. Lett.* **12**, 14 (1964).